Dynamics of Granular Matter in Two Dimensions

Inaugural-Dissertation

zur Erlangung des Doktorgrades
der Mathematisch-Naturwissenschaftlichen Fakultät
der Heinrich-Heine-Universität Düsseldorf

vorgelegt von

Elmar Stärk
aus Lahnstein

Düsseldorf, Oktober 2012

aus dem Institut für Theoretische Physik II: Weiche Materie
der Heinrich-Heine-Universität Düsseldorf

Gedruckt mit der Genehmigung der
Mathematisch-Naturwissenschaftlichen Fakultät der
Heinrich-Heine-Universität Düsseldorf

Referent: Professor Doktor Jürgen Horbach
Korreferent: Professor Doktor Stefan Egelhaaf

Tag der mündlichen Prüfung:

Abstract

In this thesis, the dynamics of granular matter are investigated in different experiments. Image processing algorithms are developed and used to extract particle positions from the experimental data.

A 2D Lorentz model is realized by driving a particle through a network of obstacles on a vibrating table. The mechanism of driving a particle horizontally by vertical vibrations is analyzed in detail. The mean-squared displacement is measured over more then six decades in time. Critical exponents for the long-time dynamics of particles of different sizes are found and compared to simulation results.

The behavior of 2D granular fluids close to the glass transition is investigated: Bidisperse mixtures of disk-like particles are driven by a vibrating table. The particles are marked by individual labels, which can be identified by an image processing algorithm. This algorithm allows to measure the evolution of the mean-squared displacement over long times, while the influence of particle tracking errors is greatly reduced. The emergence of a plateau in the mean-squared displacement close to the glass transition is observed. α-scaling is successfully applied and compared to mode-coupling predictions.

In 3D, the data from microgravity experiments on magnetically excited granular gases is analyzed. Particle velocity distributions both during magnetical driving and during granular cooling are determined. The cooling behavior is evaluated for different densities and Haff's Law is verified.

Zusammenfassung

In dieser Doktorarbeit wird die Dynamik granularer Materialien in verschiedenen Experimenten untersucht. Bildverarbeitungsalgorithmen zur Bestimmung von Teilchenpositionen werden entwickelt und angewendet.

Ein 2D Lorentzmodell wird mit Hilfe durch vertikale Schwingungen getriebener Testteilchen realisiert, die sich durch ein Netzwerk von Hindernissen bewegen. Die Umsetzung der vertikalen Schwingungen in horizontale Teilchenbewegungen wird detailiert untersucht. Das mittlere Verschiebungsquadrat wird über mehr als sechs zeitliche Dekaden gemessen. Kritische Exponenenten für die Langzeitdynamik von Teilchen verschiedener Größe werden ermittelt und mit Simulationsergebnissen verglichen.

Das Verhalten eines zweidimensionalen granularen Fluids wird untersucht: Bidisperse Mischungen scheibenähnlicher Teilchen werden durch einen Rütteltisch angetrieben. Die einzelnen Teilchen werden mit individuellen Codes markiert, die dann durch einen Bildverarbeitungsalgorithmus ausgelesen werden. Dieser Algorithmus erlaubt, Langzeitmessungen durchzuführen und dabei Störungen durch Teilchenverfolgungsfehler weitestgehend zu vermeiden. Die Ausbildung eines Plateaus im mittleren Verschiebungsquadrat über mehr als vier zeitliche Dekaden kann nahe dem Glasübergang beobachtet werden. α-Scaling wird erfolgreich angewandt und mit Modenkopplungsvorhersagen verglichen.

Die Daten eines Mikrogravitationsexperimentes bezüglich magnetisch getriebener granularer Gase werden ausgewertet. Die Verteilungen der Teilchengeschwindigkeiten werden sowohl für die Anregungsphase als auch für die Phase des granularen Kühlens bestimmt. Das granulare Kühlen wird bei verschiedenen Dichten untersucht und das Haff'sche Gesetz kann bestätigt werden.

Contents

Chapter 1

Introduction

1.1 Granular Matter

Granular matter is defined as an assembly of macroscopic solid particles. Macroscopic means, that the particles are large enough to not show any significant thermal motion [1]. The most familiar example for granular matter is sand, but also powders, grains, boulders and even the rings of Saturn can be considered a granular material according to the definition above. Because it can be applied to such a variety of systems, granular physics is quite relevant both for understanding phenomena in nature and for optimizing industrial processes.

Granular matter can occur in different states: For instance, sand can behave like a solid when lying still at a beach or in a desert. But it can also behave like a liquid for example in an avalanche or like a gas in a sand storm. However, because thermal movements do not play a role for granular matter[1], none of these states can be described by equilibrium statistical mechanics.

When investigating granular matter, it appears to be reasonable to first distinguish between granular statics (solid-like behavior) and granular

[1]For example, consider a sand grain with a diameter of $2r = 0.1\text{mm}$ and a density of $\rho = 2.5\frac{\text{kg}}{\text{l}}$: This grain has a mass of $\frac{4}{3}\pi r^3\rho \approx 1.3 * 10^{-9}\text{kg}$. For a temperature $T = 300\text{K}$, the sand grain has an average thermal energy $E_T = \frac{3}{2}k_BT \approx 6.21 * 10^{-21}\text{J}$. This energy could only lift the considered grain by $h = \frac{E_T}{mg} \approx 4.87 * 10^{-13}\text{m}$, which is by more than 8 orders of magnitude smaller than the diameter of 10^{-4}m, and therefore negligible. On the other hand, if this grain would move by an average speed of $1\frac{\text{mm}}{\text{s}}$, its temperature would equal $\sim 0.3\text{TK}$.

dynamics (liquid- or gas-like behavior). Both subjects are challenging in different ways:

The problem of granular statics is essentially a problem of mechanical stability in a disordered system. Other than for crystaline solids, for mechanically stable disordered systems there is no generally accepted definition: Some researchers assume that there is a well-defined random-close packing state that disordered systems tend to approach when they are coming to rest [2]. This random-close packing state is often thought of as being geometrically preferred in some way. Therefore, many approaches of explaining random-close packing are based on analysing geometrical properties of packings of spheres [3, 4, 5]. It has been argued, that the properties of a disordered granular solid are mainly determined by the circumstances of its formation [6], e.g. if the grains were shaken more or less before coming to rest. This would make it even more complicated to formulate a theory explaining granular solids, because both statical and dynamical properties of granular matter would have to be considered.

On the other hand, dynamical granular systems show many analogies to classical liquids or gases. For example, one can define a granular temperature $T = \frac{3}{2} < v^2 >$, which can be calculated from the particle velocities v, or define a pressure P for a granular gas. Therefore, upto a certain point it is possible to apply fluid mechanics or gas equations to dynamical granular systems. However, the validity of such analogies is limited, because different from e.g. a molecular gas, a dynamical granular system constantly dissipates kinetic energy due to inelastic particle-particle collisions. Therefore, in order to maintain a dynamical granular state, there has to be a driving mechanism which constantly injects energy to the system (e.g. gravity for an avalanche or air flow for a sand storm). Such systems may reach a steady state, but not an equilibrium state.

The fact that such a dynamical system samples many different states over time, makes it accessible by methods from statistical physics. Thus, investigating dynamical granular systems might be a good starting point for developing a theory of granular matter, which eventually might allow to draw conclusions also about static granular systems. This thesis focuses on investigating dynamical granular systems experimentally in order to increase the amount of empirical knowledge about such systems. Such knowledge might be used as the basis, on which a potential theory of granular matter could be built.

This thesis is seperated into three different parts, which cover three different realizations of granular dynamics:

- In the first part, the dynamics of a single particle within a network of obstacles (Lorentz model) is investigated. This allows to focus on the impact of the geometry of a disordered system on particle dynamics.
- In the second part, a 2D granular gas is investigated at high densities. This means, that the static obstacles from the first part are effectively replaced by moving obstacles, which are the particles of the granular gas hindering each other's movement. Therefore, the dynamics of such a system can not be explained purely geometrically anymore, but result from a combination of geometrical and dynamical factors.
- In the third part, the granular cooling of a 3D granular gas is investigated at low densities. Because a homogenous 3D dilute granular gas is very difficult to achieve in a laboratory experiment, the data resulting from a microgravity campaign is used. Therefore, different from the first two parts, the third part of this thesis is not based on own experiments, but deals with the data analysis for an already existing experiment.

1.2 Lorentz Model

The Lorentz model [7] was originally developed to explain the conductivity of non-homogenous metals. In this model, the interaction of a randomly moving test particle with a network of randomly distributed spherical obstacles is investigated. Every obstacle has the same radius r, while the test particle is point-shaped. The spatial coordinates of the obstacles are drawn from a uniform probability distribution. Consequently, the obstacles are allowed to overlap. With the obstacle radius r and the number density n of obstacles, a dimensionless density n^* can be determined as

$$n^* = r^d n, \tag{1.1}$$

where d is the number of spatial dimensions. The test particle starts with an initial velocity and undergoes elastic collisions with the obstacles, i.e. the particle velocity is conserved. Because the path of the particle does not depend on the initial velocity, the only controling parameter relevant for particle dynamics is the dimensionless density n^*.

For small densities n^*, one would expect a diffusive particle motion in the long time limit, because the obstacles cause random changes in the particle direction, but, on the other hand, do not restrict the particle movement significantly. For high densities n^*, the obstacles restrict the particle motion to such an extend, that the particle can not percolate the system anymore. However, there is no simple argument to predict the exact particle dynamics for intermediate densities.

The particle dynamics in 3D Lorentz models with different densities n^* have been investigated in event driven simulations [8]. The mean-squared displacement $MSD(t)$ has been observed as a function of the time difference t. For low densities n^* (e.g. $n^* = 0.3$ or $n^* = 0.4$), two regimes in the function $MSD(t)$ can be identified:

- For short times, the mean-squared displacement increases quadratically with t, i.e. $MSD(t) \sim t^2$. This indicates a ballistic motion of the particle, which means that it moves with constant velocity in a constant direction[2].
- For long times, the mean-squared displacement crosses over to diffusive dynamics, i.e. $MSD(t) \sim t$. This crossover is caused by the increasing influence of collisions and therefore changes of $\vec{v}$ for longer times.

A ballistic regime at small times is also observed for higher densities n^*. However, at higher densities the mean-squared displacement crosses over to a subdiffusive regime ($MSD(t) \sim t^{\frac{2}{z}}$ with $z > 2$) for indermediate times. For large times, the mean-squared displacement either approaches $MSD(t) \sim t$ again for $n^* < n_c^*$ or approaches a constant value for $n^* > n_c^*$. Thereby, n_c^* is a critical density seperating the densities at which the particle can eventually diffuse through the whole system from those at which the particle is localized by the obstacle network.

The discussed simulation also shows, that the time window of the subdiffusive regime becomes increasingly larger if n_c^* is approached from the side of small densities. For $n^* = 0.84$, the simulation results show a subdiffusive regime $MSD(t) \sim t^{\frac{2}{z}}$ over more than five decades with an exponent of $z \approx 6.25$. This indicates, that this density is very close to the critical

[2]For a particle moving with a constant velocity vector $\vec{v}$, the equation of movement is given by $\vec{r}(t) = \vec{v}(t) + \vec{r}(0)$. This leads to a mean-squared displacement of $MSD(t) =< (\vec{r}(t) - r(\vec{0}))^2 > =< (\vec{v}t)^2 >= v^2t^2$, where v is the absolute value of $\vec{v}$.

density $n_c^{*(3D)}$. Therefore, from the simulation it can be concluded, that

$$n_c^{*(3D)} \approx 0.84. \tag{1.2}$$

For a 2D Lorentz model, simulation results [9] indicate a critical density $n_c^{*(2D)}$ of

$$n_c^{*(2D)} \approx 0.359 \tag{1.3}$$

and the exponent for the subdiffusive regime at the critical density $\sim t^{2/z}$ is found as $z \approx 3.036$.

However, the dynamics of a Lorentz model with a granular particle are still unknown. In particular, using a granular particle means that the collisions become inelastic and that kinetic energy has to be injected continously. For instance, the subdiffusive regime at intermediate time scales might change due to different particle dynamics in a granular Lorentz model.

Therefore, in this thesis a granular Lorentz model experiment is performed and the particle dynamics and the mean-squared displacement are investigated.

1.3 Glass Transition in Dense Granular Fluids

1.3.1 Glass Transition

Most liquids exhibit a glass transition when they are supercooled far enough and crystallization is avoided [15]. This means, that a rapid growth of the viscosity occurs, i.e. the liquid becomes solid-like. However, the glass transition is not a phase transition and a glass does not exhibit long range order, which makes it difficult to give an exact definition of the glass transition. One widely used definition is to define the glass transition temperature T_G as the temperature at which the viscosity of the material reaches a value of $10^{12}\text{Pa} \cdot \text{s}$ [15].

It can be shown that also hard-sphere systems exhibit a glass transition [16, 17, 18]. However, in a hard-sphere systems temperature does only influence the velocities, but not the trajectories of particles. Therefore, the behavior of the system is independent of temperature. This means, that the only parameter which can change the behavior of the system qualitatively is the packing fraction φ. The glass transition in such a system happens, when the system is compressed to a certain packing fraction φ_G

and crystallization is avoided.

It is also possible to define a glassy state as a state, at which the mean-squared displacement of the system approaches a constant value [19]. In contrast, any system in which the mean-squared displacement eventually goes to infinity, is considered a liquid. This definition is particularely useful in simulations or in experiments which allow for the tracking of individual particles. However, in experiments the mean-squared displacement can only be observed for finite times. Therefore, in experiments and simulations, a system is defined as a glass, if the mean-squared displacement seems to be restricted to a finite value *during measurement time*. Hence, this definition becomes increasingly more useful for longer measurement times.

1.3.2 Dense Granular Fluids

Mode-coupling theory [20] calculations predict, that in granular fluids the glass transition density and other properties of the glass transition depend on the coefficient of restitution [21, 22]. This means, that going from an elastic hard-sphere system to a system with dissipative dynamics has a non-trivial influence on the glass transition. However, granular fluids in experiments or in nature do not obey the idealized conditions which are fed into mode-coupling calculations. For example, the driving mechanism, which injects kinetic energy, is more complex. The same is true for the dissipation mechanism: The coefficient of restitution ϵ for particle-particle collisions is in general not a constant, but a function of collision velocity, collision angle and eccentricity. In addition, energy can also be dissipated outside of particle-particle collisions, e.g. by air friction or, especially in 2D systems, by the system boundaries.

Experiments concerning dense 2D granular fluids have been performed already: For a monodisperse layer of vibrated spheres, the system does not show a glassy state, but develops crystaline structures for higher packing fractions instead [23]. Therefore, in order to observe a glassy state, crystalization has to be avoided. One way to avoid crystalization is to use bidisperse instead of monodisperse systems. This has been done in another experiment, using bidisperse mixtures of steal beads driven by a vertical upflow of air [24]. The system exhibits an amorphous state for all

densities, hence crystallization can be avoided successfully. The behavior of the mean-squared displacement varies with density: For low densities, e.g. $\varphi = 48.7\%$, a crossover from ballistic to diffusive motion can be seen. For intermediate and high densities, a crossover to subdiffusive motion is observed. However, the exponent e of the mean-squared displacement $MSD(t) \sim t^e$ starts to increase again for longer times. This is even true for densities as high as $\varphi = 80.9\%$. However, the time of measurement is not long enough to see if the mean-squared displacement returns to a diffusive behavior eventually for all densities.

Mode-coupling theory predicts, that the mean-squared displacement approaches a constant value for a glass also in two dimensions [27]. The fact, that such an behavior of mean-squared displacements could not be observed even at densities as high as $\varphi = 80.9\%$, can have a variety of reasons:

1. The glass transition in the investigated system might only occur at densities above 80.9%.

2. The mode-coupling predictions may not hold for either granular fluids in general or for the specific dynamics of 2D granular particles driven by an vertical airflow.

3. It is possible, that the used image processing algorithm mixes up neighboring particles occasionally. This would lead to a apparent growth of the mean-squared displacement at long times, even within the glassy state (for a detailed discussion, see section 4.2.1).

In this thesis, a bidisperse 2D granular fluid driven by a vertically vibrated baseplate is investigated. The main goal of this experiment is the investigation of a potential glass transition in a granular fluid. The granular particles are realized by cylinders with spherical caps. While the cylindrical part of the particles ensures a disk-like collision behavior, the spherical cap allows for efficient driving by vertical vibrations. Each particle is tagged with an individual, machine-readable code. This allows measurements with small frame rates, since the particles do not have to be tracked on a frame-to-frame basis. Therefore, it is possible to observe the system also for longer times without producing an extreme amount of raw image data. The individual tagging of particles also adresses the potential problem of image processing errors, because it becomes less likely to confuse the different particles.

1.4 Granular Cooling

If the injection of kinetic energy into a granular gas is stopped, the total amount of kinetic energy of the system starts to decrease due to inelastic collisions. In order to describe this behavior, it is useful to define a granular temperature T as

$$T = \frac{d}{2} < v^2 >, \tag{1.4}$$

where d is the number of spatial dimensions and v are the velocities of individual particles. Consequently, the loss of kinetic energy in a granular gas without continous energy injection is referred to as *granular cooling*. The time-evolution of such a system can be explained by Haff's Law [28], which is given as

$$< v(t) >= \frac{< v(0) >}{1 + \frac{t}{\tau_H}} \tag{1.5}$$

The time τ_H defines a time scale of the cooling process and depends on the average initial velocity $< v(0) >$, the mean free path s and the coefficient of restitution ϵ of particle-particle collisions. Haff's Law was intially derived from hydrodynamic equations [28]. However, it can also be derived as follows[3]:

The change in kinetic energy during a collision is given by

$$E'_{\text{kin}} = E_{\text{kin}}(1 - \epsilon^2) \tag{1.6}$$

As long as no clustering [31] occurs, a homogenous system can be assumed. In such a system, the rate r_c of collisions can be calculated from the mean free path s as:

$$r_c = \frac{s}{< v >} \tag{1.7}$$

Using equations (1.6) and (1.7), a differential equation for the granular temperature can be formulated as

$$\frac{d}{dt}T = -\frac{1 - \epsilon^2}{s/ < v >}T \tag{1.8}$$

With equation (1.4), this can be written as

$$\frac{d}{dt} < v^2 >= -\frac{1 - \epsilon^2}{s} < v >< v^2 > \tag{1.9}$$

[3]This derivation is enhancing a motivation of Haff's Law given in [30].

Provided that the shape of the velocity distribution does not change over time, the quantity $< v^2 >$ only deviates from $< v >^2$ by a constant factor α:

$$< v^2 >= \alpha < v >^2 \tag{1.10}$$

This can be inserted into equation (1.9) as

$$\frac{d}{dt}\alpha < v >^2 = -\frac{1-\epsilon^2}{s} < v > \alpha < v >^2, \tag{1.11}$$

which leads to:

$$\frac{d}{dt} < v >^2 = -\frac{1-\epsilon^2}{s} < v >^3 \tag{1.12}$$

This equation can now be transformed to

$$2 < v > \frac{d}{dt} < v >= -\frac{1-\epsilon^2}{s} < v >^3 \tag{1.13}$$

which allows to devide both sides by $< v >$:

$$2\frac{d}{dt} < v >= -\frac{1-\epsilon^2}{s} < v >^2 \tag{1.14}$$

Now the Ansatz

$$< v(t) >= \frac{< v(0) >}{1 + \frac{t}{\tau_H}} \tag{1.15}$$

is chosen and its first time derivation is calculated as

$$\frac{d}{dt} < v(t) >= -(\frac{< v(0) >}{1 + \frac{t}{\tau_H}})^2 \frac{1}{\tau_H} \tag{1.16}$$

Inserting this into equation (1.14) gives

$$-2(\frac{< v(0) >}{1 + \frac{t}{\tau_H}})^2 \frac{1}{\tau_H} = -\frac{1-\epsilon^2}{s}(\frac{< v(0) >}{1 + \frac{t}{\tau_H}})^2 \tag{1.17}$$

This proves the validity of the above Ansatz. Further, it can be transformed to the following equation

$$-\frac{2}{\tau_H} = -\frac{1-\epsilon^2}{s}, \tag{1.18}$$

which allows to calculate the Haff time τ_H as

$$\tau_H = \frac{2s}{1-\epsilon^2}. \tag{1.19}$$

With $s = \frac{1}{n\sigma}$, where n is the number density and σ is the cross section of the particles, this can also be written as

$$\tau_H = \frac{2}{(1-\epsilon^2)n\sigma}. \tag{1.20}$$

Haff's Law seems to be a quite robust phenomenon. For instance, already for the case of a single particle cooling between two walls, a Haff-like behavior can be predicted (cf. sect. A.1).

Haff's Law has already been tested in a magnetically levitated granular gas [30]. However, the investigated granular gas consists only of about 40 particles. Also, the levitating field is not completely homogenous, which causes the particles to form an increasingly large cluster in the field minimum. Therefore, in this experiment only very few particles remain moving freely outside the cluster for a longer time. This means, that the measurement of the average velocity in the long time regime relies on $1-3$ particles only.

In micro gravity experiments, no levitating field is needed and consequently no field minimum exists. Therefore, it makes sense to use micro gravity experiments to further investigate Haff's Law.

In this thesis, the data analysis for a drop tower experiment is performed in order to investigate the temporal evolution of the mean velocity $< v(t) >$ and the shape of the velocity distribution for different granular gases.

Chapter 2

Driving of Granular Particles in Two Dimensions

2.1 Driving Mechanism

In order to investigate granular dynamics in two dimensions, a mechanism to inject kinetic energy into the sample has to be developed. The goal of such a mechanism is to excite one or more particles in a way, that they perform a random and isotropic horizontal movement. This can be either achieved by

- horizontal driving from the boundaries, e.g. electromagnetic actuators [32] or by
- vertical driving by a vibrating surface.

For vertical driving, a homogenously vibrated surface is needed. While vibrating a surface is not a problem itself, vibrating in a controlled and homogenous way takes some effort. For instance, the driving force needs to be transmitted from its source to all parts of the surface without applying bending stresses to it.

A well controlled vibration of a big area can be achieved by using industrial vibrating tables (cf. fig. 2.1). Such a vibrating table uses an osillating magnetic field in order to produce vertical vibrations. Those vibrations are then transmitted via a massive metal block (headexpander) to a baseplate, to which an experiment can be attached. Such a headexpander is needed in order to avoid resonances or bending of the baseplate. If the baseplate area is increased, also the size and weight of the headexpander has to be increased. This requires a higher driving force and therefore a stronger

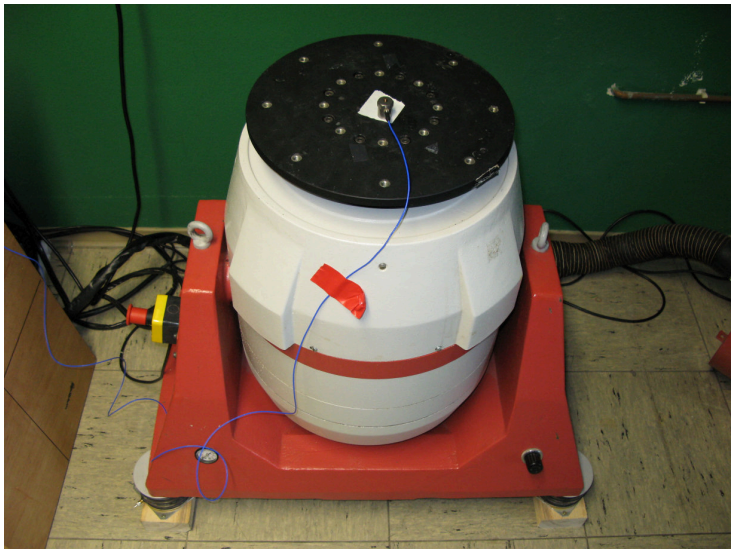

Figure 2.1: The LDS V721 vibrating table used for this thesis. The black top plate of the vibrating table can be vibrated vertically by different frequencies and amplitudes. An acceleration sensor (on top of the vibrating table, connected by a blue wire) is used to controll the top plate oscillation by a feed-back loop.

vibrating table. Thus, the size of the experimental area is limited by the power of the used vibrating table.

For driving from the boundary, such restrictions do not apply: Because the baseplate does not move, there is no size limit for the experimental setup. However, particles can only gain kinetic energy by either

- collisions with the walls or
- collisions with other particles.

First, this means that certain setups, like measurements of one-particle-dynamics in a network of obstacles, can not be realized with driving from the boundaries at all, because the particle does not touch the walls often enough to gain kinetic energy consistently.

But also for 2D granular gases without obstacles, driving from the boundaries has an important disadvantage: Particle-particle collisions are an essential feature of the dynamics of granular gases. In order to have a system dominated by particle-particle collisions, the mean free path needs

to be small compared to the system size. At each collision, the kinetic energy of a particle is reduced by ϵ, where ϵ is the coefficient of restitution. Therefore, if the system radius equals n times the mean free path, the average kinetic energy of a particle travelling from the boundaries to the centre of the system is reduced by a factor ϵ^n. This leads to a lower average kinetic energy in the bulk than at the boundaries of the system and therefore makes the system inhomogenous.

This mechanism can even cause a situation, where the particles in the centre of the system do not move at all, although the system is constantly driven from the walls[1]. In addition, the energy transport within such a system depends highly on the coefficient of restitution ϵ. Therefore, it would be very difficult to investigate systems with high ϵ or to compare the granular dynamics of systems with different ϵ.

In summary, driving from the boundaries has many intrinsic limitations, which become particularly relevant for interesting experimental setups like dense systems or systems with small ϵ. On the other hand, driving by vertical vibrations does not have any intrinsic limitations, but is only limited by the power of the vibrating table.

Therefore, a vertical shaking setup is chosen: A LDS V721 vibrating table with a suitable headexpander is used in order to employ a defined vertical oscillation to a $500 * 500\text{mm}^2$ baseplate. This vibrating table is able to produce oscillation frequencies between 5Hz and 4000Hz with a peak force of about 4000N. With a total weight of headexpander and experiment of $\approx$ 20kg and a reasonable margin of safety, this allows a peak acceleration of about 10g. Due to the construction of the vibrating table, the maximum amplitude of the oscillation is 12.7mm. For sine-shaped vibrations, the relation of amplitude A, peak acceleration a and frequency f is given as

$$a = A(2\pi f)^2 \tag{2.1}$$

The actual oscillation frequency and amplitude can then be optimized in order to achieve an optimal driving of the particles.

[1] An interesting example for this can be seen in a microgravity experiment described in [33]: Granular particles are driven by the walls of a container. For certain packing fractions, this leads to a motionless dense cluster of particles in the centre of the container, although the walls of the container are still moving.

2.2 Dynamics of a Point-Shaped Particle

A crucial point of the driving mechanism is the dynamics of individual particles. The particles has to be driven in a way that

1. all particles can gain kinetic energy,
2. the resulting movement of the particles is random and
3. the particles are restricted to a 2D-movement, e.g. do not slip on top of each other.

In order to fulfill all three conditions, the particle shape, the parameters of the driving oscillation and the experimental setup have to be chosen accordingly. For this, a good understanding of the driving mechanism is needed. Therefore, first the dynamics of a point-shaped particle on an oscillating surface is discussed.

2.2.1 Vertical Movement of Inelastic Particles

Consider a totally inelastic particle ($\epsilon = 0$) on a surface which performs a sine-shaped vibration with an oscillation frequency $\omega = 2\pi f$, an amplitude A and a peak acceleration a. If a particle is placed on that surface, it will stay there unless the surface accelerates downwards with more than one g. If this happens, the particle crosses over to free fall, until it hits the vibrating surface again.

The z-position of the vibrating surface as a function of the time t is given as:

$$z(t) = A \sin(\omega t) \tag{2.2}$$

Then the velocity $\dot{z}(t)$ and the acceleration $\ddot{z}(t)$ of the surface are given as

$$\dot{z}(t) = A\omega \cos(\omega t) \tag{2.3}$$

and

$$\ddot{z}(t) = -A\omega^2 \sin(\omega t). \tag{2.4}$$

With this, the peak acceleration a can be expressed as

$$a = A\omega^2. \tag{2.5}$$

For convenience, a dimensionless peak acceleration G is defined as

$$G = \frac{a}{g} = \frac{A\omega^2}{g}. \tag{2.6}$$

Now the time t_J, at which the surface moves downwards with $\ddot{z}(t_J) = -g$, can be calculated from (2.4) and (2.6):

$$t_J = \frac{1}{\omega} \arcsin \frac{g}{A\omega^2} = \frac{1}{\omega} \arcsin \frac{1}{G} \tag{2.7}$$

The velocity of the surface v_J at the time t_J can then be calculated as follows:

$$v_J = \dot{z}(t_J) = A\omega \cos(\omega t_J) = A\omega \cos(\arcsin \frac{1}{G}) = A\omega \sqrt{1 - \frac{1}{G^2}} \tag{2.8}$$

Also, the vertical position z_J at which the particle leaves the surface can now be calculated as

$$z_J = z(t_J) = A \sin(\omega \frac{1}{\omega} \arcsin \frac{1}{G}) = \frac{A}{G} \tag{2.9}$$

Now t_M is defined as the time the particle needs to reach its maximum height after departing from the vibrating surface. Using equation (2.8), it can be calculated as

$$t_M = \frac{v_J}{g} = \frac{A\omega}{g} \sqrt{1 - \frac{1}{G^2}} = \frac{G}{\omega} \sqrt{1 - \frac{1}{G^2}} = \frac{1}{\omega} \sqrt{G^2 - 1} \tag{2.10}$$

The maximum height z_M of the particle is calculated as

$$z_M = z_J + \frac{g}{2} t_M^2 = \frac{A}{G} + \frac{g}{2\omega^2}(G^2 - 1) \tag{2.11}$$

$$= \frac{A}{G} + \frac{A}{2G}(G^2 - 1) = \frac{AG}{2} + \frac{A}{2G} \tag{2.12}$$

However, the maximum height h_M the particle reaches relative to the vibrating surface is more relevant than the maximum height z_M the particle reaches relative to the rest position of the surface. For large peak accelerations G, the peak-peak distance of the vibrating surface $2A$ is small compared to z_M. Therefore, in this case the approximation

$$h_M \approx z_M = A(\frac{G}{2} + \frac{1}{2G}) \approx \frac{AG}{2} \tag{2.13}$$

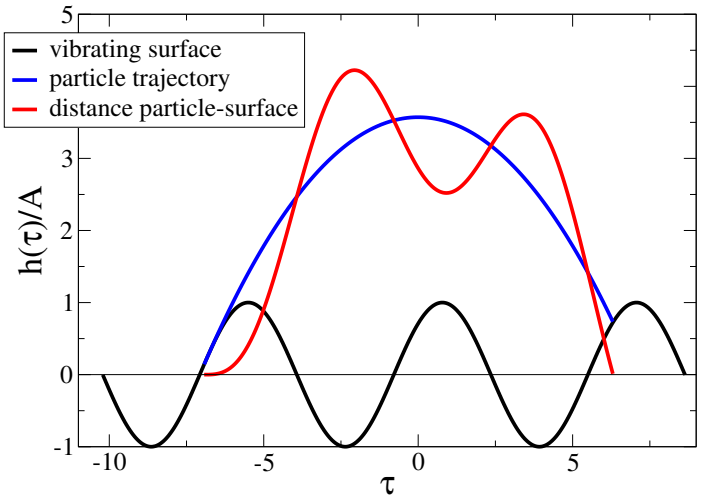

Figure 2.2: The normalized particle-surface distance $\frac{h(\tau)}{A}$ as a function of $\tau = \omega(t - t_M - t_j)$ is calculated as the difference between the absolute particle height and the surface position for a normalized peak acceleration $G = 7$.

is feasible. On the other hand, for small G the movement $z(t)$ of the surface influences h_M significantly and has to be considered. Therefore, the time-dependent distance $h(t)$ between particle and surface has to be calculated and its maximum h_M has to be found (cf. fig. 2.2).

For this purpose, first a variable $\tau = \omega(t - t_M - t_J)$ is defined. Then the distance between particle and surface $h(\tau)$ can be written as:

$$h(\tau) = z_M - \frac{g}{2}(\frac{\tau}{\omega})^2 - A\sin(\tau + \omega(t_M + t_J)) \tag{2.14}$$

$$h(\tau) = \frac{AG}{2} + \frac{A}{2G} - \frac{g}{2\omega^2}\tau^2 - A\sin(\tau + \sqrt{G^2 - 1} + \arcsin\frac{1}{G}) \tag{2.15}$$

Accordingly, $H := \frac{h(\tau)}{A}$ can be written as

$$H(\tau) = \frac{h(\tau)}{A} = \frac{G}{2} + \frac{1}{2G} - \frac{g}{2A\omega^2}\tau^2 - \sin(\tau + \sqrt{G^2 - 1} + \arcsin\frac{1}{G}) \tag{2.16}$$

$$H(\tau) = \frac{G}{2} + \frac{1}{2G} - \frac{\tau^2}{2G} - \sin(\tau + \sqrt{G^2 - 1} + \arcsin\frac{1}{G}) \tag{2.17}$$

The dimensionless quantity $H(\tau)$ depends only on the peak acceleration G. This means that the shape of the function $h(t)$ depends solely on the peak

G	2	3	4	5	6	7
H_M	1.27	2.37	3.09	3.59	3.95	4.22

Table 2.1: Normalized peak heights of inelastic particles on a vertically vibrated surface for different peak velocities of a sine-shaped surface vibration. The peak height H_M is given in units of the vibration amplitude.

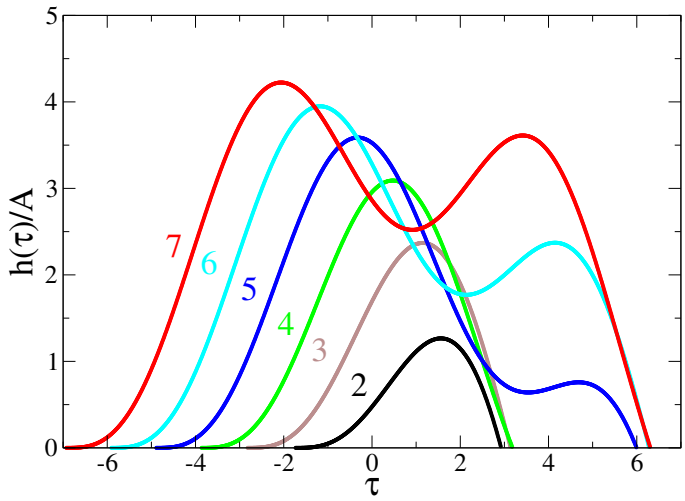

Figure 2.3: Dimensionless trajectories of inelastic particles on a vibrating surface for different dimensionless peak accelerations G, which are indicated by numbers in the plot. The red curve is the same as shown in figure 2.2.

acceleration G, while the quantities A and ω are prefactors, which define the spatial and temporal dimension of $h(t)$.

The maxima H_M of the function $H(\tau)$ are obtained numerically for different peak accelerations G and shown in table 2.1 For $G \leq 1$, the particle does not leave the surface at all and therefore $\frac{h_M}{A}$ is always zero. For $G \gg 1$, one can see from equation (2.13) that H_M can be approximated as

$$H_M \approx \frac{G}{2} \tag{2.18}$$

Once the value H_M is known for all relevant peak accelerations G, the maximum height h_M can then be calculated from the oscillation frequency

$f = \frac{\omega}{2\pi}$ and the peak acceleration G as follows:

$$h_M(G, f) = AH_M(G) = \frac{Gg}{\omega^2} H_M(G) = \frac{Gg}{(2\pi f)^2} H_M(G) \tag{2.19}$$

2.2.2 Elastic Particles

If the coefficient of restitution ϵ becomes greater than zero, the dynamics become considerably more complicated: For $\epsilon = 0$, a particle can only leave the vibrating surface excactly at the moment t_J, when the surface's downward acceleration exceeds $1g$:

$$\ddot{z}(t_J) = -g \tag{2.20}$$

On the other hand, if a particle performs an elastic collision with the surface ($\epsilon > 0$), it can keep some of its kinetic energy. This means, that it can leave the surface again immediately, no matter how much the surface is accelerating or decelerating at that moment. Therefore, one gets for the starting time t_J of a particle jump:

$$\ddot{z}(t_J) \geq -g \tag{2.21}$$

Times with $\ddot{z}(t) < -g$ are still excluded, because a free-falling particle can not collide with the surface when it accelerates downwards with more than $1g$. The time t_J and therefore the velocity $v_J = \dot{z}(t)$ now depends on the preceding jump of a particle which again depends on the jump before. Therefore, in most cases the trajectory of a particle will become unpredictable very soon. This also makes it very difficult to estimate the largest height a particle can gain relative to the surface.

However, an upper treshold $h_M^M(G, f)$ for the relative particle height can be estimated as follows: Using equation (2.6), the maximum velocity $\dot{z}_M$ of the surface is given as

$$\dot{z}_M = A\omega = \frac{gG}{\omega}. \tag{2.22}$$

When a particle with velocity $\vec{v}$ collides with a surface which moves with velocity $\dot{z}$, the velocity $\vec{v'}$ of the particle after the collision is given by

$$\vec{v'} - \vec{\dot{z}} = -\epsilon(\vec{v} - \vec{\dot{z}}). \tag{2.23}$$

This can be transformed to:

$$\vec{v'} = -\epsilon\vec{v} + (1 + \epsilon)\vec{\dot{z}} \tag{2.24}$$

Because all vectors are parallel to each other, this can also be written as a scalar equation:

$$v' = \epsilon v + (1 + \epsilon)\dot{z} \tag{2.25}$$

Now, using the maximum surface velocity $\dot{z}_M$, an upper treshold of the velocity v' after the collision can be given by

$$v' \leq \epsilon v + (1 + \epsilon)\dot{z}_M \tag{2.26}$$

With the assumption that the particle velocity v directly before a collision can not exceed the maximum possible particle velocity v_M, this maximum velocity v_M can be calculated: The maximum velocity v_M is reached directly after a collision under optimal conditions. Those optimal conditions are met when both the particle velocity before the collision and the surface velocity are at their maxima:

$$v_M = \epsilon v_M + (1 + \epsilon)\dot{z}_M \tag{2.27}$$

Now v_M can be calculated as

$$v_M = \frac{1 + \epsilon}{1 - \epsilon}\dot{z}_M \tag{2.28}$$

With equation (2.22), this can be written as:

$$v_M = \frac{gG}{\omega}\frac{1 + \epsilon}{1 - \epsilon} \tag{2.29}$$

The upper treshold $h_M^M(G, f)$ of the height can then be estimated as:

$$h_M^M \approx \frac{1}{2}g(\frac{v_M}{g})^2 + A = \frac{v_M^2}{2g} + A \tag{2.30}$$

The summand A is caused by the fact that the surface position at the peak height is unknown and h is defined as the distance between surface and particle. With equation (2.22) and equation (2.6), this can be transformed to

$$h_M^M \approx \frac{g^2G^2}{2q\omega^2}\frac{(1 + \epsilon)^2}{(1 - \epsilon)^2} + \frac{gG}{\omega^2} = \frac{gG}{\omega^2}(\frac{G}{2}\frac{(1 + \epsilon)^2}{(1 - \epsilon)^2} + 1) \tag{2.31}$$

With $\omega = 2\pi f$, one can finally write:

$$h_M^M(G, f, \epsilon) \approx \frac{gG}{4\pi^2 f^2}(\frac{G}{2}\frac{(1 + \epsilon)^2}{(1 - \epsilon)^2} + 1) \tag{2.32}$$

For large G or large ϵ, the second summand can be dropped and one gets[2]:

$$h_M^M(G, f, \epsilon) \approx \frac{gG^2}{8\pi^2 f^2} \frac{(1+\epsilon)^2}{(1-\epsilon)^2} \tag{2.33}$$

This equation can now be compared to the large-G-limit of the maximum height $h_M(G, f)$ for the inelastic case, which can be derived from equation (2.18) and equation (2.19) as

$$h_M(G, f) = \frac{Gg}{4\pi^2 f^2} H_M(G) \approx \frac{Gg}{4\pi^2 f^2} \frac{G}{2} = \frac{gG^2}{8\pi^2 f^2} \tag{2.34}$$

Therefore, for large peak accelerations G the following relation is valid:

$$h_M^M(G, f, \epsilon) \approx h_M(G, f) \frac{(1+\epsilon)^2}{(1-\epsilon)^2} \tag{2.35}$$

This means, that in the large-G-limit the upper threshold of the jump height of elastic particles can be calculated by multiplying the inelastic jump height $h_M(G, f)$ by a factor $\frac{(1+\epsilon)^2}{(1-\epsilon)^2}$.

2.2.3 Horizontal Movement

The horizontal movement of particles is caused by the roughness of the surface: If a particle collides with a point of the surface, which is not completely leveled, it can pick up some horizontal velocity. If the horizontal velocity and the jump time are small, a particle might still get stuck at some local minimum of the surface, because it can not move far enough between two collisions to escape from that minimum. Therefore, some minimum jump height and jump time are required in order to allow for a effective horizontal particle movement. Those requirements have to be determined experimentally.

However, once the requirements are met, a random horizontal movement can be achieved. This is, because the roughnesses of the surface, which controls the direction of the movement, are randomly distributed.

[2]For a comparison of equation (2.33) with observed particle trajectories, see section 2.2.3.

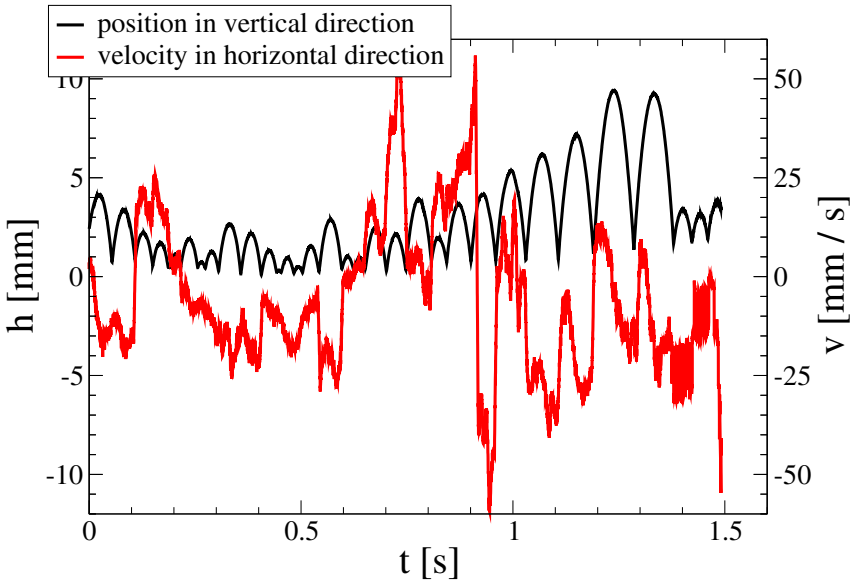

Figure 2.4: Movement of a 8mm polyester resin sphere on a vibrating surface with frequency $f = 156$Hz and peak acceleration $a = 7$g. The evolution of vertical positions and horizontal velocities is shown over a time period of ~ 1.5s.

2.3 Spherical Particles

In order to investigate the dynamics of spherical particles on a vibrating surface, a polyester resin sphere with a diameter of 8mm is put on a vibrating epoxi plate. Randomly ordered vertical needles are attached to the surface and act as obstacles. The vibrating table performs a sine-shaped oscillation with a frequency of $f = 156$HZ and a peak acceleration of $a = 7$g. The movement of the sphere in an x-z-plane is filmed by a Phantom V10 high speed camera (cf. fig. 2.4). The coefficient of restitution is determined as $\epsilon \approx 0.8$ in a seperate measurement by dropping the polyester resin sphere from a height of 100mm.

In figure 2.4, the largest observed height amounts to about 10mm. This is consistent with equation (2.33), which predicts a maximum height h_M^M of

$$h_M^M(G, f, \epsilon) \approx \frac{gG^2}{8\pi^2 f^2} \frac{(1+\epsilon)^2}{(1-\epsilon)^2} = 20.3\text{mm} \tag{2.36}$$

The amplitude A of the vibrating table oscillation is given as $A = \frac{a}{\omega^2} \approx 0.092\text{mm}$, which is two orders of magnitude smaller than the largest observed jump height of the sample sphere.

From figure 2.4, it can be seen, that the particle collides with the surface 31 times during a time interval of $\sim 1.6\text{s}$. This equals a collision frequency of about 20Hz. However, the jump height, and therefore the collision frequency varies greatly with time.

The horizontal x-movement changes rapidly at the times when the particle touches the surface, which confirms that the horizontal movement is caused by changes in the particle direction during collisions. In addition, the horizontal velocity also changes significantly in between particle-surface collisions, which is due to collisions with the obstacles. The highest observed horizontal velocity is about $0.05\frac{m}{s}$. This can be compared to the highest vertical velocity v, which can be calculated from the largest observed height h of 0.01m by

$$v = \sqrt{2gh} = 0.443\frac{m}{s} \tag{2.37}$$

This indicates, that only a small fraction of the total kinetic energy can be transformed into horizontal movement, which is probably due to the relative flatness of the surface. However, the achieved horizontal velocity is high enough to allow the particle to move randomly through the whole system, e.g. it does not get stuck at local roughnesses at the surface.

The vertical movement can also be evaluated in a quantitative way in order to confirm if the particle trajectory is consistent with a coefficient of restitution $\epsilon \approx 0.8$. This is necessary, because the coefficient of restitution might depend on the impact velocity and might therefore in some cases deviate from the measured $\epsilon \approx 0.8$. In order to determine the ϵ of individual collision, first the impact velocities v have to be determined. This can be done by using the temporal distances dt of collisions (c.f. fig 2.5) with following equation:

$$v = \sqrt{2gh} = \sqrt{2g\frac{g}{2}(\frac{dt}{2})^2} = \frac{g}{2}dt \tag{2.38}$$

The vertical particle velocity v' after the collsion is assumed to be equal to the impact velocity of the next collision and can therefore be determined by the same equation. However, in order to determine ϵ, also the velocity

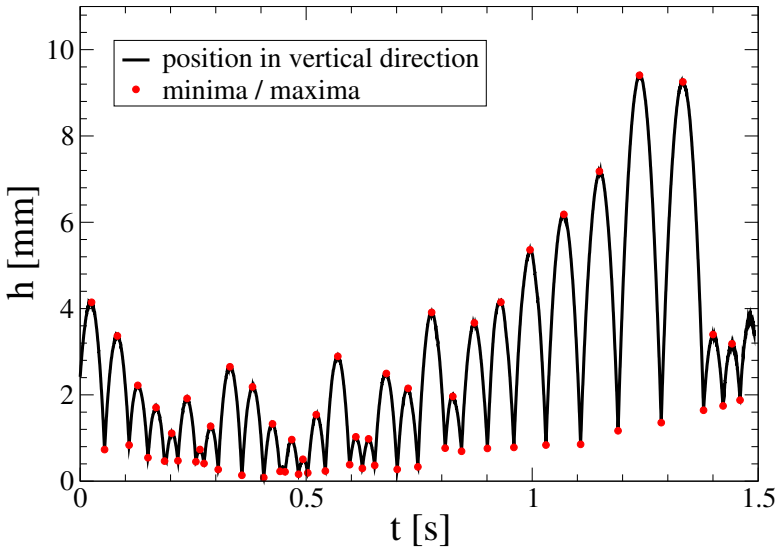

Figure 2.5: Minima and maxima of the height of a 8mm polyester resin sphere above a vibrating surface with frequency f = 156Hz and peak acceleration a = 7g. The minimum height is moving with time due to roughnesses of the baseplate.

v_s of the vibrating surface at the collision has to be known. Because the amplitude of the vibrating surface $A = \frac{gG}{(2\pi f)^2} = 7.1 * 10^{-6}$m is very small, the surface vibration can not be measured by the high speed camera. On the other hand, an upper and a lower threshold for ϵ can be determined by assuming that the surface is moving downwards or upwards, respectively, with its maximum velocity v_s^M, which is given as

$$v_s^M = A\omega = \frac{Gg}{2\pi f} = 0.0701\frac{m}{s} \tag{2.39}$$

For the case of maximum upward velocity, the collision can be described by the following equation:

$$v' - v_s^M = \epsilon(v + v_s^M) \tag{2.40}$$

For the case of maximum downward velocity, the corresponding equation is given as:

$$v' + v_s^M = \epsilon(v - v_s^M) \tag{2.41}$$

Provided that the measured velocities v and v' are fixed, the upper threshold ϵ_U of ϵ can be retrieved from the case of maximum downward movement, while the lower threshold ϵ_L is given by the case of maximum upward velocity. Therefore, from equation (2.41) and equation (2.40), one can derive

$$\epsilon_U = \frac{v' + v_s^M}{v - v_s^M} \tag{2.42}$$

and

$$\epsilon_L = \frac{v' - v_s^M}{v + v_s^M}. \tag{2.43}$$

In addition, a coefficient of restitution ϵ_0 for the case that the baseplate does not move during collision can be calculated as:

$$\epsilon_0 = \frac{v'}{v} \tag{2.44}$$

Now, from the collision times, the impact velocities and the lower and upper threshold for ϵ and the value ϵ_0 are calculated and shown in table 2.2.

For the collision at $t = 0.4422$s no values have been calculated, because the jump between $t = 0.4256$s and $t = 0.4422$s is too small for a well-defined measurement. The upper and lower thresholds ϵ_U and ϵ_L, as well as the

t/s	dt/s	$v_{\mathrm{impact}}/\frac{\mathrm{m}}{\mathrm{s}}$	ϵ_L	ϵ_0	ϵ_U
0.0541					
0.1083	0.0542	0.2659	0.40	0.77	1.40
0.15	0.0417	0.2046	0.40	0.88	1.86
0.1867	0.0367	0.1801	0.30	0.80	1.95
0.2163	0.0295	0.1448	0.58	1.35	3.55
0.2561	0.0398	0.1954	0.07	0.45	1.26
0.2741	0.0180	0.0881	0.53	1.75	12.40
0.3055	0.0314	0.1541	0.83	1.67	3.89
0.3578	0.0523	0.2567	0.51	0.93	1.65
0.4063	0.0484	0.2376	0.35	0.74	1.47
0.4422	-	-	-	-	-
0.4831	0.0298	0.1464	0.14	0.69	2.23
0.5036	0.0205	0.1004	0.70	1.89	8.57
0.5423	0.0388	0.1901	0.75	1.39	2.79
0.5963	0.0539	0.2644	0.20	0.52	1.07
0.6244	0.0281	0.1380	0.30	0.97	3.00
0.6516	0.0272	0.1334	0.86	1.83	4.97
0.7014	0.0498	0.2445	0.49	0.92	1.69
0.7472	0.0458	0.2246	0.77	1.32	2.37
0.8075	0.0603	0.2958	0.29	0.60	1.10
0.8438	0.0363	0.1778	0.85	1.58	3.25
0.9009	0.0572	0.2805	0.62	1.02	1.70
0.9595	0.0586	0.2874	0.78	1.21	1.92
1.0305	0.0709	0.3480	0.73	1.08	1.61
1.1072	0.0767	0.3763	0.75	1.08	1.56
1.19	0.0828	0.4062	0.84	1.15	1.60
1.2855	0.0955	0.4683	0.72	0.98	1.33
1.3791	0.0936	0.4591	0.27	0.46	0.73
1.4223	0.0433	0.2123	0.40	0.87	1.79
1.4598	0.0375	0.1839			

Table 2.2: Lower thresholds ϵ_L, values for a not moving baseplate ϵ_0, and upper thresholds ϵ_U of possible coefficients of restitution ϵ of the test particle. The thresholds are calculated from the observed collision times of subsequent collisions of a test particle with a vibrating surfaced.

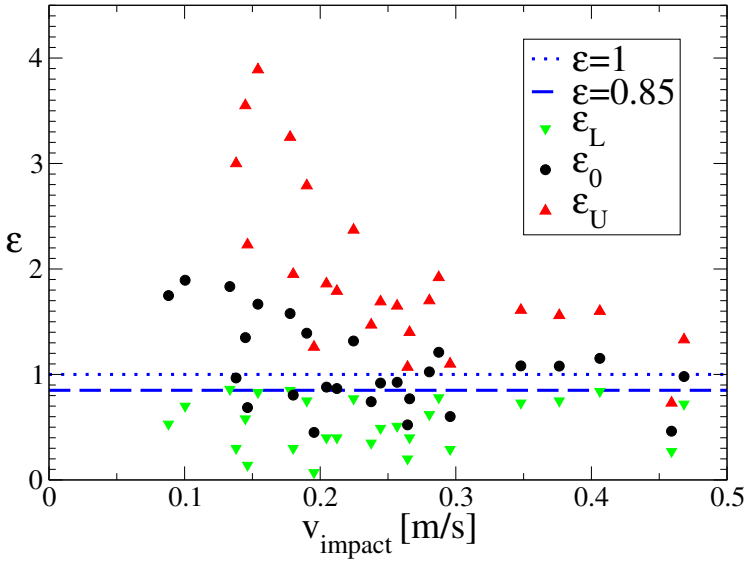

Figure 2.6: Apparent coefficients of restitution ϵ for a 8mm polyester resin sphere for different impact velocities. Upper thresholds ϵ_U, values from assuming no baseplate movement ϵ_0, and lower thresholds ϵ_L are shown. The horizontal lines at $\epsilon = 0.85$ and $\epsilon = 1$ indicate the range of possible values of the ϵ of the sphere-surface collision.

values for a not moving baseplate ϵ_0, for different impact velocities v_{impact} are plotted in figure 2.6. The plot indicates, that $\epsilon \geq 0.85$. This is a little larger than the $\epsilon \approx 0.8$ measured by dropping the sphere from a height of 100mm. This deviation might be caused by a slight velocity dependence of ϵ. On the other hand, the measured ϵ_L in figure 2.6 might also be heigher than the actual ϵ in some cases: The horizontal velocity can also be transformed back to vertical velocity during a collision. This might cause the vertical velocity to grow during a collision by a bigger amount than what one would expect from the driving by the shaker and the vertical velocity v_z before the collision.

Therefore, one can conclude that the trajectory shown in figure 2.4 and figure 2.5 is consistent with the measured $\epsilon \approx 0.8$ of the polyester resin sphere.

2.4 Disks

For a 2D granular experiment, another interesting option is to choose disk-shaped particles. However, the dynamics of disks on a vibrating surface is much more complicated than the dynamics of a spherical particle: For instance, if a disk collides with the surface, the course of this collision depends very much on the tilting angle of the disk in the moment of collision: If the disk is parallel to the surface, its whole area collides with the surface at virtually the same moment. However, if the disk is significantly tilted, it collides with one side first and therefore experiences a significant torque. Also the coefficent of restitution ϵ depends on the exact course of a collision. This means that the dynamics of disks on a vibrating surface is very difficult to predict by mathematical considerations.

The dynamics of various non-spherical particles on vibrating surfaces have already been investigated. For example, a dimer consisting of two spheres connected by a rod can perform horizontal drifting on a vibrated surface[3] [34]. The dynamics of the dimer depend on the driving parameters like oscillation frequency and peak acceleration. However, the exact dynamics of disks on a vibrating surface are still unknown and therefore have to be investigated.

2.4.1 Dynamics of Disks on a Vibrating Surface

In order to investigate the dynamics of disks on a vibrating surface experimentally, twenty polyethylen disks are put into a confined area and their behavior is observed for different oscillations. Because for many purposes bidisperse disks are needed, ten of the disks have a diameter of 15mm, while the other ten have a diameter of 18mm. The height of all disks is 2mm.

Five qualitatively different kinds of disk behavior are observed. Those states are listed in table 2.3.

Table 2.4 and figure 2.7 show a number of measurements for different peak accelerations and frequencies with the observed states (1-5).

[3] Similiar self-propelled particles are described in section A.2.

State	Description
1	The disks do not move in x-y-directions.
2	Some disks are moving slowly in the beginning. However, after a short time they tend to get stuck at the system boundaries or to form big clusters of disks which do not move anymore.
3	Some disks are moving lively, while most of the disks do not move at all.
4	Some disks are agitated to an extent that they can jump on top of other disks or flip around. On the other hand, there are also still disks which do not move at all.
5	All disks are moving around wildly. Some of them flip around frequently or even jump across the system boundaries.

Table 2.3: Definition of five different possible behaviors of disks on a vibrated surface.

	2g	3g	5g	7g
20 Hz	**5**	-	-	-
25 Hz	**4**	-	-	-
30 Hz	**4**	**5**	-	-
40 Hz	**3**	**4**	-	-
50 Hz	**3**	**3**	**5**	-
70 Hz	**3**	**3**	**4**	**5**
100 Hz	**2**	**3**	**3**	**4**
150 Hz	**2**	**2**	**2**	**3**
200 Hz	**2**	**2**	**2**	**3**
250 Hz	**1**	**2**	**2**	**2**
300 Hz	-	**2**	**2**	**2**
400 Hz	-	**2**	**2**	**2**
500 Hz	-	**1**	**2**	**2**
700 Hz	-	-	**2**	**2**
1000 Hz	-	-	**1**	**2**
1500 Hz	-	-	-	**1**

Table 2.4: Dynamics of disks on a vibrated surface. The definition of the different kinds of dynamic behavior are listed in table 2.3.

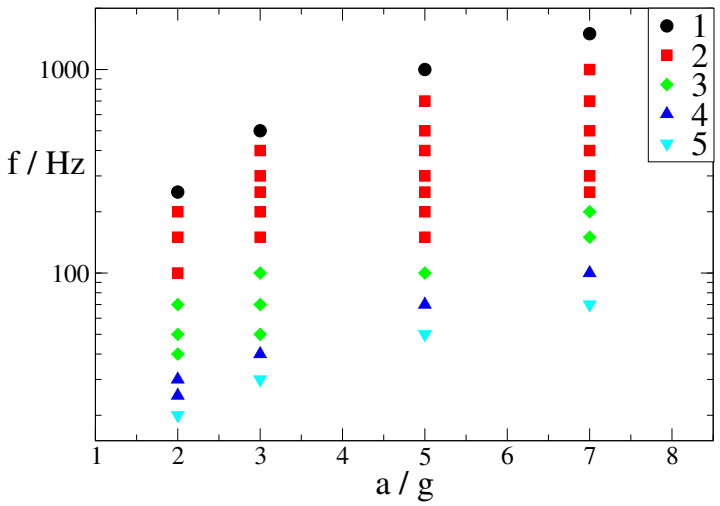

Figure 2.7: Dynamical behavior of disks on a vibrated surface for different peak accelerations G and driving frequencies f. The different kinds of dynamical behavior are explained in table 2.3.

The data shows that for high frequencies the disks move steadily but get stuck soon (state **2**), while for low frequencies the disks move around wildly (state **4**,**5**), which leads effectively to 3D dynamics instead of the desired 2D dynamics.

This dynamical behavior of the disks is plotted versus the peak acceleration G and the theoretical jump height h_M for the inelastic case (c.f. equation (2.19)) in figure 2.8. h_M is the maximum distance from the surface which the disks could reach if they would collide with the surface completely inelasticly. However, the disks collide partly elastic and can therefore accumulate energy over several jump cycles. This means, that the jump height can be larger than h_M. Also, the disks can be tilted during the time when they do not touch the surface. If a tilted disk collides with the surface, it experiences a combination of a torque and a repulsive force.

This torque tends to be higher for higher h_M, because a bigger jump height allows for a higher tilting angle. If the torque gets large enough, it might destabilze the disk and might even cause it to flip around (state **4** and **5**). This is consistent with figure 2.8, which shows that state **4** and **5** always occur at high h_M. On the other hand, if h_M is very small, this means that

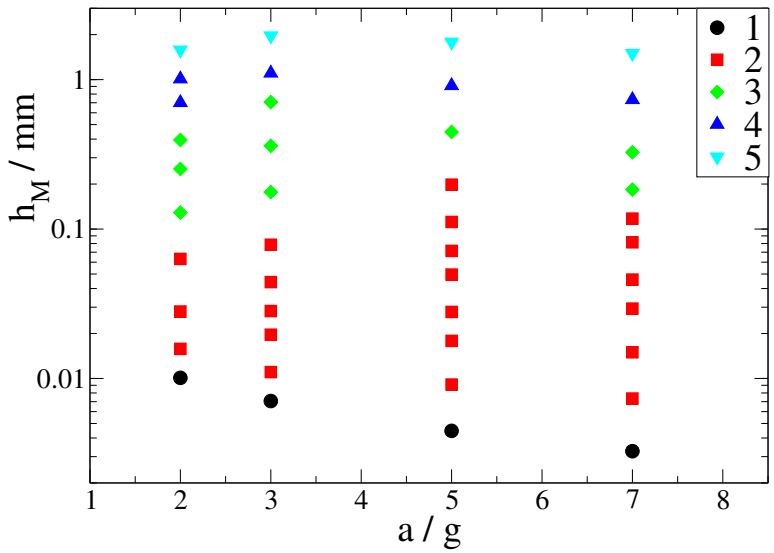

Figure 2.8: Dynamical behavior of disks on a vibrated surface for different peak accelerations G and theoretical particle jump height h_M. The theoretical jump height is calculated from the vibration parameters, assuming a point-shaped and inelastic particle (cf. section 2.2.1). Therefore, the actual jump height for different points at the disks will in general deviate significantly from the calculated h_M.

the disks only leave the surface for a rather short time. Also, they can only experience a very small torque. Therefore, in this case the disks can only move by a small distance between two collisions. This makes it very likely that they get stuck in some locally stable position, e.g. caused by a small unevenness of the surface. This is also consistent with the fact that in figure 2.8 the static state **1** only occurs at very low h_M.

Also, at least some small tilting seems to be a neccessary condition for a disk to start moving. Because of this, disks which touch the walls or neighboring disks often stop moving: A neighboring disk (especially if it does not move itself) or a wall provides a vertical plane, which can restrict the tilting possibilities of the disk and by this eventually also stop its horizontal movement. Especially for lower h_M, this often leads to the formation of groups of adjacent disks, which are not able to move any further anymore.

In summary, one can conclude that the complexity of the dynamics of disks on a vibrating surface causes a significant likelihood for a disk not to move even for quite high h_M. This likelihood becomes smaller for higher h_M and eventually all disks start moving (state **5**). But at the same time a higher h_M increases the likelihood of strong tilting, flipping around and overlapping of disks, which effectively produces a 3D-system instead of a 2D-system. In the described experiments no set of parameters (G, f) could be found which allows for a continous movement of all particles and prevents 3D-dynamics at the same time. In addition, the analysis of those experimental results suggests that there are no such parameter sets at all. This might also be the reason for the fact, that no 2D granular experiments using disks on a vibrated surface can be found in literature.

2.4.2 Disks with Top Plate

A possible solution for the problem of excessive tilting of driven disks could be the introduction of a top plate into the system, which would constrain the disks effectively to two dimensions. Such a setup is tried by using a plexiglass plate as top plate for a $200 \times 200\text{mm}^2$ experimental area. This means, the disks are confined in a box which consists of the vibrating surface as bottom plate, metal bars as horizontal boundaries and the plexiglass plate as top plate. Different heights of this box between 2.5mm and 5mm are tried. The whole system is vibrated with different parameter sets which allow all disks to move, or in other words, which leads to a state-5 disk movement according to figures 4.32 and 2.8.

However, when vibrated that strongly, the plexiglass plate also starts to vibrate significantly. This cannot be easily prevented, because it could only be stabilized by either introducing supporting columns into the experimental area or by using a very thick plate. But introducing supporting columns would change the bulk dynamics of the system and using a very thick plate would lead to an undesirable high total mass of the experiment, especially, when the experimental area is eventually extended to $500 \times 500\text{mm}^2$. Also, the choice of possible top plate materials is quite limited, because it has to be transparent in order to allow a direct observation of the system.

A vibrating top plate allows the system height to change temporarely

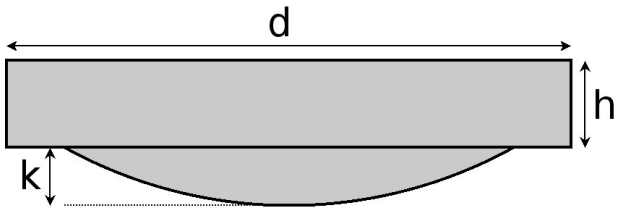

Figure 2.9: Large particle A with spherical cap. The spherical cap has a height of k = 2mm and a curvature radius of 17mm. A cylinder with height h = 3mm and diameter d = 20mm is placed at the top of the spherical cap.

and locally. For instance, even if the system height is set to 2.5mm, the height can temporarly exceed 4mm at some places. This allows some disks to slip above each other, which can be frequently observed in such setups. This means that introducing a top plate does not prevent the disks from performing 3D-dynamics.

Therefore, driving disks by vertical shaking in a controlled way seems to be rather difficult. Consequently, it makes sense to look for alternative particle shapes, which should allow for a disk-like 2D collision behavior and for a controlled driving by vertical shaking at the same time.

Also, an experiment with open top is more suitable for possible future extensions. For instance, it might be interesting to investigate the dynamics of a sample particle, which is pulled through a dense granular fluid by a constant force [11, 12, 13].

2.4.3 Disks with Spherical Cap

The main difficulty of driving cylindrical particles in a horizontal direction is due to the fact, that the whole particle touches the vibrating table surface. This leads to geometrical constraints of the possible particle movement. Those restrictions can hinder or even effectively block the transformation of the vertical vibrations into a horizontal motion. On the other hand, spherical particles touch the vibrating table surface only at one point and do not experience any geometrical constraints due to their shape. Consequently, spheres can be driven very well by vertical vibrations.

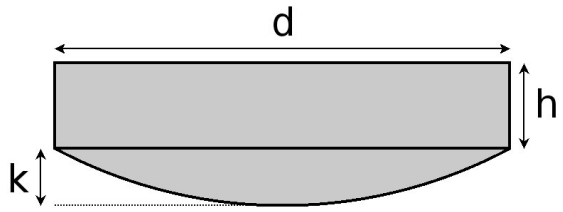

Figure 2.10: Small particle B with spherical cap. The spherical cap has a height of k = 2mm and a curvature radius of 17mm. A cylinder with height h = 3mm and diameter d = 16mm is placed at the top of the spherical cap.

Therefore, it makes sense to design particles, which consist of a cylindrical part combined with a spherical cap (cf. fig. 2.9, fig. 2.10). While the cylindrical part ensures a disk-like particle-particle collision behavior, a spherical cap at the lower side of the cylinder allows for a good transformation of vertical driving into horizontal motion.

In order to produce a bidisperse mixture, two different kinds of particles are designed: The cylindrical part of the large particles A has a height of 3mm and a diameter of 20mm (cf. fig. 2.9). The cylindrical part of the small particles B has a height of 3mm and a diameter of 16mm (cf. fig. 2.10). The curvature radius of the spherical cap is chosen as 17mm both for A- and B-particles. This ensures, that the coupling of both kinds of particles to the vibrating surface is as similiar as possible. Also, the height of the spherical cap (2mm) is the same for both kinds of particles in order to achieve an equal height of A- and B-particles.

The particles are produced from an ABS filament by a 3D printer (Makerbot). This 3D printer allows for a spatial resolution of about $\approx$ 0.3mm.

The height of the center of mass can be determined as c_A = 3.52mm for large particles and c_B = 3.32mm for small particles. This is much smaller than the curvature radius of the spherical cap of 17mm. Hence, if the particle is tilted in one direction, it experiences a torque opposite to the tilting direction. This means, that if tilted, the particle automatically goes back into an upright position. On the one hand such a particle is able to pick up horizontal velocities due to the spherical shape of its lower surface, but on the other hand its ability to maintain an upright position ensures a disk-like particle-particle collision behavior.

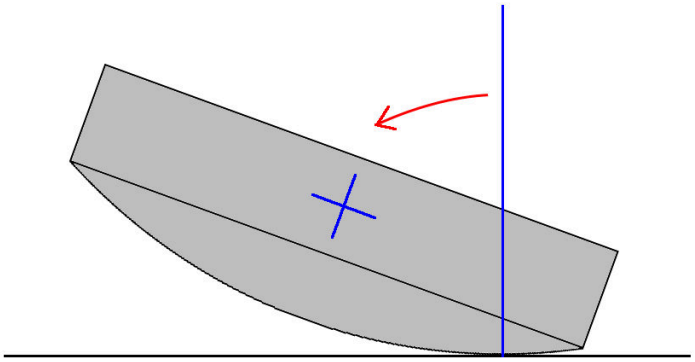

Figure 2.11: A tilted cylinder with spherical cap experiences a torque (red arrow) opposite to the tilting direction. The torque is caused by the fact, that the x-y-position of the center of mass (blue cross) deviates from the position of the contact point between spherical cap and surface.

However, if the particles are driven too strongly, they can flip around or slip above each other. This would destroy the disk-like dynamics and effectively produce a 3D system. Therefore, a too strong agitation of the particles has to be avoided. Because the dynamics of disk-shaped particles with spherical caps are quite complex, suitable parameters of the vertical driving have to be determined experimentally: A suitable baseplate oscillation on the one hand has to be strong enough to produce a random horizontal movement of particles, but one the other hand has to be weak enough to avoid particle flipping and 3D particle dynamics.

It turns out, that a sine-shaped oscillation with a frequency of $f = 120\text{Hz}$ and a peak acceleration of $a = 3\text{g}$ leads to optimal particle dynamics. The amplitude A of this oscillation amounts to $A = \frac{a}{\omega^2} \approx 52\mu\text{m}$.

Chapter 3

Lorentz Model

3.1 Setup

A Lorentz system is realized by a $400 \times 300\text{mm}^2$ epoxi plate (cf. fig. 3.1 and 3.2). The actual area of the system is $A = 350x240\text{mm}^2$, contained by styrofoam boundaries. Within this area, there are $N = 1600$ randomly distributed needles, which act as obstacles. The positions of the needles are calculated by a computer program, which draws the x- and y-coordinates of the needle positions from uniform probability distributions.

The dynamics of a sample particle in this Lorentz system has to be measured for different obstacle densities $n^* = \frac{r_{ob}^2 N}{A}$. This could be achieved by changing the obstacle radius r_{ob} between measurements, which would effectively mean that a new epoxi plate has to be produced. However, a collision of a sphere of diameter r_s with a point-shaped obstacle is geometrically identical to a collision of a point-shaped particle with an obstacle of radius r_{ob}. Because of this, instead of building different systems with different obstacle radii, in this experiment different spheres with different radii are used as sample particles. Since the needle radii are smaller than 0.5mm, while the spheres have radii between 2.9mm and 6.95mm, the obstacles can be considered as approximately point-shaped.

The epoxi plate is attached to a vibrating table, which is driven by a sine oscillation with a peak acceleration $a = 7g$ and a frequency $f = 156\text{Hz}$. This leads to an oscillation amplitude of $A = \frac{a}{\omega^2} \approx 0.092\text{mm}$. Polyester resin spheres with diameters $d = 5.8\text{mm}$, $d = 8\text{mm}$, $d = 10\text{mm}$, $d = 11.5\text{mm}$ and $d = 13.9\text{mm}$ are used as sample particles. Those spheres can move

Figure 3.1: The Lorentz system experiment. The experiment is put on a LDS V721 vibrating table, which produces vertical oscillations. A sphere is driven by those oscillations and moves through a random network of obstacles, which are represented by needles.

randomly through the system with the specified driving parameters. A detailed analysis of the microscopic dynamics of those particles is provided in section 2.3.

An example of a trajectory of a $d = 8$mm-sphere on a vibrating surface is shown in figure 3.3. It can be seen, that the particle samples a fractal pocket of the obstacle network.

The dynamics of the sample particle differ from the dynamics of an elastic Lorentz model:

- The collisions between particles and needles are inelastic.
- The particle does not only change its direction and velocities during collisions with the obstacles, but also every time it hits the baseplate of the experiment. For the applied vibration parameters, this happens with a collision frequency in the order of 20Hz. Also, the collision frequency with the surface can vary greatly, depending on the current kinetic energy of the particle (cf. sect. 2.3). This means that the horizontal particle movement between obstacles can not be

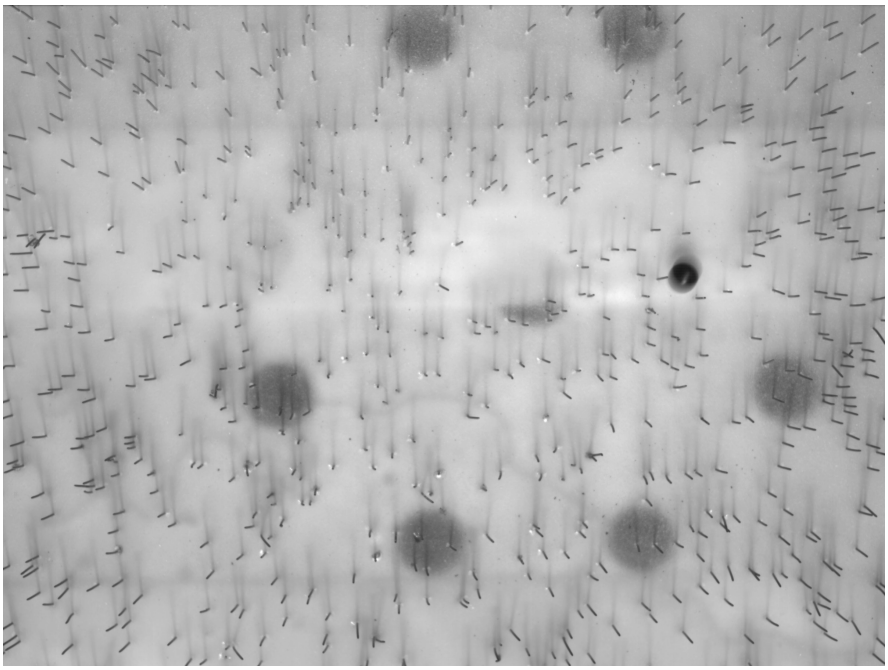

Figure 3.2: View from above of the Lorentz system. The black sphere (d = 8mm) moving through the obstacle network is the sample particle. The feint black circles are caused by the attachement of the expoxi plate to the headexpander.

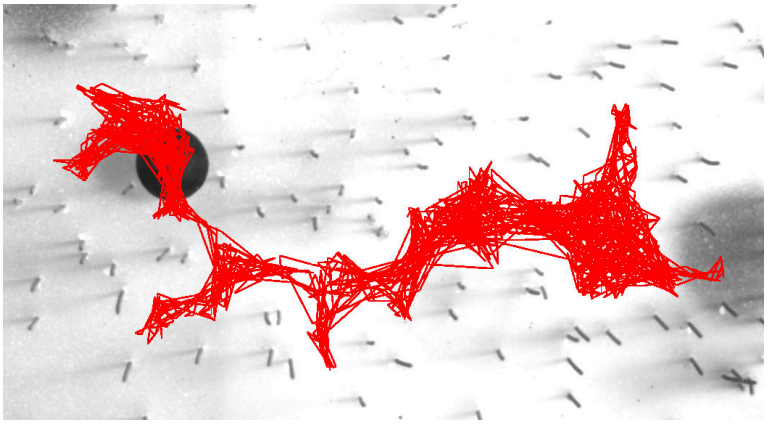

Figure 3.3: Trajectory of a sphere with $d = 8$mm within the Lorentz system experiment during a measurement time of ~ 300s. The sphere is driven by an vertical oscillation with frequency $f = 156$Hz and peak acceleration $a = 7g$.

considered purely Newtonian, but is probably rather a mixture of Newtonian and Brownian behavior.

- The particle velocity depends on a balance between driving and dissipation. Since the intensity of dissipation depends on the local obstacle density, the particle velocity might also depend on the geometry of the experiment. For instance, the particle might move faster on average within larger pockets of the obstacle network.

Because of those differences, it is interesting to compare simulation results of frictionless Lorentz models with experimental results from a granular Lorentz model. For instance, this might allow to draw conclusions on how much the long-time dynamics of particles within a Lorentz model depend on microscopic dynamics.

3.2 Experiment

For each run, a polyester resin sphere is put at a random position of the Lorentz system plate, before the vibrating table is switched on. This starting position is determined by a random number generator in order to avoid any bias by the experimenter. If this position is blocked by needles, another possible position is calculated until the sphere can be placed.

Once the sphere is placed, the vibrating table is switched on and a vibration with $a = 7g$ and $f = 156$Hz is started. The sphere is filmed by a high speed camera, which is able to produce videos with frame rates between 4.68fps and 480fps at full resolution ($2400x1800\text{px}^2$). If the resolution is decreased, the frame rate can be increased beyond 480fps. From the resulting video, the trajectory of the sphere can be determined by the image processing algorithm. This algorithm is written in c++ and uses following steps to determine the position of the sphere from a greylevel image $I(x, y)$ of the experiment:

1. A smoothed image $J(x, y)$ is calculated from the original image $I(x, y)$. The smoothing filter is defined as follows:

$$J(x, y) = \frac{1}{(2n+1)^2} \sum_{k=x-n}^{x+n} \sum_{l=y-n}^{y+n} I(k, l) \tag{3.1}$$

   The smoothing is effectively a low-pass filter, which can be tuned by the parameter n. It is used to retrieve the background intensity of the image.

2. A local treshold $T(x, y)$ is calculated by dividing the original image $I(x, y)$ by the background intensity $J(x, y)$ and multiplying with a factor f:

$$T(x, y) = \frac{fI(x, y)}{J(x, y)} \tag{3.2}$$

3. A binarized image $B(x, y)$ is produced by applying the local threshold $T(x, y)$ to the original image $I(x, y)$:

$$B(x, y) = \begin{cases} 1, & \text{if } I(x, y) > T(x, y) \\ 0, & \text{else} \end{cases} \tag{3.3}$$

4. Because a black sphere is used, now the sphere should be represented in $B(x, y)$ by pixels with the value 0, while all other pixels have value 1. Therefore, the position (x_s, y_s) of the sphere can be calculated as an average over the positions of all pixels with value 0. In order to avoid wrong results, the algorithm also checks if all 0-pixels form a connected area. If not, no particle position is returned.

The algorithm is optimized by changing the parameters n and f until the particle position can be recognized correctly. The optimal set of parameters

diameter	4.68fps	480fps	6400fps
5.8mm	40	9	13
8mm	14	12	9
10mm	11	0	0
11.5mm	6	14	4
13.9mm	10	4	6

Table 3.1: Number of runs of measurements for different sphere diameters and frame rates of the Lorentz model.

depends on the position and strength of light sources and on the exposure time. However, $n = 200$px and $f = 0.91$ work for most image series.

After the particle position is known for every frame, the mean-squared displacement $M(t) := \delta r^2(t)$ of the particle trajectory can be calculated. For large times t, $M(t)$ depends very much on the starting point and the actual path of the particle. For instance, if a particle is too large to explore the whole system, it is confined within a subarea of the system during the whole measurement. In this case, the size of this subarea which contains the starting position has a big impact on $M(t)$. However, even if the particle is small enough to move through the whole system, this might still take longer than the duration of the measurement. This means, that the particle stays within a subarea during the whole measurement even though it is in priniciple able to leave that area. Therefore, while the impact of the starting position is most significant for large particles, it does also exist for smaller particles.

In order to obtain a representative $M(t)$, multiple measurements are performed for each sphere diameter and the mean-squared displacements of individual measurements are averaged. Also, the frame rate of the camera is varied in order to capture the dynamics of the sample particles for both very small and rather large times. In particular, for most particle sizes measurements with frame rates of 4.68fps, 480fps and 6400fps are performed. Table 3.1 shows the exact number of measurement runs for each particle size.

The mean-squared displacements $M(t)$ are averaged for each frame rate seperately and than put together in a joint plot.

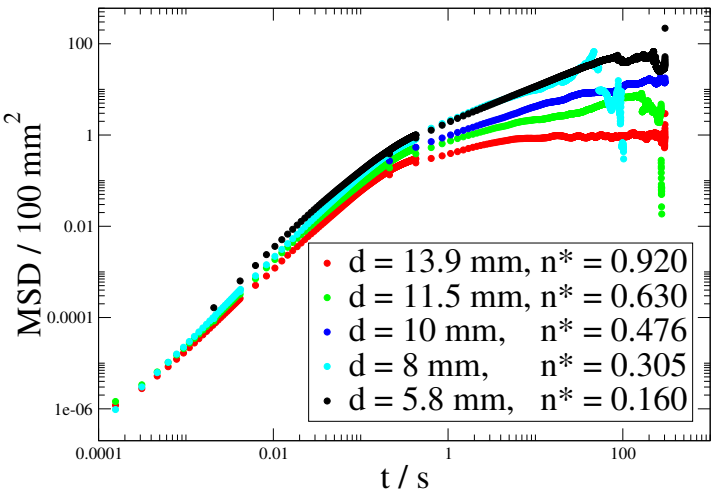

Figure 3.4: Mean-squared displacements of different spheres in the Lorentz system

3.3 Results

The results of the Lorentz system experiment are shown in figure 3.4. The average mean-squared displacement for different frame rates (4.68fps, 480fps and 6400fps) match each other quite well, which allows to plot smooth mean-squared displacement curves from $t \approx 156\mu$s to $t \approx 304$s. This means, that the measurements cover more than six decades in time.

For small times, all mean-squared displacements $M(t)$ are approximately proportional to t^2, which means that for small times the particles mainly move ballistically and accelerations due to collisions or friction are negligible. The distance Δx_i covered by a particle during a time t can therefore be expressed as

$$\Delta x = vt \tag{3.4}$$

The behavior of the resulting mean-squared displacement $M(t)$ can be explained by squaring this expression and averaging over a large number of observations:

$$M(t) =< \Delta x^2 >=< v^2 t^2 >=< v^2 > t^2 \tag{3.5}$$

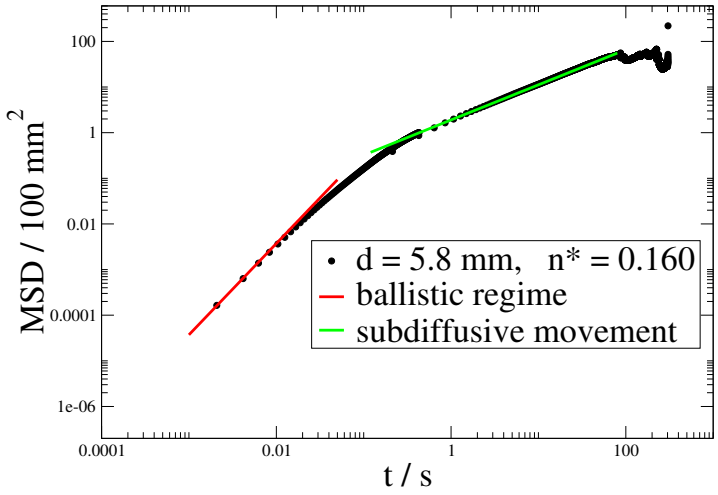

Figure 3.5: Manual fit of ballistic movement and subdiffusive dynamics to the mean-squared displacement for the density $n^* = 0.160$. The fit of the ballistic regime at short times gives a velocity of $\sqrt{< v^2 >} \approx 25 \frac{\text{mm}}{\text{s}}$ and the fit of the long-time regime yields an exponent of $\beta \approx 0.77$.

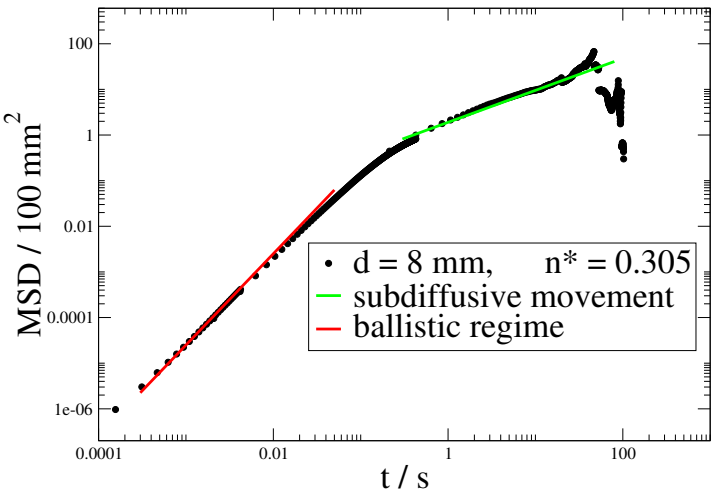

Figure 3.6: Manual fit of ballistic movement and subdiffusive dynamics to the mean-squared displacement for the density $n^* = 0.305$. The fit of the ballistic regime at short times gives a velocity of $\sqrt{< v^2 >} \approx 22 \frac{\text{mm}}{\text{s}}$ and the fit of the long-time regime yields an exponent of $\beta \approx 0.7$.

With this equation, the mean-squared velocities of particles can be obtained directly from the measured $M(t)$.

For longer times, the exponent of the mean-squared displacements decreases below 1. The exact value of this exponent depends on the particle diameter. For even longer times, one would either expect a transition to diffusive dynamics or to localized dynamics, depending on if the system is below or above the critical density n_c^* [8][9]. This means, the exponent should either approach 1 or drop to 0. However, for most sphere diameters the time of measurement is too short to observe the long-time limes of the exponent. Only for $d = 13.9$mm an eventual decrease of the exponent to 0, which indicates localized dynamics, can be observed.

For the $d = 5.8$mm-sphere and the $d = 8$mm-sphere, the mean-squared displacement reaches values in the order of 10^4mm^2 at the large-time side of figure 3.4. Because the system size is 350×240mm^2, a mean-squared displacement of 10^4mm^2, which amounts to mean displacements in the

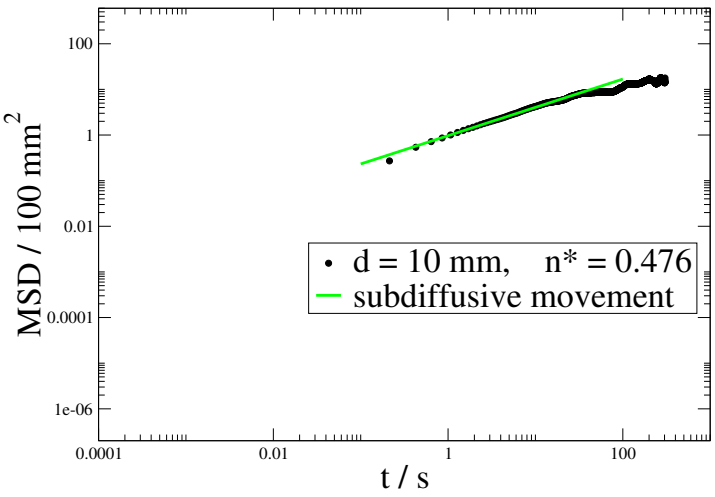

Figure 3.7: Manual fit of subdiffusive dynamics to the mean-squared displacement for the density $n^* = 0.476$. The fit of the long-time regime yields an exponent of $\beta \approx 0.62$.

order of 10^2mm, is already comparably large. Therefore, trying to measure larger mean-squared displacements would lead to significant finite size effects.

For further evaluation of the measured data, first the effective densities of the Lorentz system for different sphere diameters have to be determined. The effective density n^* is given as:

$$n^* = \frac{r_{ob}^2 N}{A} = \frac{d_{ob}^2 N}{4A} \tag{3.6}$$

r_{ob} and d_{ob} are the radius and the diameter of the obstacles. Because the actual diameter of a needle is small compared to the particle diameter, the effective obstacle diameter d_{ob} approximately equals the sphere diameter. $N = 1600$ is the number of obstacles and $A = 84000\text{mm}^2$ is the total area of the experiment. The resulting densities n^* for different sphere diameters are listed in table 3.2.

Now the mean-squared particle velocities are determined for different densities by a manual fit of equation (3.5) to the short-time regime of the

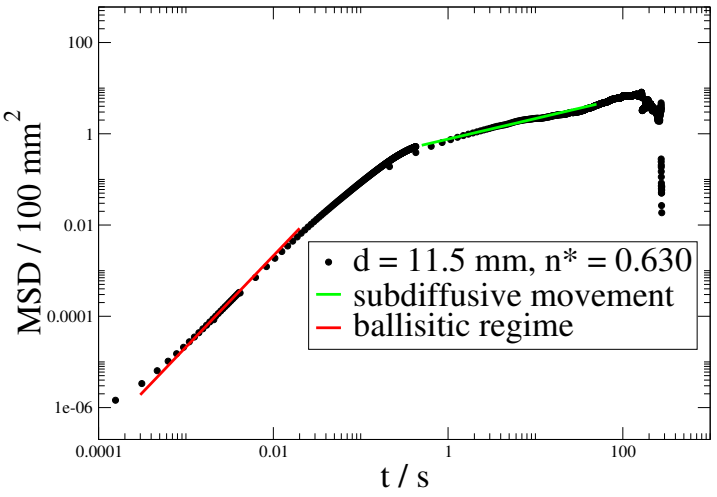

Figure 3.8: Manual fit of ballistic movement and subdiffusive dynamics to the mean-squared displacement for the density $n^* = 0.630$. The fit of the ballistic regime at short times gives a velocity of $\sqrt{< v^2 >} \approx 21 \frac{\text{mm}}{\text{s}}$ and the fit of the long-time regime yields an exponent of $\beta \approx 0.45$.

sphere diameter in mm	5.8	8	10	11.5	13.9
n^*	0.160	0.305	0.476	0.630	0.920

Table 3.2: Densities of the Lorentz model for different diameters of the sample sphere.

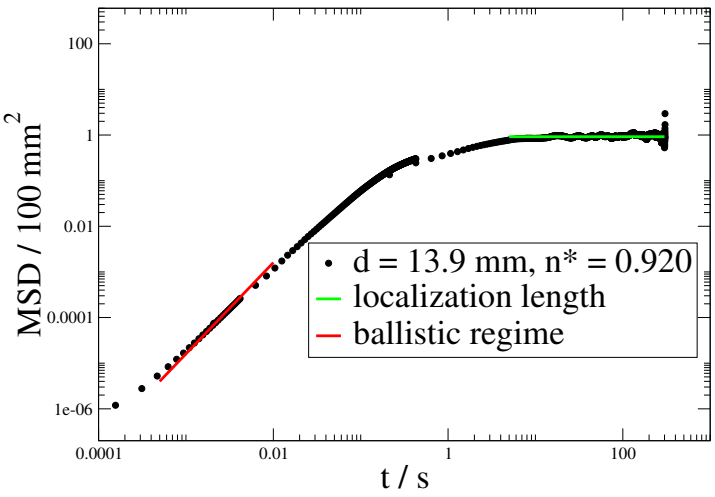

Figure 3.9: Manual fit of ballistic movement and localization length to the mean-squared displacement for the density $n^* = 0.920$. The fit of the ballistic regime at short times gives a velocity of $\sqrt{< v^2 >} \approx 20 \frac{\text{mm}}{\text{s}}$. In the long-time regime, the particle is arrested and the exponent is $\beta = 0$.

measured mean-squared displacements. Similiarly, the function

$$M(t) = at^{\beta} \tag{3.7}$$

is fitted manually to the long-time regime of the measured mean-squared displacements in order to obtain the prefactor a and the exponent β. Those fits are shown in figure 3.5, 3.6, 3.7, 3.8 and 3.9.

The resulting mean squared velocities $< v^2 >$ for the ballistic motion and the parameters a and β of the subdiffusive motion are listed in table 3.3.

It turns out that the mean-squared velocities $< v^2 >$ decrease with increasing density n^*. The driving mechanism should only depend on the vibrating table oscillation and on the coefficient of restitution ϵ of the particles, but not on the mass and size of the particle. Therefore, the decrease of the mean-squared velocity is most likely not caused by differences in the driving itself. However, the mean free horizontal path of a particle is much smaller at higher densities. Therefore, the horizontal velocity has less time to add up until the particle collides with an obstacle and by this

n^*	$\sqrt{< v^2 >}[\frac{\text{mm}}{\text{s}}]$	$a[\text{mm}^2]$	β
0.160	25	230	0.77
0.305	22	250	0.7
0.476	-	95	0.62
0.630	21	55	0.45
0.920	20	92	0

Table 3.3: Short time velocities and parameters of a function at^β fitted to the long-time regime of the measured mean-squared displacements.

loses a part of its horizontal velocity. This mechanism might explain the differences in the microscopic dynamics.

The exponent β does also decrease with increasing density. For $n^* = 0.920$ it becomes zero, which means that the particle becomes localized. Molecular dynamics simulations predict a critical density of $n_c^* \approx 0.359$ for a 2D Lorentz model [9]. Different from those simulation results, for $n^* = 0.476$ and $n^* = 0.630$ non-zero exponents β are measured. However, the system used in this experiment is to small to determine if the particle finally localizes or not at densities of $n^* = 0.476$ and $n^* = 0.630$. Also, the distribution of the 1600 obstacles is fixed for all measurements. This means, that the obstacle distribution used in the experiment might not be statistically representative for a 2D Lorentz model and therefore exhibit different properties. In order to check this, either additional measurements with different obstacle distributions or a larger system is needed.

Another result from simulation is that the exponent β just at n_c^* is

$$\beta(n_c^*) = \frac{2}{3.03} = 0.66 \tag{3.8}$$

This is consistent with the measured data, which shows an exponent $\beta \approx 0.7$ at the density $n^* = 0.305$. The measured β are also shown in figure 3.10.

3.4 Conclusion

A 2D Lorentz model is realized experimentally. A random particle movement is achieved by vibrating the system vertically. The obtained mean-squared displacements show a localization transition and subdiffusive dynamics consitent to simulation results.

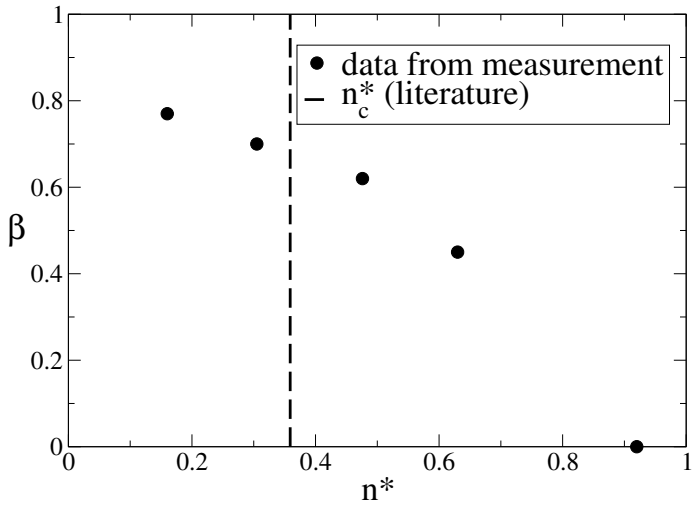

Figure 3.10: Measured exponents β as a function of the density n^*. The dashed vertical line shows a molecular dynamics prediction for the critical density n_c^* [9].

However, for more detailed measurements a larger system size and sampling over several obstacle configurations is required.

Chapter 4

Glass Transition in a Dense Granular Fluid

4.1 Setup

A dense granular fluid in two dimensions is represented by cylinders with spherical caps on a vibrating surface (cf. fig 4.1). The particles used are described in detail in section 2.4.3. In the experiment, a bidisperse mixture consisting of 50% large particles (A) with a diameter $d_A = 20$mm and 50% small particles with a diameter of $d_B = 16$mm, is used. The particles are confined within a circular area with a diameter of 380mm. The baseplate of this area is driven by an LDS vibrating table, which produces a vertical sine oscillation with a frequency of $f = 120$Hz and a peak acceleration of $a = 3$g.

A camera is mounted above the experiment. This allows to continously take pictures of the sample, which then can be evaluated by image processing programs in order to track the movement of the sample particles.

4.2 Image Processing

For measuring quantities like e.g. the mean-squared displacement, it is crucial to be able to track individual particles over long times. This can be either done by tracking the particles from frame to frame within a video, or by recognizing individual particles within images.

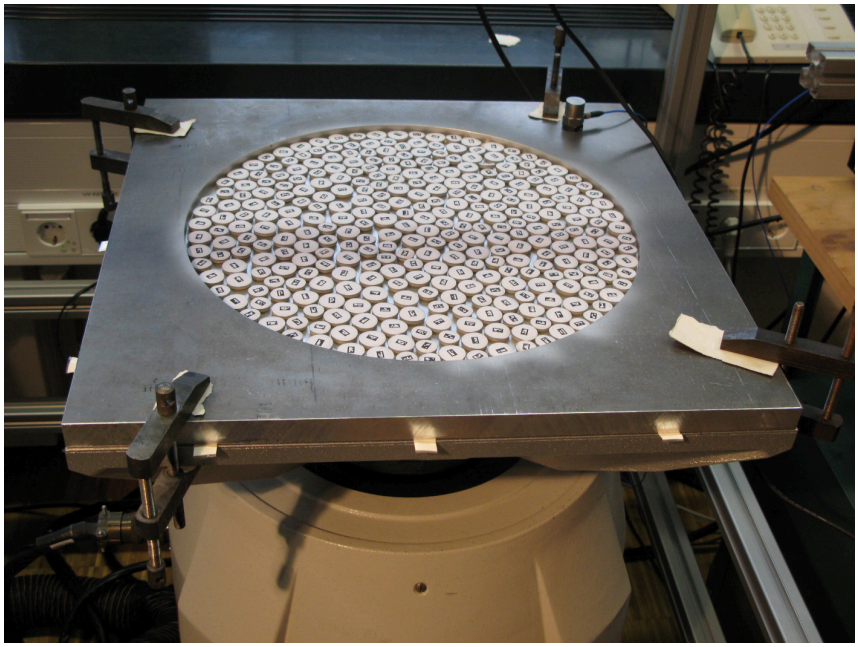

Figure 4.1: Experimental setup for the dense granular fluid experiment. The particles are contained in a circular area and vertically vibrated by a LDS V721 shaker.

4.2.1 Particle Tracking on a Frame-to-Frame Basis

In order to track particles from frame to frame, first the particle positions have to be evaluated for every frame. Then the found particle positions in subsequent frames are compared. If two particle positions in two subsequent frames differ by less than a particle radius, they are considered as two subsequent observations of the same particle. By matching particle positions between subsequent frames, it is possible to track individual particles over the whole time of an experiment[1].

However, the success of such a tracking algorithm depends on two conditions:

- The frame rate has to be high enough to guarantee, that no particle can move by more than one particle radius between frames. If the long time dynamics of particles have to be measured, this leads to an extremely high number of images which has to be recorded and analysed.

[1] A detailed description of an image processing algorithm which tracks particles on a frame-to-frame basis is given in section 5.2

- If the position of a particle can not be determined within a certain frame, the tracking of this particle gets interrupted and can not be continued, because in later frames the particle can not be identified again. Even worse, if a particle is falsely found at a wrong position in one frame, this can cause the image processing algorithm to swap two particles which each other, which might e.g. artificially increase the measured mean-squared displacement. This means, the tracking algorithm depends very much on the accuracy of the image processing algorithm which determines the particle positions. In addition, the impact of image processing errors becomes increasingly large, when the measurement time and therefore the total number of frames is increased.

Because long time measurements are particularely interesting for analysing glassy dynamics, especially the second point is critical for the accuracy of such a particle tracking algorithm for the described experiment. The impact of image processing errors on the measured mean-squared displacement of a 2D-system can be estimated as follows:

Assume a system with N particles, which are tracked by an image processing algorithm. This algorithm has a probability $p > 0$ to confuse a given particle with its neighbor at a given frame. Consequently, after t frames, $(1-(1-p)^t)N$ particles have been confused with neighboring particles at least once.

If a particle i is swaped with its neighbor j at a time t_1, this has two effects: First, the displacement $\vec{D}_i(t)$ of the particle after t frames is replaced by the sum of two seperate displacements $\vec{D}_i(t_1)$ and $\vec{D}_j(t-t_1-1)$ of the particles i and j after t_1 and $t-t_1-1$ frames, respectively. In addition, a displacement $\vec{d}$ is added, because if two particles are swaped, this appears like one particle moving by its own diameter. Consequently, the absolute value of the vector $\vec{d}$ equals one particle diameter. Now, the measured displacement $\vec{D}'_{i,j}(t)$ of the apparent particle trajectory can be written as:

$$\vec{D}'_{i,j}(t) = \vec{D}_i(t_1) + \vec{d} + \vec{D}_j(t-t_1-1) \tag{4.1}$$

If we now assume, that we average over a large number of trajectories of particles, which all are swaped with a neighboring particle at the time t_1, we can write:

$$< \vec{D}'(t)^2 > = < (\vec{D}(t_1) + \vec{d} + \vec{D}(t-t_1-1))^2 > \tag{4.2}$$

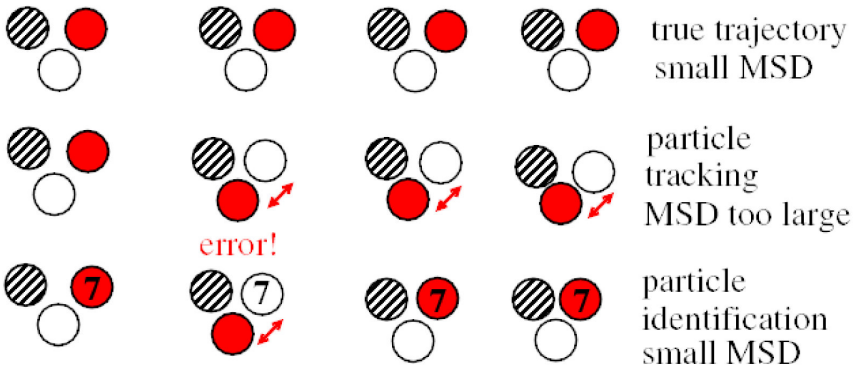

Figure 4.2: If particles are swaped by a tracking algorithm on frame-to frame basis, the apparent mean-squared displacement (center) can increase significantly faster at longer times than the actual mean-squared displacement (top). A potential solution for this problem is to label individual particles (bottom).

This leads to:

$$\begin{aligned} < \vec{D}'(t)^2 > =& < \vec{D}(t_1)^2 > + < \vec{d}^2 > + < \vec{D}(t - t_1 - 1)^2 > + 2 < \vec{D}(t_1)\vec{d} > \\ &+ 2 < \vec{D}(t - t_1 - 1)\vec{d} > + 2 < \vec{D}(t_1)\vec{D}(t - t_1 - 1) > \end{aligned} \tag{4.3}$$

The terms $< \vec{D}(t_1)^2 >$ and $< \vec{D}(t - t_1 - 1)^2 >$ equal the actual mean-squared displacements $M(t_1)$ and $M(t - t_1 - 1)$ of the system. The term $< \vec{d}^2 >$ by definition equals the squared particle diameter d^2. Because the direction of $\vec{d}$ depends on the image processing algorithm only, it is to a good approximation not correlated with the actual particle displacements. Therefore, the terms $< \vec{D}(t_1)\vec{d} >$ and $< \vec{D}(t - t_1 - 1)\vec{d} >$ equal zero. $< \vec{D}(t_1)\vec{D}(t - t_1 - 1) >$ correlates the subsequent displacements of two *different* particles. This term approaches zero for dilute systems, but can have a non-zero value for sufficiently dense systems. However, for simplicity, it is set to zero in this calculation. Then one can write:

$$< \vec{D}'(t)^2 > \approx M(t_1) + M(t - t_1 - 1) + d^2 \tag{4.4}$$

The impact of the image processing errors on different kind of systems can be estimated:

- If the particles move ballistically, the mean-squared displacement is proportional to t^2 and therefore

$$M(t) \gg M(t_1) + M(t - t_1 - 1) \tag{4.5}$$

This means, that for such a system the measured $< \vec{D'}(t)^2 >$ is significantly smaller than the actual mean-squared displacement $M(t)$.

- If the particles move diffusively, the mean-squared displacement is proportional to t and therefore

$$M(t) \approx M(t_1) + M(t - t_1 - 1) \tag{4.6}$$

This means, that for diffusive dynamics, the measured $< \vec{D'}(t)^2 >$ does is a good approximation of the actual mean-squared displacement $M(t)$. However, this is only valid as long as $M(t) \gg d^2$ is true.

- If the particles move subdiffusively, one can write

$$M(t) \ll M(t_1) + M(t - t_1 - 1) \tag{4.7}$$

In this case, the measured $< \vec{D'}(t)^2 >$ is significantly larger than the actual mean-squared displacement $M(t)$.

Still, a particle might be swaped with its neighbors more often then once. In that case, the term $< \vec{d^2} >$ has to be replaced by the term $< \vec{d_S}^2 >$, while $\vec{d_S} = \sum_{k=1}^{n} \vec{d_k}$ is the sum of n apparent displacements by one particle diameter each. Because those displacements are uncorrelated with each other, one can write:

$$< \vec{d_S}^2 >= nd^2 \tag{4.8}$$

If one now considers the case, that the particles are at rest, the measured mean-squared displacement $M'(t)$ can be calculated as follows:

$$M'(t) = \sum_{l=0}^{t-1} \binom{t-1}{l} \binom{t-1}{t-l-1} p^l (1-p)^{t-l-1} l d^2 \tag{4.9}$$

$\sum_{l=0}^{t-1} \binom{t-1}{l} \binom{t-1}{t-l-1} p^l (1-p)^{t-l-1} l$ is the expectation value of a binomial distribution, which is $(t-1)p$. Therefore, one gets a apparent mean-squared displacement of

$$M'(t) = (t-1)pd^2 \approx tpd^2 \tag{4.10}$$

One can conclude:

1. For a system at rest ($M(t) = 0$), the impact of image processing errors can be calculated from the error probability p as: $M'(t) - M(t) \approx tpd$. Hence, for $p > 0$, a system at rest will always appear as a diffusive system. Even for a small error probability of $p = 0.001$, according to equation (4.10), this leads to an apparent movement by one particle diameter after 1000 frames.

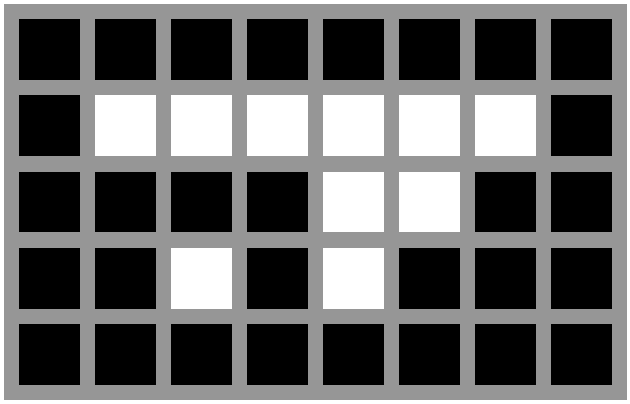

Figure 4.3: Sketch of a particle label. The particle has the number 131, which leads to a binary code of $131 * 7 = [00001110010101]_2$.

2. For a moving system ($M(t) \neq 0$), it is difficult to calculate the effect of tracking errors exactly. However, the image processing errors drag the measured mean-squared displacements $M'(t)$ towards the diffusive case $M'(t) \sim t$ (cf. fig. 4.2).

3. Because the effect of tracking errors increases with the considered time t, it becomes particularely difficult to properly recognize localized mean-squared displacements, because the tracking errors always add a diffusive component to the actual mean-squared displacement.

However, for measuring glassy dynamics, it is interesting to look at localized or subdiffusive mean-squared displacements over long time scales, i.e. at large t. Thus, a particle tracking algorithm on a frame-to-frame basis is not suitable for measuring glassy dynamics, because it shows apparent hopping at long times.

4.2.2 Tracking of Labeled Particles

The main weakness of a tracking algorithm on a frame-to-frame basis is that the effect of image processing errors adds up over time: If such a tracking algorithm loses a particle trajectory, it can not find the particle again for the remaining time of the measurement, because it can not distinguish one particle from another. In order to avoid this problem, each particle has to be labeled by a unique code. Such a labeling system is developed as follows:

A unique number between 0 and 2340 is assigned to each particle. Numbers between 0 and 999 are assigned to large particles, while numbers between 1000 and 2340 are assigned to small particles. Those numbers are multiplied by seven and then turned into 14-digit binary numbers.

For instance, a big particle with number 131 gets the binary code:

$$131 * 7 = 917 = [00001110010101]_2 \tag{4.11}$$

In order to make this code machine readable, it is encoded into a binary image with 5×8 pixels. White pixels represent the digit 0, while black pixels represent the number 1. The 22 pixels at the boundary of the label are always set to 1 (black) in order to allow the image processing algorithm to determine the dimension and, by that, the resolution of the label. The two pixels in the upper corners of the inner area of the label are always set to 0 (white) and the two pixels in the lower corners are always set to 1 (black). This allows to determine the orientation of the label. The binary code with digits $d_{13}, ..., d_0$ is then written into the 14 remaining pixels.

1	**1**	**1**	**1**	**1**	**1**	**1**	**1**
1	**0**	d_{13}	d_{12}	d_{11}	d_{10}	**0**	**1**
1	d_9	d_8	d_7	d_6	d_5	d_4	**1**
1	**1**	d_3	d_2	d_1	d_0	**1**	**1**
1	**1**	**1**	**1**	**1**	**1**	**1**	**1**

Thereby, the digit d_{13} has the highest value (2^{13}) and the digit d_0 has the lowest value (2^0). For the particle with the number 131 and the binary code $[00001110010101]_2$, the label then looks as follows:

1	**1**	**1**	**1**	**1**	**1**	**1**	**1**
1	**0**	0	0	0	0	**0**	**1**
1	1	1	1	0	0	1	**1**
1	**1**	0	1	0	1	**1**	**1**
1	**1**	**1**	**1**	**1**	**1**	**1**	**1**

The label of this particle is sketched in figure 4.3. A picture of this particle within a 2D dense granular fluid can be seen in figure 4.4: The labels are put on the top surface of the particles in a way that the center of the label is identical with the center of the respective particle. Therefore the image processing algorithm only needs to locate the label in order to get the exact position of a particle. The particles are placed on a comparably bright surface, in order to provide a sufficient contrast between between label and

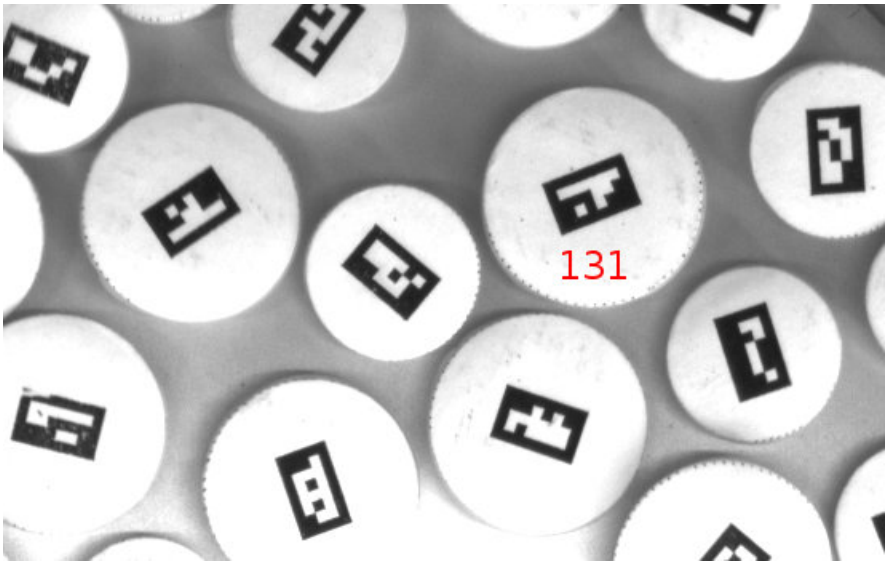

Figure 4.4: Labeled particles in a dense granular fluid on a vibrating table. The particle number 131 is marked by a red number.

background.

The image processing algorithm for finding the particle positions and reading the labels now works as follows:

1. An image $J(x, y)$ is calculated from the original greylevel image $I(x, y)$ by replacing each pixel with the average of the pixels within a $201 \times 201\text{px}^2$ square around the original pixel. This operation is effectively a low-pass filter and is used to determine the illumination of the sample.

2. A binarized image $B(x, y)$ is now created as

$$B(x, y) = \begin{cases} 1, & \text{if } I(x, y) < tJ(x, y) \\ 0, & \text{else} \end{cases} \tag{4.12}$$

   The threshold t is used to tune the resulting image in a way that, as far as possible, everything except the particle labels gets the value 0, while the particle labels get the value 1. The exact value of t depends on the analysed video. It is usually chosen from a range between $t = 0.5$ and $t = 0.65$.

3. Each connected area of pixels with value 1 is analysed seperately. First, areas which are too large or too small to represent a label are

excluded. The labels are represented by rectangles with a side ratio of $\frac{5}{8}$. Using this information, the image processing program measures the angle of rotation of the found labels. The labels are then extracted from the image and rotated into an upright position.

4. The resolution of the extracted labels is determined by measuring their exact dimension. With this information, the values of the 8×5 squares within the labels (cf. fig. 4.3) can be read by averaging the pixel values within each square and applying a threshold to the result.

5. It is checked if all boundary squares have the value 1 and if two corner squares of the inner region have the value 0 and the other two have the value 1. If not, the label is rejected because it may be unreadable.

6. The binary numbers $b = \sum_{i=0}^{13} 2^i d_i$ are extracted from the remaining labels and the positions of the labels are stored together with the numbers.

7. Finally, the resulting numbers b are devided by seven and it is checked if $l = \frac{b}{7}$ is an integer or not. If l is an integer, it is assumed that the particle with the number l has been found and its position is written to a data file. If l is not an integer, the particle is rejected. The numbers n_f and n_r of found and rejected particles are printed to a logfile to check the quality of the image processing algorithm:

   On average, one out of seven incorrectly read numbers can not be detected because they still happen to be multiples of seven[2]. This means, that the numbers of $\frac{n_r}{6}$ particles out of the n_f found particles have been read incorrectly. Therefore, the fraction p of image processing errors is given by

$$p = \frac{\frac{n_r}{6}}{n_f} = \frac{1}{6}\frac{n_r}{n_f} \tag{4.13}$$

   Because for all analysed videos, $\frac{n_r}{n_f}$ is found to be smaller than 0.2, an upper threshold for the particle recognition errors can be given by

$$p < 0.035 \tag{4.14}$$

[2]This can only happen if at least three digits of the binary number are read incorrectly, which is the reason to choose the number 7 as the divisor.

The errors of this image processing algorithm do also have an influence on the measured mean-squared displacement. However, different from a tracking algorithm on frame-to-frame basis, the impact of errors does not increase with time: If a particle is identified incorrectly in one frame, this does not prevent the algorithm from identifying it correctly again in later frames.

An upper threshold for the impact of image processing errors on the measured mean-squared displacement can be calculated as follows: Assuming a bidisperse mixture containing 50% large particles ($d_A = 20\text{mm}$) and 50% small particles ($d_B = 16\text{mm}$), a granular fluid with a density of $\varphi = 0.75$ in this experiment consists of

$$N = 2\frac{0.75\pi(190\text{mm})^2}{\pi((10\text{mm})^2 + (8\text{mm})^2)} \approx 330 \tag{4.15}$$

particles. The labeling system provides $\frac{2^{14}}{7} = 2340$ possible particle identification numbers. Therefore, if a particle is identified incorrectly, there is a probability of $\sim \frac{330}{2340}$, that this particle is swaped with one of the 330 existing particles. This means, that the fraction p_w of incorrectly measured particle positions is given by

$$p_w = p * \frac{330}{2340} \tag{4.16}$$

With $p < 0.035$, this yields:

$$p_w < 0.005 \tag{4.17}$$

The apparent mean-squared displacement $M'(t)$ of a system of N particles with a measurement time of T frames is now calculated as

$$M'(t) = \frac{1}{N(T-t)} \sum_{i=1}^{N} \sum_{\tau=1}^{T-t} (\vec{r}_i(\tau) - \vec{r}_i(\tau + t))^2 \tag{4.18}$$

If a fraction p_w of the positions $\vec{r}_i(t)$ is measured incorrectly, this means that also a fraction p_w of the summands $(\vec{r}_i(\tau) - \vec{r}_i(\tau + t))^2$ are incorrect. However, the remaining $(1 - p_w)N(T - t)$ summands are measured correctly and their average equals the actual mean-squared displacement $M(t)$. This means, that equation (4.18) can be rewritten as

$$M'(t) = (1-p_w)M(T) + p_w \frac{1}{2} \frac{1}{p_w N(T-t)} \sum_{i,\tau \in \text{incorrect}} ((\vec{r'}_i(\tau) - \vec{r}_i(\tau+t))^2 + (\vec{r'}_i(\tau) - \vec{r}_i(\tau-t))^2) \tag{4.19}$$

The second summand now contains the average squared distance between actual particle positions $\vec{r}$ and incorrectly identified particle positions $\vec{r'}$. Because the incorrect particle positions are randomly distributed and therefore uncorrelated to the actual particle posititions, a good estimate for an average squared distance is r_E^2, while r_E is the radius of the sample area. With this estimate, one can write:

$$M'(t) = (1 - p_w)M(t) + p_w r_E^2 \tag{4.20}$$

Because $p_w < 0.005$ is rather small, one can write

$$M'(t) \approx M(t) + p_w r_E^2 \tag{4.21}$$

This means that the mean-squared displacement is distorted by image processing errors by an added value $dM = p_w r_E^2$, which is given by

$$dM < 180.5\text{mm}^2 \tag{4.22}$$

The upper threshold for dM equals a mean-squared displacement caused by an average particle movement of about $\sqrt{180.5\text{mm}^2} \approx 13\text{mm}$. More importantly, the value dM does not depend on time, which means that potential image processing errors might shift the measured mean-squared displacement $M'(t)$ towards higher mean-squared displacement, but can not change the time dependence of $M'(t)$. In particular, important features like a supposed plateau in the mean-squared displacement can not be destorted by image processing errors.

However, the upper threshold for tracking errors of $\sim$ 13mm is larger than $\frac{d_A}{2}$, while length scales in the order of $\frac{d_A}{10}$ are particularely interesting for investigating glassy dynamics. Therefore, an additional mechanism for preventing swaps of particles is implemented to the image processing algorithm:

All individual squared displacements $S_{i,\tau}(t) = (\vec{r}_i(\tau + t) - \vec{r}_i(\tau))^2$ for a particular time difference t. The median squared displacement $\overline{S}(t)$ is calculated. Now, all squared displacements which are larger than $100\overline{S}(t)$ are rejected and the measured mean squared displacement $M'(t)$ is calculated from the remaining squared displacements.

This prevents the algorithm from swaping particles, which are farther away from each other than $10\sqrt{\overline{S}(t)}$, which reduces the upper threshold

dM of the offset due to particle confusion to[3]

$$dM(t) \sim 50 p_w \overline{S}(t) \tag{4.23}$$

Because $\overline{S}(t)$ is in the order of magnitude of the actual mean-squared displacement $M(t)$, this leads to

$$dM(t) \sim 50 p_w M(t) \tag{4.24}$$

Having $p_w < 0.005$, this yields:

$$dM(t) < 0.25 M(t) \tag{4.25}$$

This means, that the measured mean-squared displacement will deviate less then 25% from the actual mean-squared displacement. In addition, the upper threshold of 180.5mm^2 for the error in the measured $M(t)$ is still valid.

4.3 Results

Particle trajectories are measured for different densities φ of a 2D bidisperse granular fluid. The granular fluid consists of 50% large particles with diameters d_A = 20mm and 50% small particles with diameters d_B = 16mm. For each density, the particle trajectories are measured at three different frame rates in order to investigate the system behavior both in the short time and in the long time regime. The used frame rates are 0.2fps, 10fps and 480fps. While for the measurement at 0.2fps a high-resolution (4008×2672px^2) Lumenera camera is used, the measurements at 10fps and 480fps are done with a Phantom high-speed camera, which has a lower resultion (2400×1800px^2), but is able to work at higher frame rates.

The dynamics of the granular fluid are measured at different densities φ, ranging from $\varphi = 0.6$ to $\varphi = 0.76$. However, measurements at higher densities are not possible with the mentioned experimental setup: At high

[3] A particle can now only be confused with particles within a circle of radius $R = 10\sqrt{\overline{S}(t)}$. This means, that the average squared displacement $< D >$ which results from such a potential confusion can be calculated by integrating over this area as: $< D >= \frac{1}{\pi R^2} \int_0^R 2\pi r r^2 dr = \frac{R^2}{2} = 50\overline{S}(t)$.

densities, the average particle-particle distance becomes very small and therefore the particles can execute significant forces onto each other. If a group of particles is pressed into one direction in a dense system, this can put a significant pressure on individual particles, which can lead to permanent particle overlaps. With increasing time of measurement, the number of permanently overlapping particles grows, which effectively changes the system denisity and the particle dynamics.

Therefore, measurements at higher densities than $\varphi = 0.76$ are omitted. However, the increase of pressure between particles and the observed collective dynamics at higher densities may also indicate that the system is close to a glassy state.

4.3.1 Pair Distribution Functions

From the data measured at 0.2fps, particle pair distributions $g(r)$ are calculated. Particle-particle distances r are measured within each individual frame and $g(r)$ is calculated as a histogram of all distances r with a binning b of 1px $\approx \frac{1}{135}\mathrm{d_A}$:

First, preliminary pair distribution functions $g^p(r)$ are calulated as

$$g^p_{k,l}(r) = \frac{N_{k,l}(r \leq \rho < r + b)}{N_k} \frac{1}{2\pi r b} \tag{4.26}$$

k and l indicate the species of particles, whose distances are evaluated. This can be either all particles (T), large particles only (A), or small particles only (B). E.g., $g^p_{A,B}(r)$ denotes the number density of B-particles seen at a distance $\rho \in [r, r + b)$ from A-particles. $N_{k,l}(r \leq \rho < r + b)$ is the number of l-particles seen at a distance $\rho \in [r, r + b)$ from k-particles and N_k is the number of k-particles.

Now the actual pair distribution functions $g_{k,l}(r)$ are normalized in a way, that for an infinite system $\lim_{r\to\infty} g_{k,l} = 1$ is true. This is done by normalizing with the number density of l-particles within the sample area.

$$g_{k,l}(r) = g^p_{k,l}(r) \frac{\pi r_E^2}{N_l / N_f} \tag{4.27}$$

φ	N_A (actual)	N_B (actual)	N_A (identified)	N_B (identified)
0.6	132	132	111.3	78.4
0.65	143	143	115.7	75.8
0.7	154	154	129.7	85.4
0.72	158	158	137.5	82.6
0.75	165	165	142.9	94.5
0.76	167	167	142.3	90.7

Table 4.1: Numbers of actual and identified large (A) and small (B) particles for different densities of the dense granular fluid.

r_E is the radius of the sample area and N_f is the number of considered frames, so that $\frac{N_l}{N_f}$ is the average number of l-particles per frame. Thereby, $\frac{N_l}{N_f}$ is in general smaller than the actual number of particles within the system, because the image processing algorithm is usually not able to identify all particles. The average numbers of identified particles and the actual numbers of particles for different system densities are shown in table 4.1

While, on average, about 80% of the large particles could be identified, only about 50% to 60% of the small particles could be identified. This might be because for small particles the distance between the particle boundary and the particle label is much smaller than for large particles (cf. fig. 4.4). This might prevent the image processing algorithm from properly identifying the label.

However, the fact that the image processing algorithm has a significant probability of failing at identifying a particle, does only decrease the statistics of the pair distribution function, but does not cause systematic errors. The failure rate is already taken into account by the normalization in equation (4.27). Potential systematic errors could only be caused by finding particles at wrong positions. However, the image processing algorithm is optimized in a way, that it is much less likely to falsely identify particles than to fail at identifying particles.

The resulting pair distribution functions $g_T(r)$ can be seen in figure 4.5. All pair distribution functions decrease quickly below 1 for higher distances. This is caused by the finite size of the sample area: Provided a homogenous

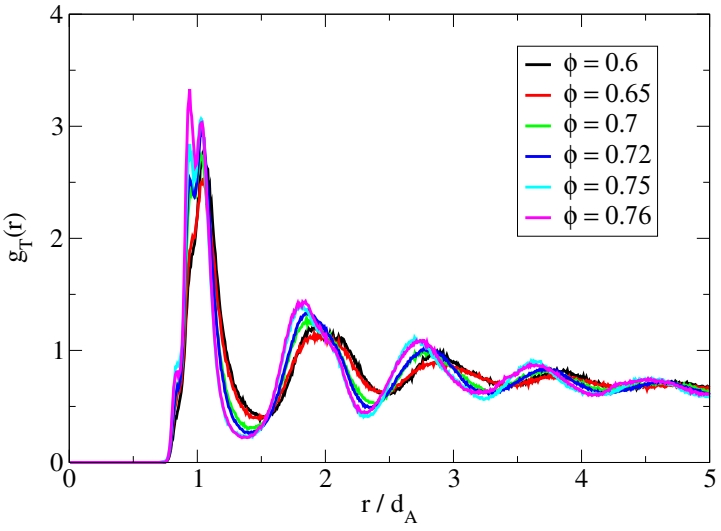

Figure 4.5: Total pair distribution functions $g_T(r)$ for granular fluids with densities $\varphi = 0.6$, $\varphi = 0.65$, $\varphi = 0.7$, $\varphi = 0.72$, $\varphi = 0.75$ and $\varphi = 0.76$.

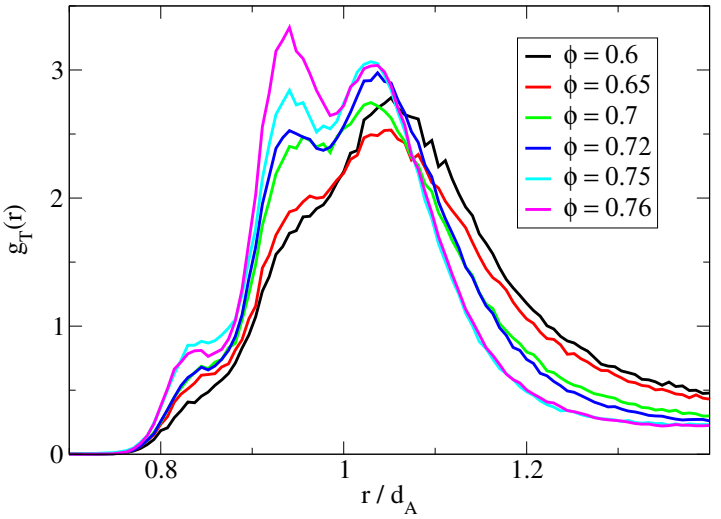

Figure 4.6: First peak of total pair distribution functions $g_T(r)$ for granular fluids with densities $\varphi = 0.6$, $\varphi = 0.65$, $\varphi = 0.7$, $\varphi = 0.72$, $\varphi = 0.75$ and $\varphi = 0.76$.

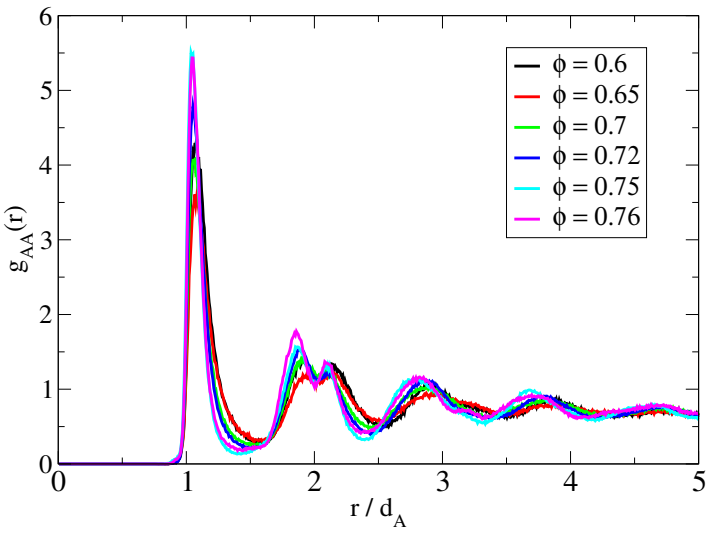

Figure 4.7: Partial pair distribution functions $g_{AA}(r)$ for granular fluids with densities $\varphi = 0.6$, $\varphi = 0.65$, $\varphi = 0.7$, $\varphi = 0.72$, $\varphi = 0.75$ and $\varphi = 0.76$.

particle distribution, $1 - \frac{(r_E - d_A)^2}{r_E^2} \approx 20\%$ of the particles are closer than d_A to the system boundaries and $1 - \frac{(r_E - 2*d_A)^2}{r_E^2} \approx 37.3\%$ of the particles are closer than $2d_A$ to the system boundaries.

The influence of the system density on the $g_T(r)$ can be clearly seen: For higher densities, the peaks of the pair distribution become larger and more pronounced. Also, the peaks shift to smaller distances, because the particles are pushed closer together.

The first peak of the total pair distribution function $g_T(r)$ is shown in detail in figure 4.6. The $g_T(r)$ is almost zero for distances below $d_B = 0.8d_A$, where d_B is the diameter of small particles. It then exhibits a shoulder for distances between $0.8d_A$ and $0.9d_B$, which is caused by small particles neighboring other small particles. At distances between d_A and $1.1d_A$, a peak in the $g_T(r)$ can be seen. This peak is caused by large particles neighboring other large particles.

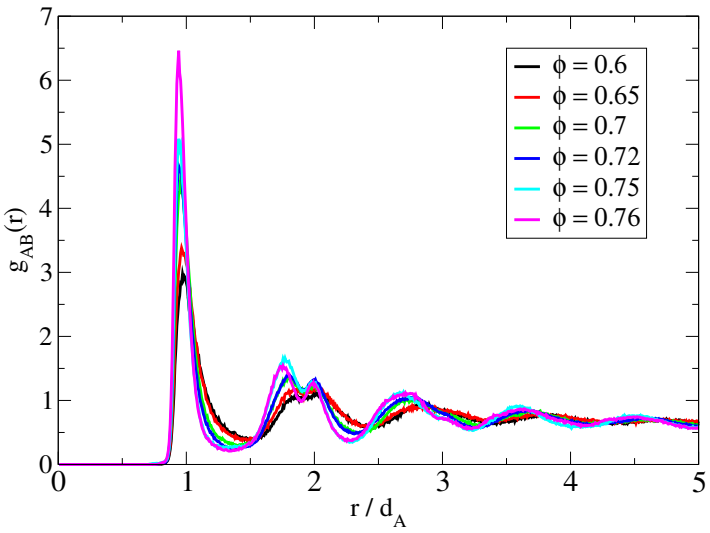

Figure 4.8: Partial pair distribution functions $g_{AB}(r) = g_{BA}(r)$ for granular fluids with densities $\varphi = 0.6$, $\varphi = 0.65$, $\varphi = 0.7$, $\varphi = 0.72$, $\varphi = 0.75$ and $\varphi = 0.76$.

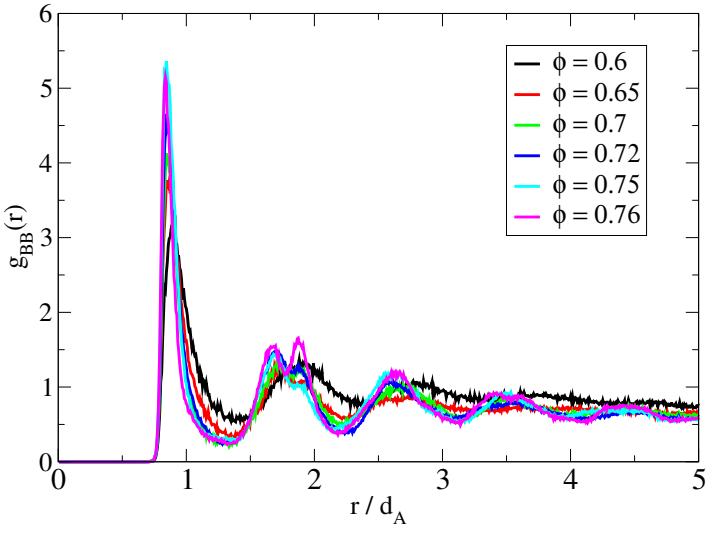

Figure 4.9: Partial pair distribution functions $g_{BB}(r)$ for granular fluids with densities $\varphi = 0.6$, $\varphi = 0.65$, $\varphi = 0.7$, $\varphi = 0.72$, $\varphi = 0.75$ and $\varphi = 0.76$.

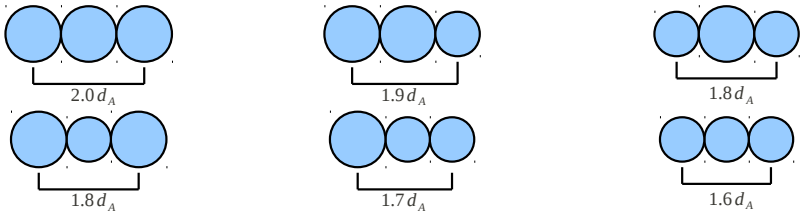

Figure 4.10: Possible contributions to partial pair distribution functions $g_{AA}(r)$ (left), $g_{AB}(r)$ (center) and $g_{BB}(r)$ (right).

For higher densities starting from $\varphi = 0.7$, another peak can be seen between $0.9d_A$ and d_A. This peak is caused by small particles neighboring big particles and becomes larger for higher densities. This means, that at larger densities the particles tend to arrange in structures combining large and small particles, probably since the available area can be used more efficiently by such structures.

The left edge of the first peak in $g_T(r)$ moves to smaller distances and becomes much steeper for higher densities. This also shows, that at heigher densities the particles are forced to arrange in a way, that they almost touch each other.

The partial pair distribution functions $g_{AA}(r)$, $g_{AB}(r)$ and $g_{BB}(r)$ are shown in figure 4.7, figure 4.8 and figure 4.9. The function g_{BA} is exactly the same as g_{AB} and is therefore not shown. For all partial pair distribution functions, the second peak is relatively smooth at low densities but gets split into two peaks at higher densities:

Consider three particles in a row. The first and the last particle might for instance be large particles, so that this particle formation contributes to $g_{AA}(r)$. However, the particle in the middle can either be a large or a small particle. If it is a small particle, then the distance between the outer particles is $r = \frac{1}{2}d_A + d_B + \frac{1}{2}d_A = 1.8d_A$. If it is a large particle, the distance between the outer particles is $2d_A$. This means, that for dense systems it is more likely to find two large particles with a distance of $1.8d_A$ or $2.0d_A$, than for example, with a distance of $1.9d_A$. This leads to the observed split of the second peak of the $g_{AA}(r)$. However, for less dense systems, the

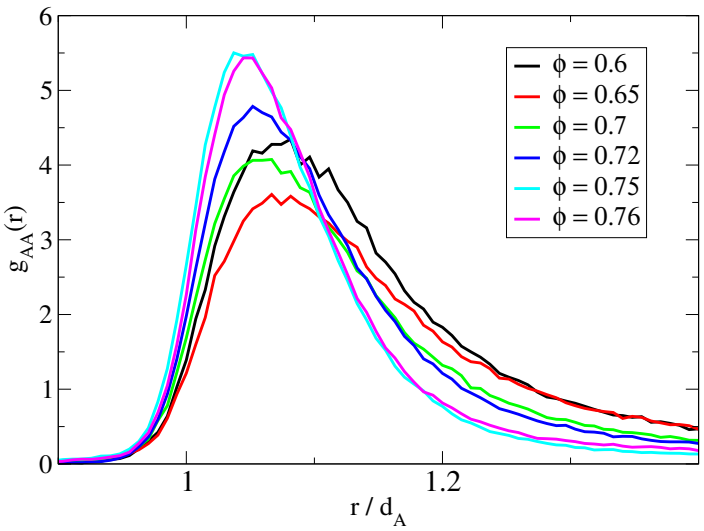

Figure 4.11: First peak of partial pair distribution functions $g_{AA}(r)$ for granular fluids with densities $\varphi = 0.6$, $\varphi = 0.65$, $\varphi = 0.7$, $\varphi = 0.72$, $\varphi = 0.75$ and $\varphi = 0.76$.

particles are on average not aligned that strictly, which makes the second peak broader and its structure less distinct.

Similiar arguments can be made about the structure of the second peak of the partial pair distribution functions $g_{AB}(r)$ and $g_{BB}(r)$. Possible configurations of aligned particles, which can contribute to the according pair distribution functions, are shown in figure 4.10.

The first peaks of the partial pair distribution functions are shown in figure 4.11, figure 4.12 and figure 4.13. For all pair distribution functions, the first peak becomes larger and more pronounced at higher densities. However, this effect is most significant for the pair distribution function $g_{AB}(r)$. This is consistent with the observation from the total pair distribution functions, that the particles tend to order in pairs of large and small particles at higher densities.

The first peak of $g_{AA}(r)$ first decreases from $\varphi = 0.6$ to $\varphi = 0.65$ and then starts to grow for increasing densities again. This means, that pairs of large particles become significantly less favored when the density raises

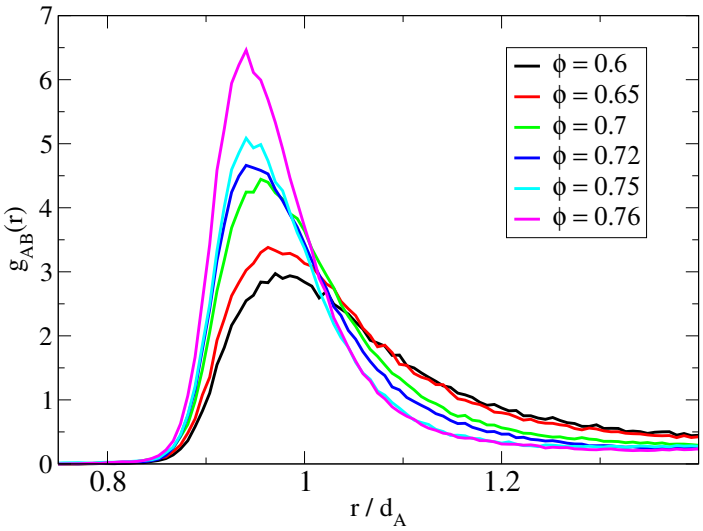

Figure 4.12: First peak of partial pair distribution functions $g_{AB}(r) = g_{BA}(r)$ for granular fluids with densities $\varphi = 0.6$, $\varphi = 0.65$, $\varphi = 0.7$, $\varphi = 0.72$, $\varphi = 0.75$ and $\varphi = 0.76$.

above $\varphi = 0.6$. However, all pair distribution peaks tend to grow with increasing densities, so that this effect might be overcompensated by the overall growth of the first peak at densities above $\varphi = 0.65$.

In general, the pair distribution functions show no signs of crystallization within the system. Also, the increase of density can be seen very well in the pair distribution function, which means that the granular fluid is sufficiently homogenous (e.g., the particles do not cluster at lower densities).

4.3.2 Mean-Squared Displacements

From the particle trajectories, mean-squared displacements are calculated. The resulting mean-squared displacements are shown in figure 4.14.

The mean-squared displacement increases quickly at short times. At times of about ~ 0.02s, this increase slows down significantly. The extent

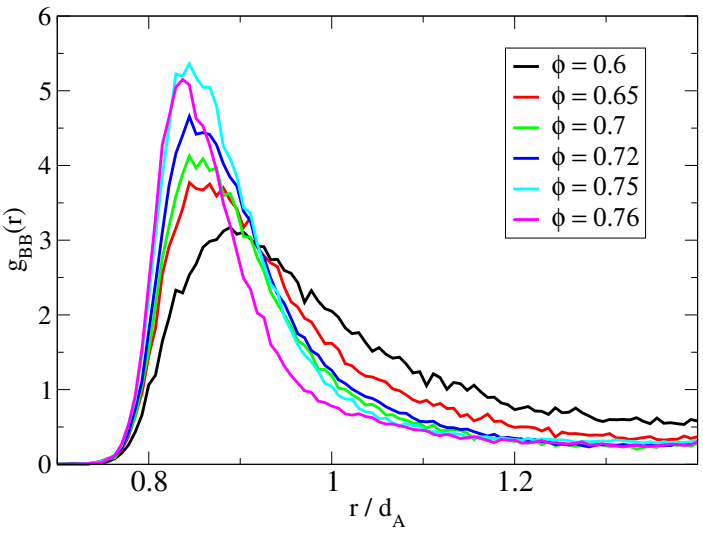

Figure 4.13: First peak of partial pair distribution functions $g_{BB}(r)$ for granular fluids with densities $\varphi = 0.6$, $\varphi = 0.65$, $\varphi = 0.7$, $\varphi = 0.72$, $\varphi = 0.75$ and $\varphi = 0.76$.

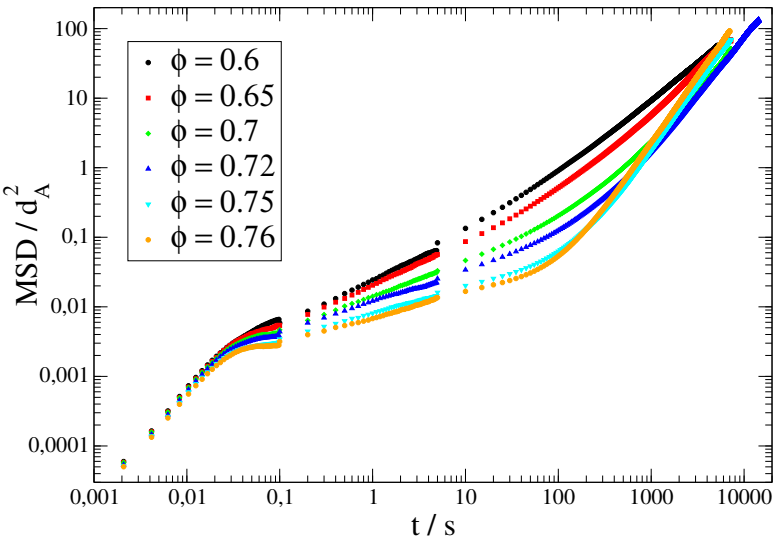

Figure 4.14: Mean-squared displacements of a 2D granular fluid at different densities φ.

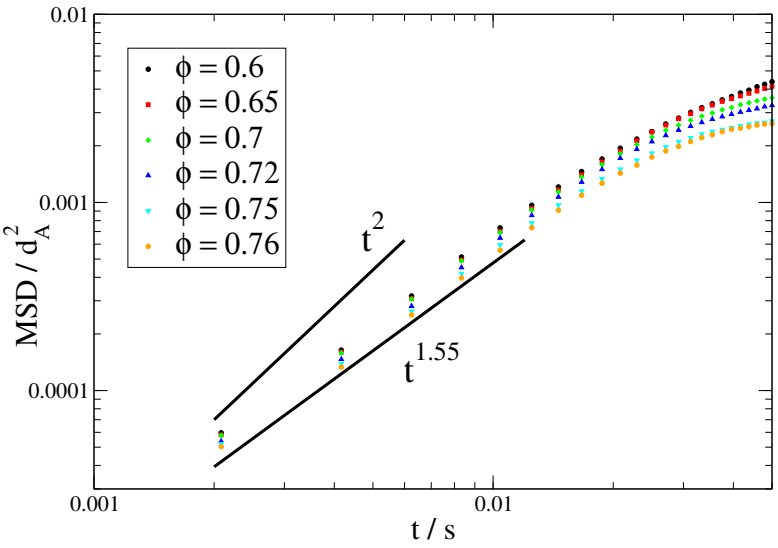

Figure 4.15: Mean-squared displacements of a 2D granular fluid at short times. An increase with $\sim t^{1.55}$ can be observed.

of this slowing down depends on the density: The higher the density, the slower the mean-squared displacement increases. However, at larger times the mean-square displacement increases rapidly again for all densities.

In figure 4.14, for some densities (e.g. $\varphi = 0.6$), small kinks in the mean-squared displacements can be seen at 0.1s and at 5s. This is because three different measurements, i.e. at 480fps, 10fps and 0.2fps, go into one mean-squared displacement curve.

Because the camera and the camera settings have to be changed between measurements at different frame rates, the according mean-squared displacements can not be measured at the same time. Also, the short-time mean-squared displacements are only averaged over several seconds, while the long-time mean-squared displacements are averaged over times between 2 and 4 hours. Finally, the resolution of the Phantom high-speed camera which is used for the short-time measurements is smaller than the resolution of the Lumenera camera used for the long-time measurements, which makes it harder to identify the particles. This again leads to lower statistics at short times.

Therefore, the kinks between mean-squared displacements measured at different frame rates are probably due to statistical fluctuations of the system behavior. However, those kinks usually only shift the mean-squared displacement by less than 10% and therefore do not affect the qualitative features of the measured system dynamics.

Short-Time Dynamics

While the mean-squared displacements for different densities deviate from each other for long and intermediate times, at short times the system dynamics are very similiar (cf. fig. 4.15). All short-time mean-squared displacements increase with the same exponent, i.e. they follow a power law with $\sim t^{1.55}$. This means, that at those times the particles perform directed movements rather than a random walk. However, the particle movement is also not ballistic, which would be indicated by an exponent of 2. One reason for this might be, that different from the dynamics of a sphere in the Lorentz system (cf. sect. 3.3), the dynamics of cylinders with spherical caps are more complex.

Since the short-time movement of particles is non-ballistic, no microscopic velocity can be determined. However, it can be seen that the mean-squared displacement increases faster for lower densities already at short time. The short-time mean-squared displacement of the most dilute sample ($\varphi = 0.6$) is about twenty percent larger than the mean-squared displacement of the densest sample ($\varphi = 0.76$). Because this is a relatively small density dependence of the short-time dynamics, it should not have any significant impact on the long-time dynamics.

Aging

The initial state of the system might not be representative for the states which the system samples over time due to its own dynamics. Therefore, the mean-squared displacement after driving the system for a long time might deviate from the mean-squared displacement one would measure directly after leaving the initial state. Because the dynamics of systems close to the glass tranisition can become very slow, it can take a long time

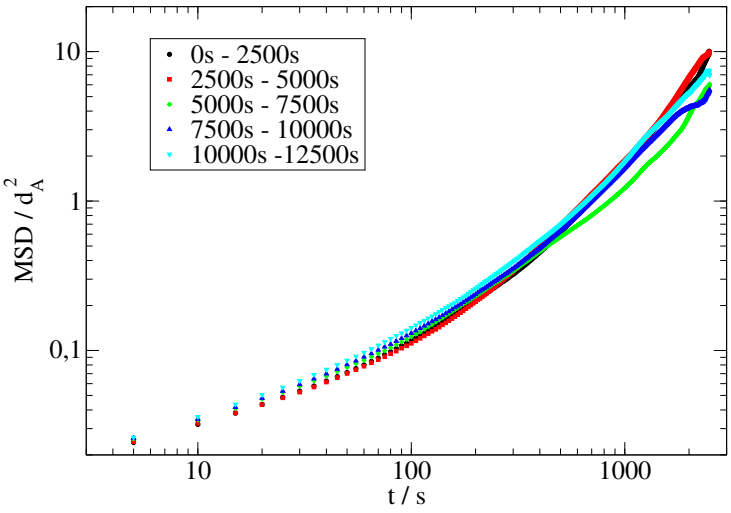

Figure 4.16: Mean-squared displacements of a dense granular fluid with the density $\varphi = 0.72$. The mean-squared displacements are calculated from subsequent time periods of the same measurement.

until the influence of the initial state on the mean-squared displacement has completely vanished. Therefore, in such systems the mean-squared displacement $M(t)$ can keep changing for a quite long time, until it finally becomes stable. This behavior is called *aging* [10].

In order to check if aging plays a role in the granular fluid experiment, the mean-squared displacement of the longest available run of measurement ($\varphi = 0.72$) is calculated for five subsequent time periods of 2500s each (cf. fig. 4.16).

It can be seen that the mean-squared displacements from the different time periods of the measurement slightly deviate from each other. However, no systematic change can be observed. For instance, the fastest long-time dynamics is observed for the first two time periods, while the third time period exhibits the slowest long-time dynamics and the forth and fifth time period are somewhere in between.

Thus, it is likely that the differences between the different time periods are either caused by statistical fluctuations either of the system dynamics

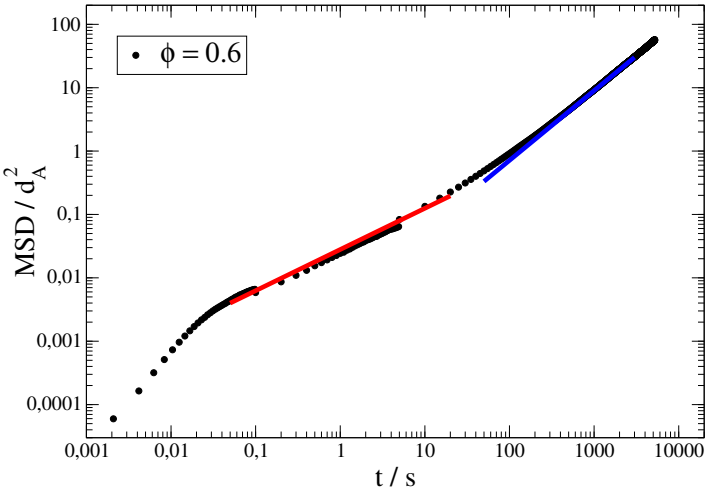

Figure 4.17: Mean-squared displacement for a granular fluid of the density $\varphi = 0.6$. The red line represents a manual fit to a function $\sim t^{0.65}$, while the blue line represents a manual fit to a function $\sim t^{1.1}$.

or by the fact that the image processing algorithm sometimes fails to identify particles. This means that it makes sense to average the mean-squared displacement over the whole time of measurement, as no substantial aging is observed.

Exponents at Intermediate and Long Times

In order to find exponents of the mean-squared displacement function $M(t)$ for intermediate and long times, the mean-squared displacements are plotted in figures 4.17, 4.18, 4.19, 4.20, 4.21, and 4.22. Functions $f(t)$ of the type

$$f(t) = bt^m \tag{4.28}$$

are fitted manually both to the intermediate- and the long-time part of $M(t)$.

It turns out that it is possible to properly fit such functions to the measured data for all considered densities. This means, the mean-squared displacement actually is proportional to t^m with certain exponents m both for intermediate and long times.

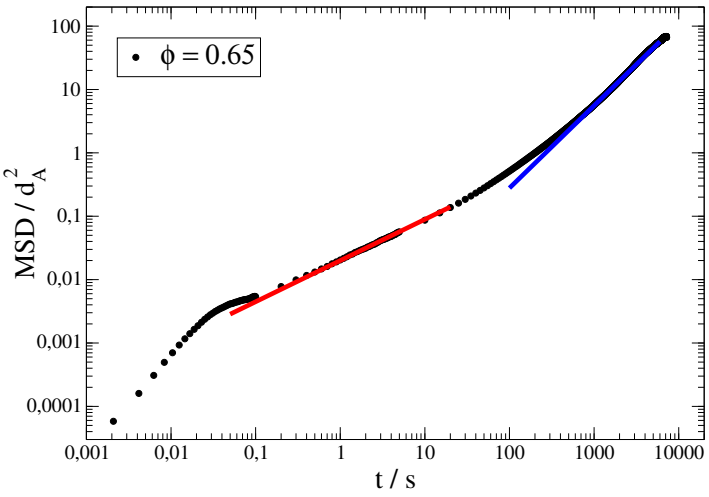

Figure 4.18: Mean-squared displacement for a granular fluid of the density $\varphi = 0.65$. The red line represents a manual fit to a function $\sim t^{0.65}$, while the blue line represents a manual fit to a function $\sim t^{1.3}$.

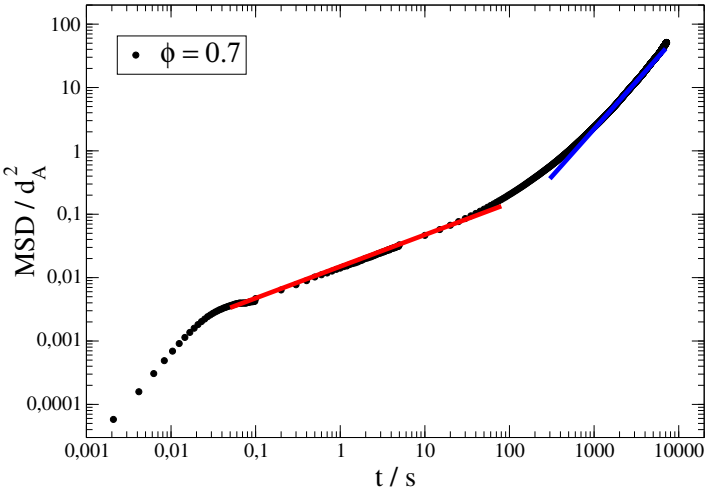

Figure 4.19: Mean-squared displacement for a granular fluid of the density $\varphi = 0.7$. The red line represents a manual fit to a function $\sim t^{0.5}$, while the blue line represents a manual fit to a function $\sim t^{1.5}$.

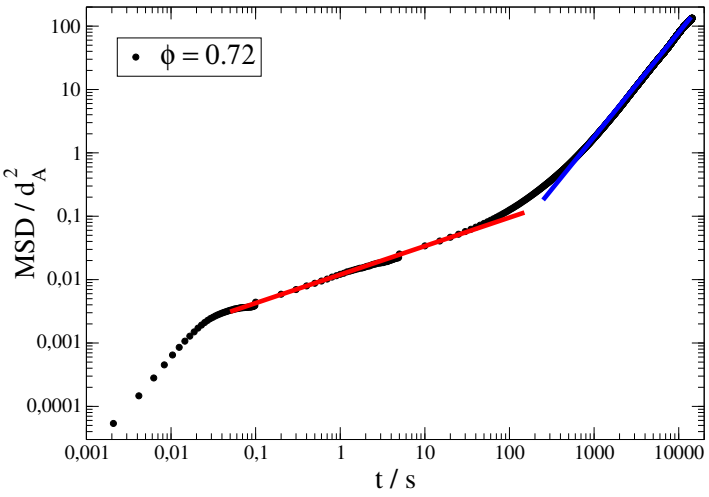

Figure 4.20: Mean-squared displacement for a granular fluid of the density $\varphi = 0.72$. The red line represents a manual fit to a function $\sim t^{0.45}$, while the blue line represents a manual fit to a function $\sim t^{1.65}$.

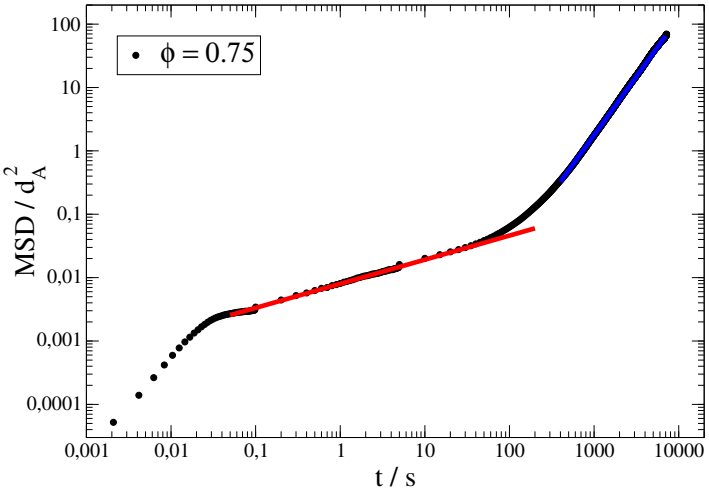

Figure 4.21: Mean-squared displacement for a granular fluid of the density $\varphi = 0.75$. The red line represents a manual fit to a function $\sim t^{0.38}$, while the blue line represents a manual fit to a function $\sim t^{1.85}$.

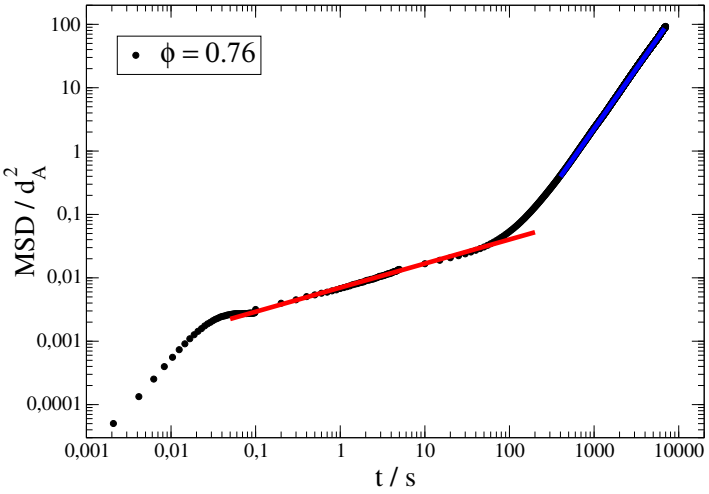

Figure 4.22: Mean-squared displacement for a granular fluid of the density $\varphi = 0.76$. The red line represents a manual fit to a function $\sim t^{0.38}$, while the blue line represents a manual fit to a function $\sim t^{1.9}$.

φ	0.6	0.65	0.7	0.72	0.75	0.76
m_I	0.65	0.65	0.5	0.45	0.38	0.38
b_I	0.028	0.02	0.015	0.012	0.008	0.007

Table 4.2: Parameters of a function $f(t) = b_I t^{m_I}$ fitted to the mean-squared displacement of a dense granular fluid at intermediate times for different densities.

The parameters for the manual fits at intermediate times are listed in table 4.2.

The obtained exponent m_I is always smaller then one and decreases for increasing densities. This indicates that the system approaches a glassy state, at which the mean-squared displacement would become localized. However, the exponent $m_I = 0.38$ at the highest measured density $\varphi = 0.76$ is still significantly larger than zero.

The parameters for the manual fits at long times are listed in table 4.3.

φ	0.6	0.65	0.7	0.72	0.75	0.76
m_L	1.1	1.3	1.5	1.65	1.85	1.9
b_L	0.0045	0.0007	7e-5	2e-5	5e-6	4.5e-6

Table 4.3: Parameters of a function $f(t) = b_L t^{m_L}$ fitted to the mean-squared displacement of a dense granular fluid at long times for different densities.

The exponent m_L is always larger than one, which means that there is a contribution of directed movement to the long time dynamics. Also, it can be seen that this directed movement becomes more significant for higher densities. However, from visual observations it can be concluded, that the center of mass of the system does not move significantly during measurement. Also, at higher densities it would become more difficult for the center of mass to move than at lower densities. Therefore, if the long-time dynamics of the system would be caused by a movement of the center of mass, one would expect a decrease of these dynamics for increasing densities.

However, the system could also rotate collectively. Because the sample area is circular, a collective rotational movement is possible at all densities. This means, while the particles can get localized at higher densities relative to each other, such localization would still not prevent them from collectively moving into an angular direction.

4.3.3 Radial Mean-Squared Displacements

In order to check for a possible collective rotational movement, a radial mean-squared displacement is defined as follows: First, the center $\vec{c}$ of the sample area is determined. Then, a radial mean-squared displacement $M_R(t)$ is calculated as:

$$M_R(t) =< (|\vec{r}_i(\tau + t) - \vec{c}| - |\vec{r}_i(\tau) - \vec{c}|)^2 >_{i,\tau} \tag{4.29}$$

For small times and displacements, the radial mean-squared displacement should exactly equal $\frac{1}{2}$ of the mean-squared displacement $M(t)$. On the other hand, it has to become smaller than $\frac{1}{2}M(t)$ for the larger displacements, since a particle moving through the center of the system might cover a significant distance but still end up at the same radial position $|\vec{r} - \vec{c}|$. However, this effect can be considered as another finite size effect,

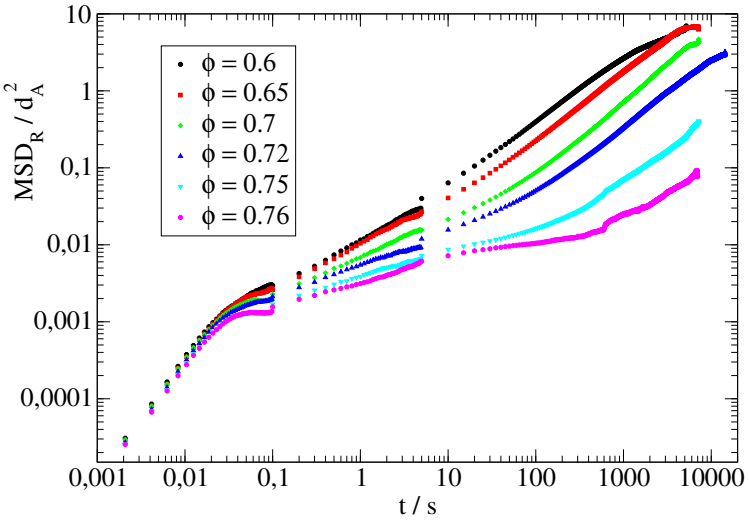

Figure 4.23: Radial mean-squared displacements for granular fluids at different densities.

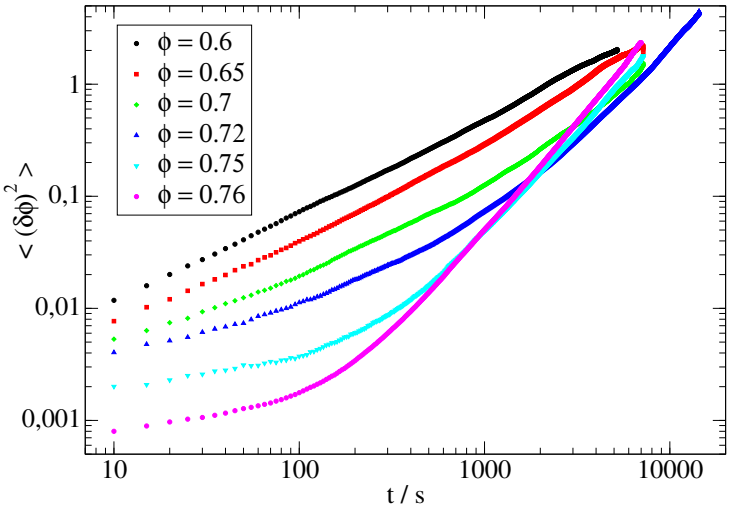

Figure 4.24: Mean-squared angular displacements for granular fluids at different densities.

which should not affect the qualitative features of $M_R(t)$.

The radial displacements of the granular fluid at different densities are shown in figure 4.23. The radial mean-squared displacements show a similiar behavior to the mean-squared displacements shown in figure 4.14. For instance, the increase of the radial mean-squared displacement slows down at intermediate times and becomes faster again at longer times. However, the exponent does not rise above one at long times anymore. Also, other than the total mean-squared displacements, the radial mean-squared displacements for higher densities no longer cross the radial mean-squared displacements for lower densities at long times.

In addition, it can be seen that the radial mean-squared displacements for high densities $\varphi = 0.75$ and $\varphi = 0.76$ stay slow for longer times than the corresponding total mean-squared displacements.

Mean-Squared Angular Displacements

The fact, that the radial mean-squared displacements do not exhibit exponents above 1 for long times indicates that the large exponents in the total mean-squared displacement have to be caused by a rotational motion. However, in order to check this hypothesis, also a mean-squared angular displacement is defined as:

$$M_\varphi := < ((\vec{r_i})_\varphi(\tau + t) - (\vec{r_i})_\varphi(\tau))^2 >_{i,\tau} \tag{4.30}$$

Thereby, the φ-component of the particle positions $\vec{r_i}$ is defined as the angular coordinate within a cylindrical coordinate system with origin in the center of the sample area. Also, it is taken care of, that the absolute values of the differences of the angular components φ do not exceed π. If this is the case, the algorithm for calculating the mean-squared angular displacement adds or substracts an multiple of 2π to that difference in order to map it back onto the interval $[-\pi, \pi]$.

The mean-squared angular displacements of the granular fluid are shown in figure 4.24. It can be seen, that all mean-squared angular displacements increase with exponents greater than 1 at long times. The higher the density, the higher those exponents become. This also makes the high-density mean-squared angular displacements cross the low-density mean-squared

angular displacements at long times, like it is observed for the total mean-squared displacement (cf. fig. 4.14).

Therefore, it can be concluded that the fast increase of total mean-squared displacements at long times is solely caused by a directed angular movement. The fact that this effect becomes more significant for higher densities can be explained as follows: At low densities, the particles can still move relatively freely towards each other. Thus, the angular movements of the particles are not neccessarily correlated with each other. However, for larger densities, a particle can only move significantly into one direction (in this case angularely), if all other particles do also move into that direction.

Therefore, the angular movement becomes a collective movement for higher densities. This seems to make the movement more persistent: It is probably more difficult for a particle to change its direction of movement, if the system is moving collectively, than if every particle is able to move freely relative to other particles.

Detailed Analysis of Radial Mean-Squared Displacements

In order to avoid the influence of collective angular movements, it makes sense to analyse the radial mean-squared displacements instead of the total mean-squared displacements.

The short-time behavior of radial mean-squared displacements is shown in figure 4.25. Again, the short-time dynamics are similiar for all densities. However, it can be seen that the particles move slightly faster in low density systems than in high density systems. E.g., at a density of $\varphi = 0.6$ the short-time radial mean-squared displacement is about 25% larger than at a density of $\varphi = 0.76$. However, all radial mean-squared displacements increase with $\sim t^{1.55}$ at short times. This is very similiar to the short-time behavior of the total mean-squared displacements, which shows that the collective angular movement does not play a role at short times.

Functions of the type

$$f(t) = bt^m \tag{4.31}$$

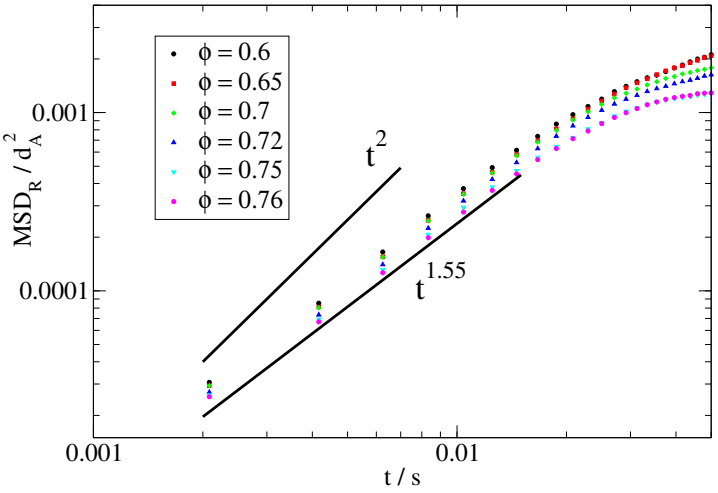

Figure 4.25: Short-time behavior of the radial mean-squared displacement of granular fluids at different densities. The short-time increase follows $\sim t^{1.55}$.

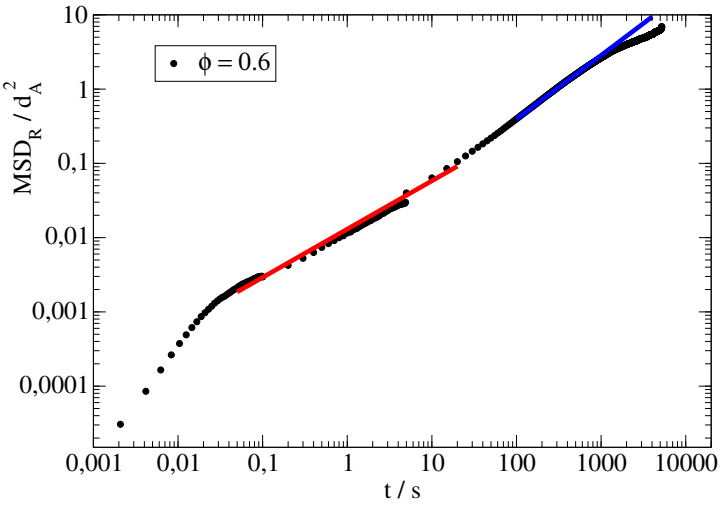

Figure 4.26: Radial mean-squared displacement for a granular fluid of the density $\varphi = 0.6$. The red line represents a manual fit to a function $\sim t^{0.65}$, while the blue line represents a manual fit to a function $\sim t^{0.86}$.

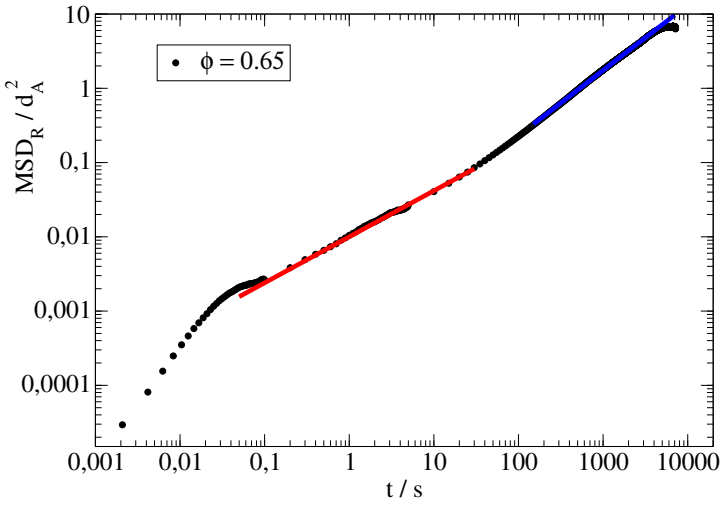

Figure 4.27: Radial mean-squared displacement for a granular fluid of the density $\varphi = 0.65$. The red line represents a manual fit to a function $\sim t^{0.62}$, while the blue line represents a manual fit to a function $\sim t^{0.88}$.

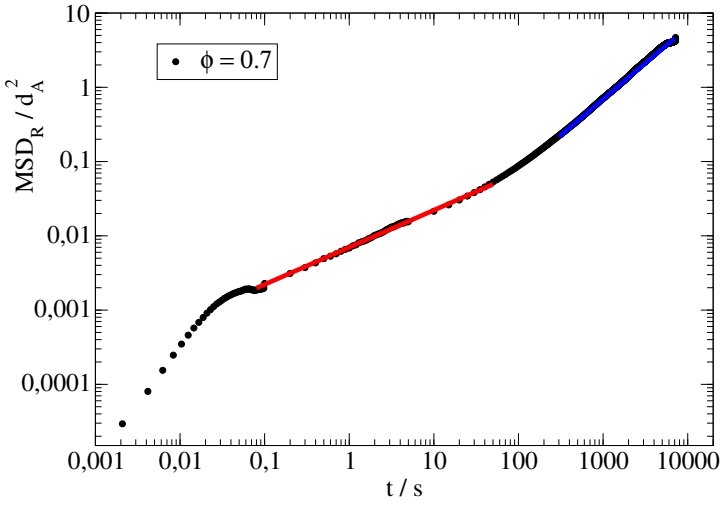

Figure 4.28: Radial mean-squared displacement for a granular fluid of the density $\varphi = 0.7$. The red line represents a manual fit to a function $\sim t^{0.5}$, while the blue line represents a manual fit to a function $\sim t^{0.97}$.

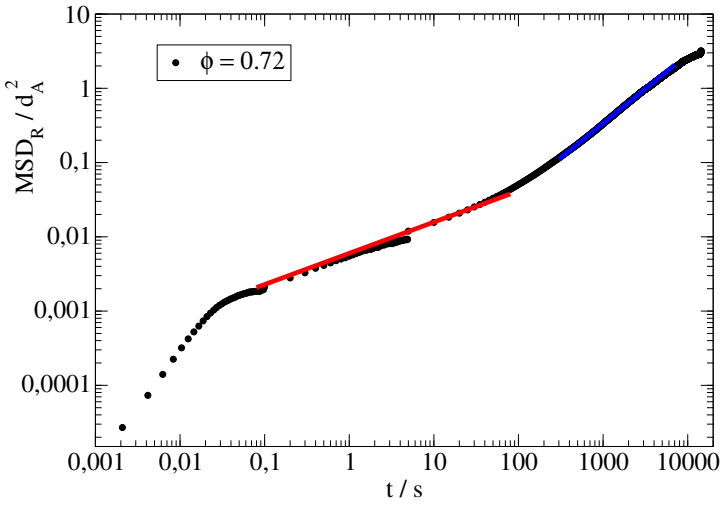

Figure 4.29: Radial mean-squared displacement for a granular fluid of the density $\varphi = 0.72$. The red line represents a manual fit to a function $\sim t^{0.42}$, while the blue line represents a manual fit to a function $\sim t^{0.93}$.

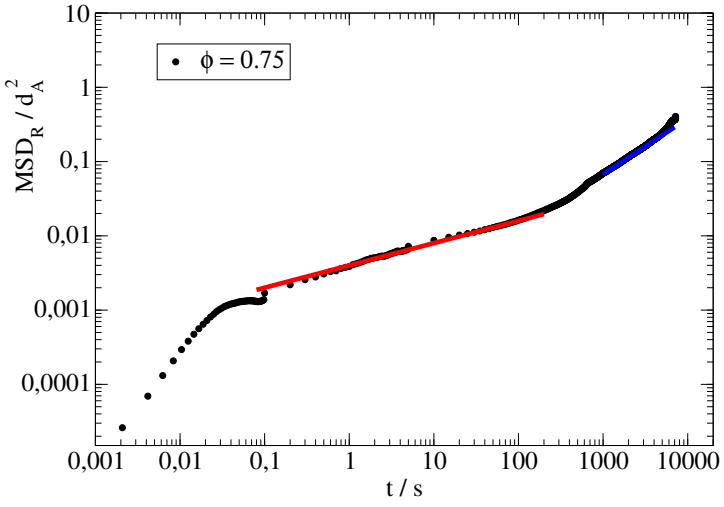

Figure 4.30: Radial mean-squared displacement for a granular fluid of the density $\varphi = 0.75$. The red line represents a manual fit to a function $\sim t^{0.3}$, while the blue line represents a manual fit to a function $\sim t^{0.75}$.

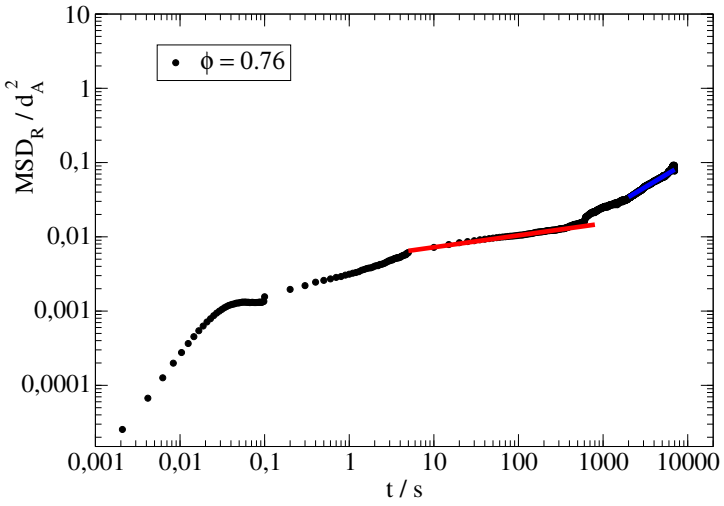

Figure 4.31: Radial mean-squared displacement for a granular fluid of the density $\varphi = 0.76$. The red line represents a manual fit to a function $\sim t^{0.16}$, while the blue line represents a manual fit to a function $\sim t^{0.68}$.

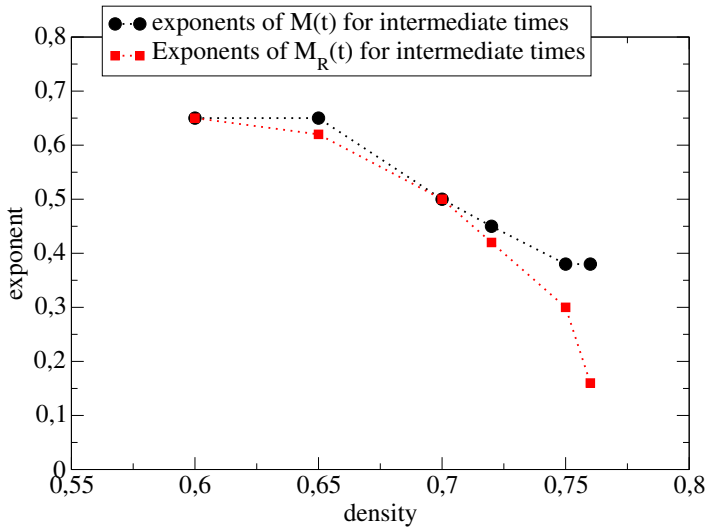

Figure 4.32: Exponents for intermediate times at different densities obtained from the total mean-squared displacement (black) and the radial mean-squared displacement (red).

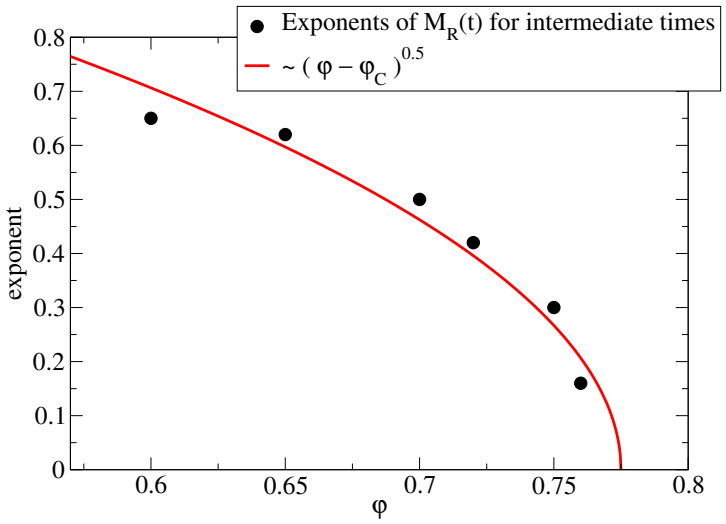

Figure 4.33: Fit of a square-root function $\sim (\varphi_c - \varphi)^{0.5}$ to the exponents for intermediate times of the radial mean-squared displacements. The fit indicates a glass transition density $\phi_c \approx 0.775$.

φ	0.6	0.65	0.7	0.72	0.75	0.76
m_I	0.65	0.62	0.5	0.42	0.3	0.16
b_I	0.013	0.01	0.007	0.006	0.004	0.005

Table 4.4: Parameters used to fit a function $f(t) = b_I t^{m_I}$ to the intermediate-time radial mean-squared displacements of a granular fluid at different densities.

are manually fitted to the measured radial mean-squared displacements both for intermediate and for long times. The fits are shown in figure 4.26, 4.27, 4.28, 4.29, 4.30, and 4.31. It can be seen, that fitting such functions to the data is possible for all densities both for intermediate and long times.

The used fitting parameters for intermediate times are listed in table 4.4.

The resulting exponents m_I are compared to the exponents obtained from the total mean-squared displacements in figure 4.32. It can be seen, that the exponents are very similiar for low densities up to a density of $\varphi = 0.72$. However, for higher densities the exponents obtained from the radial mean-squared displacements decrease much faster than the ex-

φ	0.6	0.65	0.7	0.72	0.75	0.76
m_L	0.86	0.88	0.97	0.93	0.75	0.68
b_L	0.0075	0.004	8.5e-4	5.5e-4	3.8e-4	1.95e-4

Table 4.5: Parameters used to fit a function $f(t) = b_L t^{m_L}$ to the long-time radial mean-squared displacements of a granular fluid at different densities.

ponents from the total mean-squared displacements. This shows, that the collective rotational movement of the particles partially distorts the indications of onsets of glassy dynamics in the total mean-squared displacement.

However, the increasingly fast decay of the exponents in the radial mean-squared displacement shows that the system is already close to the glass transition at $\varphi = 0.76$. Also, in figure 4.31 it can be seen that the radial mean-squared displacement exhibits a plateau-like behavior over more than four decades and up to a time of about ~ 1000s at this density.

The exponents m_I for intermediate times of the radial mean-squared displacements seem to follow a square-root function. In order to get a better estimate for the glass transition density, a function

$$f(\varphi) = a(\varphi_c - \varphi)^{0.5} \tag{4.32}$$

is fit to the measured m_I in figure 4.33. This fit indicates a glass transition density

$$\varphi_c \approx 0.775. \tag{4.33}$$

The fitting parameters for the radial mean-squared displacements at long times are shown in the table 4.5.

All exponents m_L are smaller than 1. The measured exponents increase for increasing densities up to $\varphi = 0.7$, where a diffusive behavior can be observed. However, for higher densities the exponent starts to decrease again.

One could suppose that the apparent exponents for $\varphi = 0.6$ and $\varphi = 0.65$ are decreased due to finite size effects. However, the system radius is $r_E = 190$mm, which equals 9.5 times the large particle diameters d_A. The according mean-squared displacement equals $r_E^2 = 90.25$. The maximum measured mean-squared displacements for $\varphi = 0.6$ and $\varphi = 0.65$ are still

by one order of magnitude smaller.

However, the radial mean-squared displacement is affected by finite size effects already before the maximum possible displacement is reached. In particular, the apparent movement of particles crossing the center of the system is systematically underestimated by the radial mean-squared displacement. If the displacements grow, it becomes more and more likely for a particle to cross through the system center. Therefore, the comparebly small exponents at low densities might very well be caused by finite size effects. However, in order to further investigate this point, measurements at larger systems or at systems with a geometry which prevents collective angular movements would be neccessary.

The decrease of long-time exponents for densities above $\varphi = 0.7$ might be due to the onset of glassy dynamics at higher density. Possibly, the intermediate time period of slowly increasing mean-squared displacements would grow towards higher times, if the system would have more time to age. However, it has been shown that no effects of ageing can be seen at the time scales at which the system dynamics is measured. For further investigating the long-time behavior at higher densities, the duration of measurements has to be increased greatly.

Radial Mean-Squared Displacements of Large and Small Particles

The radial mean-squared displacements of large particles only and small particles only are compared for granular fluids at different densities in figures 4.34, 4.35, 4.36, 4.37, 4.38, and 4.39.

For $\varphi = 0.6$, the small particles are moving slightly faster than the large particles at long times. The short-time part of figure 4.34 does not show this deviation. This is probably caused by the fact that the short time dynamic is not sampled over long times and therefore the measured dynamics are not fully representative for the system dynamics. However, the radial mean squared displacements of large and small particles stay parallel at long times, i.e. the long-time exponent does not depend on the particle size.

For all other densities no significant deviations between small-particle and large-particle dynamics can be seen. This means that the gaps between large particles are not big enough to let the small particles pass through

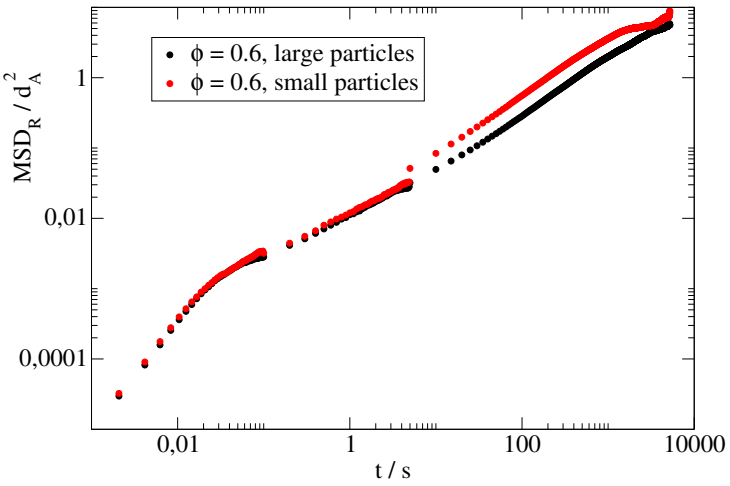

Figure 4.34: Comparison of radial mean-squared displacements of large and small particles for a granular fluid of the density $\varphi = 0.6$.

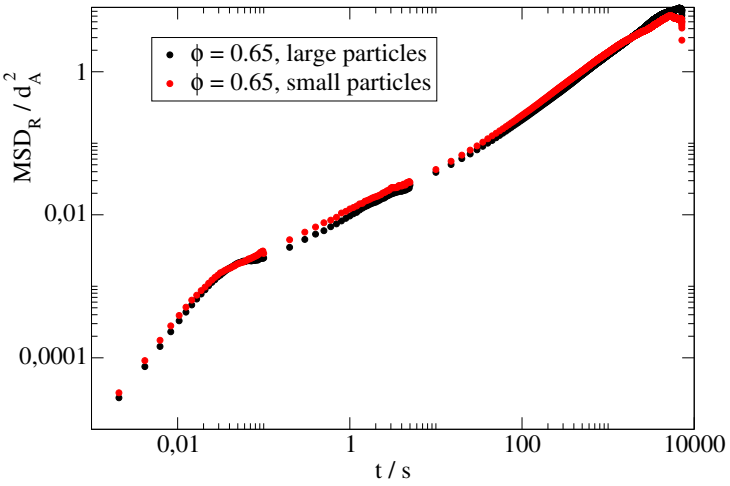

Figure 4.35: Comparison of radial mean-squared displacements of large and small particles for a granular fluid of the density $\varphi = 0.65$.

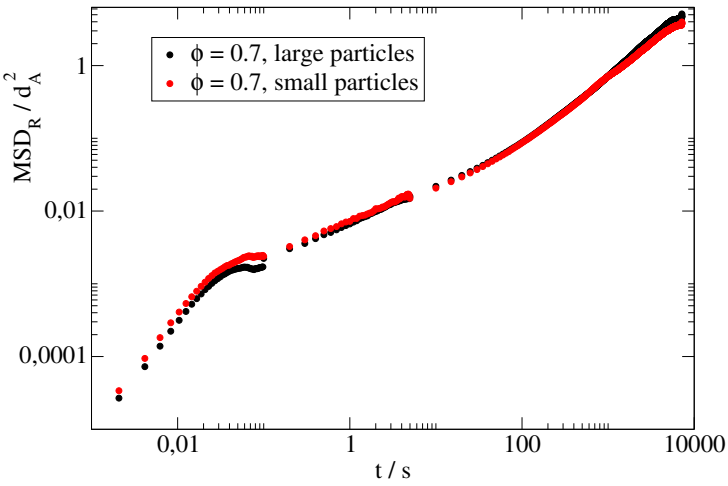

Figure 4.36: Comparison of radial mean-squared displacements of large and small particles for a granular fluid of the density $\varphi = 0.7$.

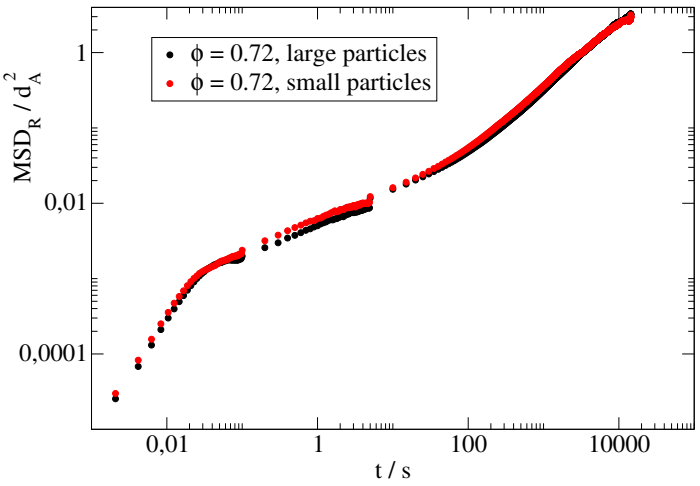

Figure 4.37: Comparison of radial mean-squared displacements of large and small particles for a granular fluid of the density $\varphi = 0.72$.

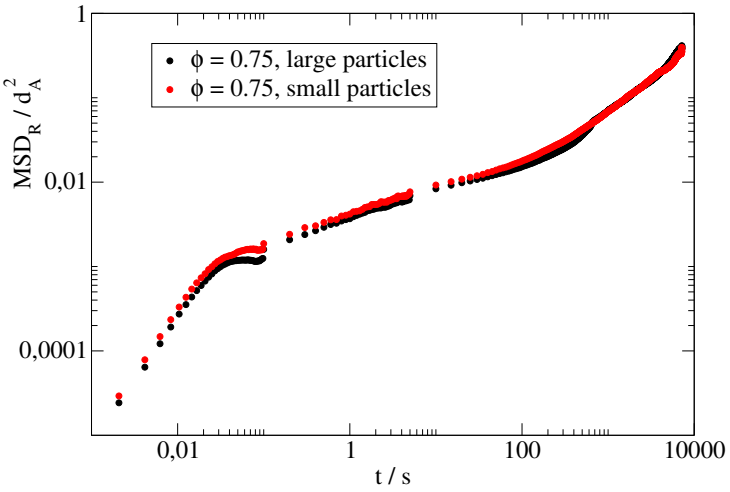

Figure 4.38: Comparison of radial mean-squared displacements of large and small particles for a granular fluid of the density $\varphi = 0.75$.

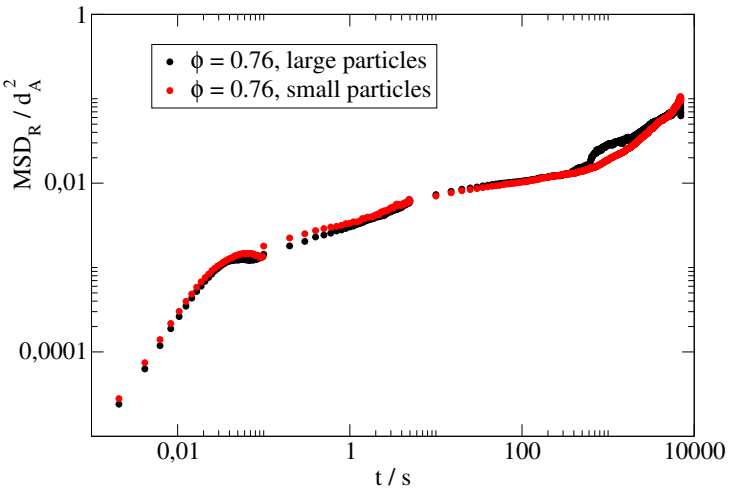

Figure 4.39: Comparison of radial mean-squared displacements of large and small particles for a granular fluid of the density $\varphi = 0.76$.

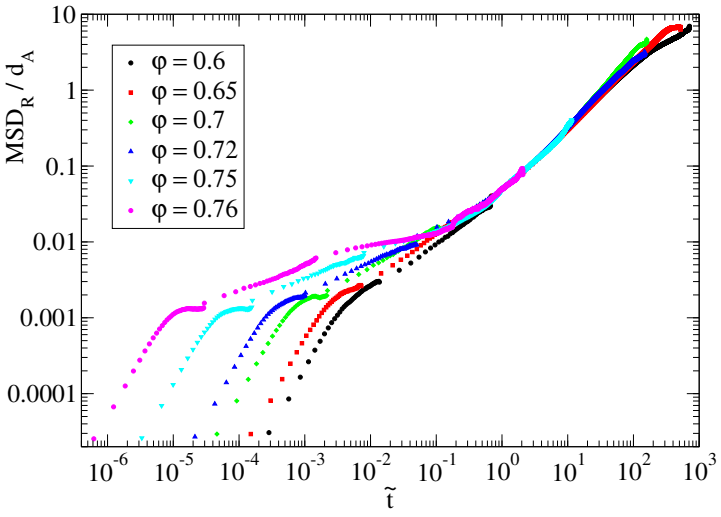

Figure 4.40: Scaled radial mean-squared displacements. The scaled time $\tilde{t}$ is calculated by dividing the actual times t by the corresponding scaling factors given in table 4.6.

and therefore both large and small particles are equally slowed down with increasing densities.

α-Scaling

In order to compare the long-time dynamics of radial mean-squared displacements, scaled radial mean-squared displacements $M_r'(\tilde{t})$ are calculated from the original radial mean-squared displacements $M_r(t)$ as follows:

$$M_r'(\tilde{t}) = M_r(\tilde{t}/\tau_\alpha(\varphi)) \tag{4.34}$$

Thereby τ_α is a density-dependent scaling factor. It is chosen in a way, that at the scaled time $\tilde{t} = 1$ all scaled radial mean-squared displacements $M_r'(\tilde{t})$ reach a value of $0.05 d_A$. The scaling factors τ_α are given in table 4.6. The scaled radial mean-squared displacements are shown in figure 4.40.

The scaled radial mean-squared displacements match each other well at large $\tilde{t}$, which indicates that α-scaling [25, 26] is applicable for the measured

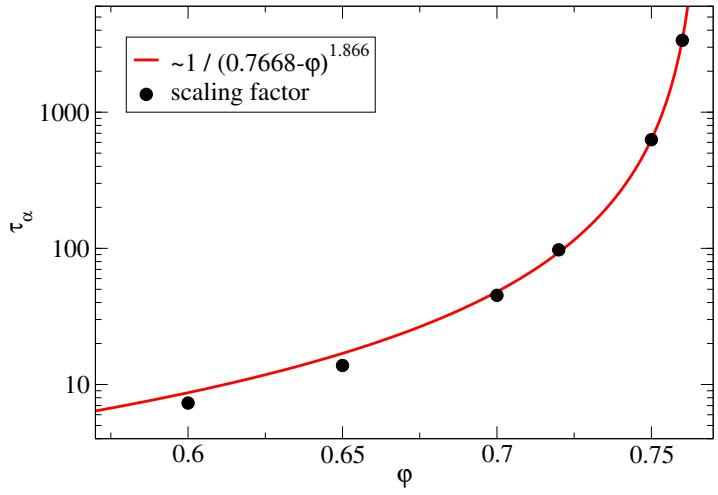

Figure 4.41: Scaling factors τ_α as a function of the system density φ. A function $s(\varphi) = \frac{a}{(\varphi_c - \varphi)^\gamma}$ can be fitted to the data with an exponent $\gamma = 1.866$ and a critical density $\varphi_c = 0.7668$.

φ	0.6	0.65	0.7	0.72	0.75	0.76
τ_α	7.31s	13.8s	45.2s	97.5s	628s	3370s

Table 4.6: Scaling factors τ_α of the radial mean-squared displacements for different densities φ.

data. As shown in figure 4.41, the scaling factors τ_α approximately follow a function

$$\tau_\alpha(\varphi) = \frac{a}{(\varphi_c - \varphi)^\gamma} \tag{4.35}$$

with a prefactor $a = 0.308$s, the glass transition density

$$\varphi_c = 0.7668 \approx 0.765 \tag{4.36}$$

and an exponent

$$\gamma = 1.866 \approx 1.87. \tag{4.37}$$

The obtained glass-transition density $\varphi_c \approx 0.765$ is consistent with the glass transition density $\varphi_c \approx 0.775$ resulting from the square-root fit of the exponents for intermediate times in section 4.3.3.

Mode-coupling calculations for a monodisperse system of hard disks in 2D predict a scaling exponent $\gamma = 2.38$. This is similiar to the above exponent $\gamma \approx 1.87$ for dense granular fluids.

4.3.4 Conclusion

The dynamics of a bidisperse granular fluid with a size ratio of 4/5 and a mixing ratio of 50% are measured at different densities between $\varphi = 0.6$ and $\varphi = 0.76$. Different from [23], the emergence of crystal structures can be avoided.

The onset of glassy dynamics can be seen very well in the radial mean squared-displacements: The emergence of a plateau at intermediate times can be observed already at the density $\varphi = 0.6$. The dynamics at intermediate times can be described by a function $f(t) = b_I t^{m_I}$. Beginning from $\varphi = 0.6$, the exponent m_I decreases and the length of the observed plateau increases continously with increasing densities.

At a density of $\varphi = 0.76$, a plateau with an exponent as small as $m_I = 0.16$ can be observed over more than four decades in the radial mean-squared displacement. This deviates significantly from [24], where even at a very high density $\varphi \approx 0.81$ only two decades of a plateau-like behavior with a rather high exponent $m_I \approx 0.4$ are observed.

Due to technical limitations, the system dynamics can not be observed

for densities above $\varphi = 0.76$. However, the fact that the exponent m_I is decaying increasingly fast at densities close to $\varphi = 0.76$ indicates that the actual glass transition happens probably at a slightly higher density than $\varphi = 0.76$. Also the scaling behavior of the radial mean-squared displacements suggests a glass transition at $\varphi \approx 0.767$. This might also explain the fact, that above $\varphi = 0.76$ the inter-particle pressure becomes large enough to produce permanent particle-overlapping.

Chapter 5

A 3D Granular Gas Experiment

5.1 Experiment: Magnetically Excited Granular Matter

MEGraMa (Magnetically Excited Granular Matter) is an experimental setup for the investigation of dilute granular gases under microgravity: A granular sample consisting of paramagnetic particles in a $5x5x5\text{cm}^3$ sample cell is agitated by oscillating magnetic fields in microgravity. Due to collisions with the sample cell walls, an apparently random movement of the granular particles can be achieved. After a few seconds, the magnetic fields are switched off and the granular particles start to gradually lose energy due to particle-particle and particle-wall collisions. This process is called granular cooling. The particle dynamics during this cooling process is to be investigated.

The MEGraMa experiment was performed with similiar setups both in parabolic flights and at a drop tower. Parabolic flights and drop tower experiments have different microgravity durations and qualities. While the parabolic flight experiments allow measuring under microgravity for about 22s at a time, the microgravity quality in parabolic flights is rather poor: Because it is difficult for an airplane to follow precisely a free-fall trajectory, during the microgravity time remaining accelerations up to 0.05g can occur. On the other hand, the drop tower allows only for microgravity measurement times of up to ~ 10s, but also limits remaining accelerations during microgravity to $\sim 10^{-5}$g.

For investigating the granular cooling, it is crucial to have good microgravity quality. This is because remaining accelerations can have a dom-

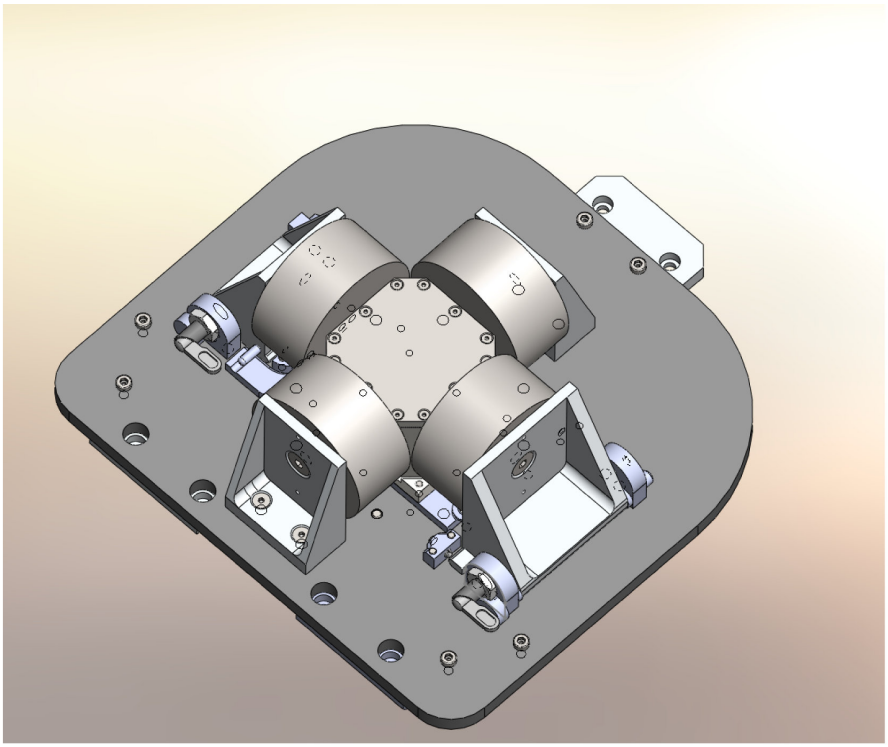

Figure 5.1: CAD drawing of the MEGraMa sample cell. The sample cell is surrounded by four electromagnets, which can be switched on and off individually in order to excite the paramagnetic particles inside the sample cell. This setup is used both in parabolic flight and in drop tower experiments.

inating influence especially on slow particles. For instance, it only takes $\sqrt{\frac{2*0.05\text{m}}{0.5\frac{\text{m}}{\text{s}^2}}} \approx 0.45\text{s}$ for a particle to be moved from one side of the sample cell to the other, if it is accelerated by $0.5\frac{\text{m}}{\text{s}^2}$.

This means, that everything which happens on significantly longer time scales (e.g. granular cooling), is distorted by remaining accelerations in a parabolic flight. However, for remaining accelerations of 10^{-4}g, this time scale amounts to $\sqrt{\frac{2*0.05\text{m}}{0.0001\frac{\text{m}}{\text{s}^2}}} \approx 32\text{s}$, which is larger than the entire drop tower measurement time of $\sim 10\text{s}$.

Therefore, the drop tower data is much more suitable for a quantitive analysis. Consequently, in this thesis a quantitative analysis of the data of a MEGraMa experiment on a drop tower is performed.

5.2 Image Processing

In the MEGraMa drop-tower experiment, spherical mu-metal[1] particles with diameters $d = 0.9\text{mm}$ are agitated magnetically and filmed by a high-speed camera with a resolution of $512 \times 512\text{px}^2$ and a framerate of 500fps (cf. fig. 5.2).

In order to obtain the 2D-projections of particle velocities from the recorded videos, first the particle positions have to be detected. For this, an image processing software is programmed. This software obtains the particle positions from the original greyscale images by performing the following steps:

- The image is binarized by setting all pixels with greylevels below a certain treshold to 1 and all pixels above that threshold to 0.
- As long as the number of pixels with value 1 is greater than zero, the following loop is performed:
  - The image is eroded [14] by a matrix $\begin{pmatrix} 0 & 1 & 0 \\ 1 & 1 & 1 \\ 0 & 1 & 0 \end{pmatrix}$. In other words, all pixels which are adjacent to a pixel with value 0 are also set to 0.

[1] The mu-metal consists of 77% nickel, 14% iron, 5% copper and 4% molybdenum.

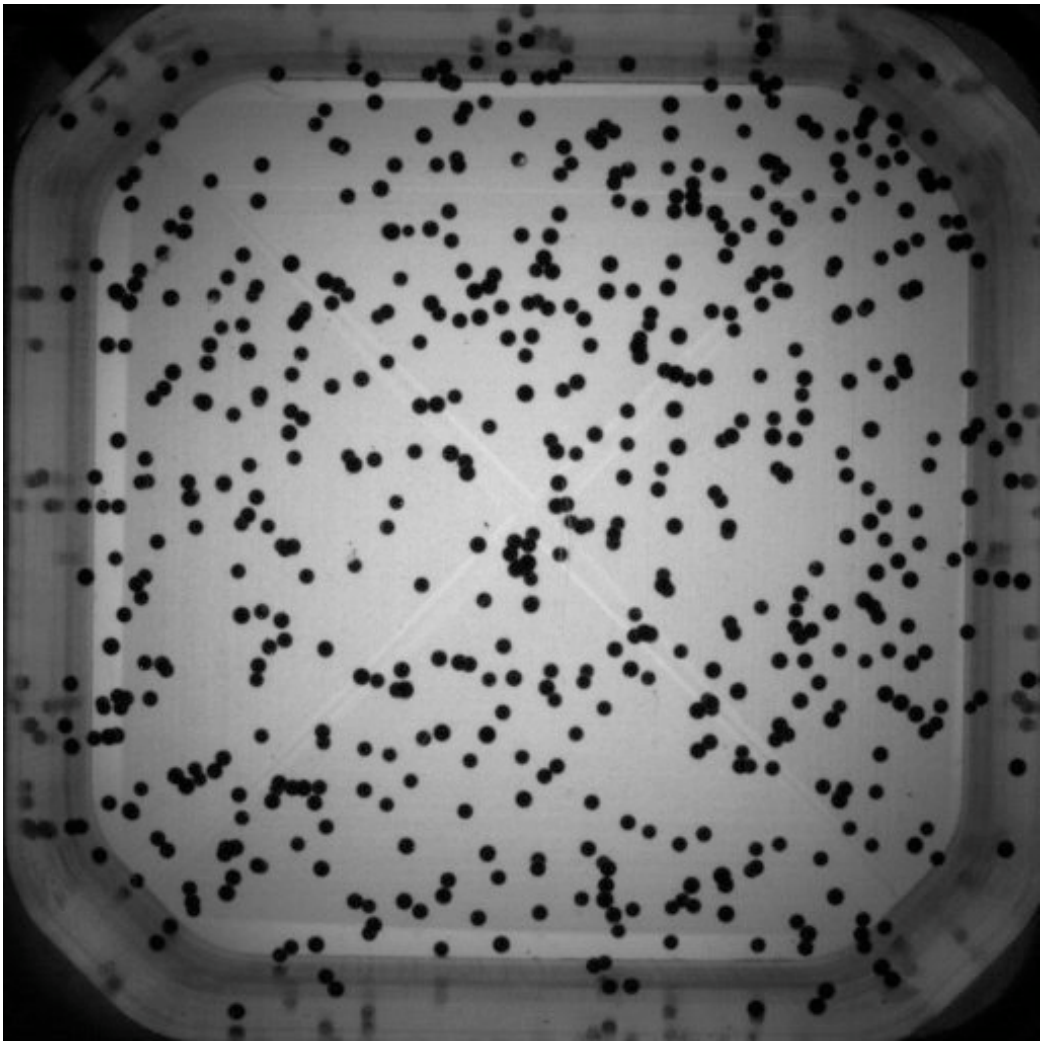

Figure 5.2: View into the sample cell during a drop tower experiment on granular cooling. It shows a granular gas after magnetic excitation and is taken from a video, which is recorded by a high-speed camera during the experiment and later used as input for the image processing algorithm described in section 5.2.

  - The image now consists of various disconnected regions of pixels with value 1. For each of those regions a maximum radius is defined by the distance between the average position of all pixels within that region and the position of the outermost pixel of the region.
  - If the maximum radius is smaller than or equal to a parameter *mr*, a particle is found, its position is stored, and all pixels of the according region are set to zero.

- When all pixels eventually are set to zero, the loop terminates and the particle finding algorithm is completed.

After the positions of particles in the individual frames are obtained, they have to be put together to actual trajectories of individual particles. Because all particles look the same in the camera images, it is not possible to identify a particular particle only by processing individual images. However, the particles usually do not move very much from frame to frame. Therefore, it is possible to follow individual particles from frame to frame and, by this, to obtain the trajectories of such particles.

Two particle positions obtained from two subsequent frames are considered to represent the same particle if their distance is smaller or equal than a parameter *md*. In order to exclude image processing errors, all particles which can not be tracked over at least $dt + 1$ subsequent frames, are neglected. The components $v_x(t)$ and $v_y(t)$ of the velocity vectors of the tracked particles can then be calculated as:

$$v_x(t) = \frac{x_{t+\lfloor dt \rfloor} - x_{t-\lfloor dt \rfloor}}{dt}$$

$$v_y(t) = \frac{y_{t+\lfloor dt \rfloor} - y_{t-\lfloor dt \rfloor}}{dt}$$

From those velocities, time dependent 2D velocity distributions and mean velocities can be calculated.

The tuning parameters of the particle tracking programm are set to $mr = 3$, $md = 4$ and $dt = 10$.

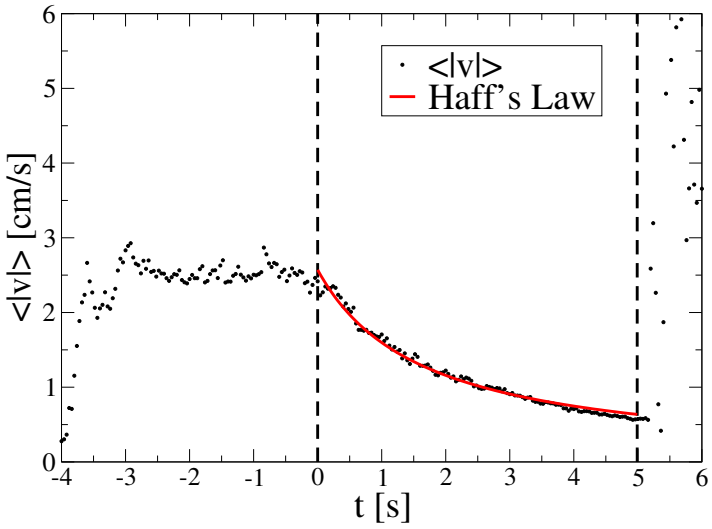

Figure 5.3: Drop tower data for a system of 605 annealed mumetal spheres. The system is excited by sequences of applying a magnetic field for 20ms and waiting for 80ms.

5.3 Results and Discussion

5.3.1 Evolution of Mean Velocities

Several drop tower measurements for different particle numbers and different kinds of particles and driving sequences are analysed. The particle number varies between 605 and 1219 spheres with $d = 0.9$mm, while the sample cell has always the dimension $50x50x50\text{mm}^3$. In some runs, annealed paramagnetic particles are used, while in other runs the particles are not annealed. Annealing the particles is a way to achieve a stronger magnetic susceptibility of the paramagnetic alloy. In addition, also different protocols of magnetic excitation are tried in the drop tower experiment.

The protocols used are listed as follows:

1. Two opposing magnets are switched on for 20ms. Then all magnets are switched off for 80ms. After that, the other two magnets are switched on for 20ms and finally, all magnets are switched off for 80ms again. This is repeated several time.

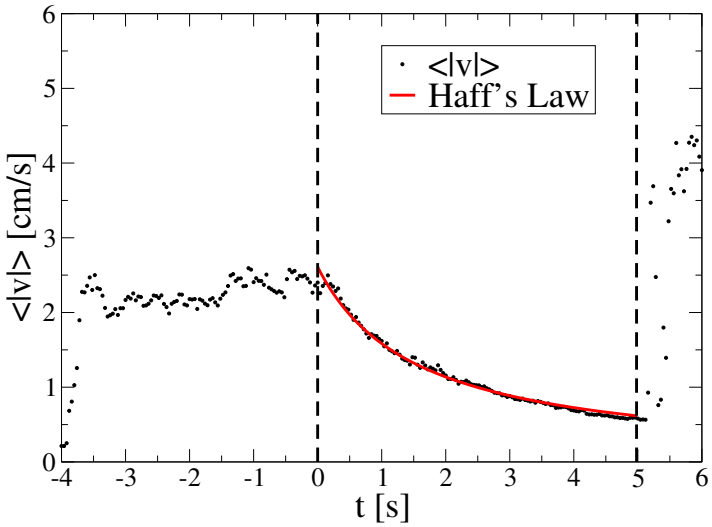

Figure 5.4: Drop tower data for a system of 607 unannealed mumetal spheres. The system is excited by sequences of applying a magnetic field for 20ms and waiting for 80ms.

2. Similiar to protocol **1**, but the magnets are switched on for 50ms and also switched off for 50ms.

3. Similiar to protocol **1** and **2**, but the magnets are switched on for 50ms and switched off for 150ms.

For each measurement, the 2D-velocities obtained by image processing are averaged over sets of 20 frames each and the resulting mean velocities are plotted as a function of time. The time at which the magnetig excitation is finished and the time of the impact are obtained from the log of the drop tower experiments. Haff's law

$$< |v(t)| >= \frac{v_0}{1 + \frac{t}{\tau_H}} \tag{5.1}$$

is fitted to the data which is obtained between switching of the magnetic excitation and the end of the microgravity phase (impact). The fitting parameters are the mean initial velocity v_0 and the Haff-time τ_H. The results of fitting Haff's Law to the experimental data are given in the table 5.1.

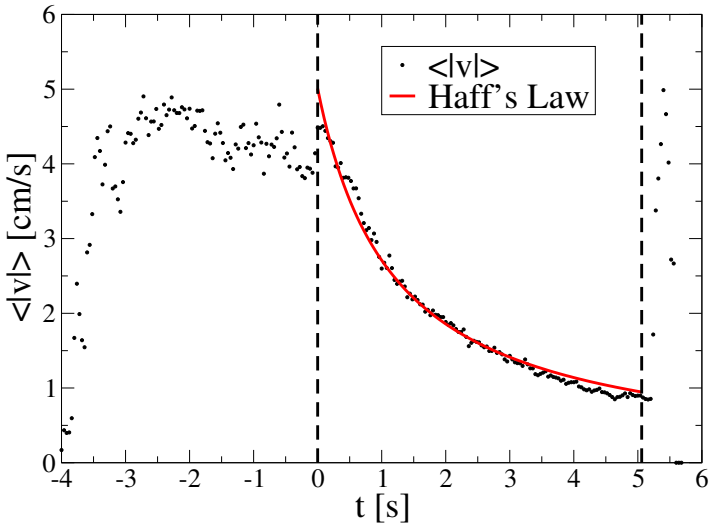

Figure 5.5: Drop tower data for a system of 607 unannealed mumetal spheres. The system is excited by sequences of applying a magnetic field for 50ms and waiting for 150ms.

N	φ	annealed	driving protocol	v_0	τ_H
605	0.185%	yes	**1**	$2.57\frac{\text{cm}}{\text{s}}$	1.64s
607	0.185%	no	**1**	$2.61\frac{\text{cm}}{\text{s}}$	1.55s
607	0.185%	no	**3**	$5.01\frac{\text{cm}}{\text{s}}$	1.18s
800	0.244%	yes	**1**	$2.67\frac{\text{cm}}{\text{s}}$	1.38s
1000	0.305%	yes	**1**	$2.45\frac{\text{cm}}{\text{s}}$	1.34s
1219	0.372%	no	**2**	$4.54\frac{\text{cm}}{\text{s}}$	1.56s

Table 5.1: Parameters used to fit Haff's law $< |v(t)| >= \frac{v_0}{1+\frac{t}{\tau_H}}$ to the measured velocities of a 3D granular gas with particle numbers N, and, accordingly, different densities φ.

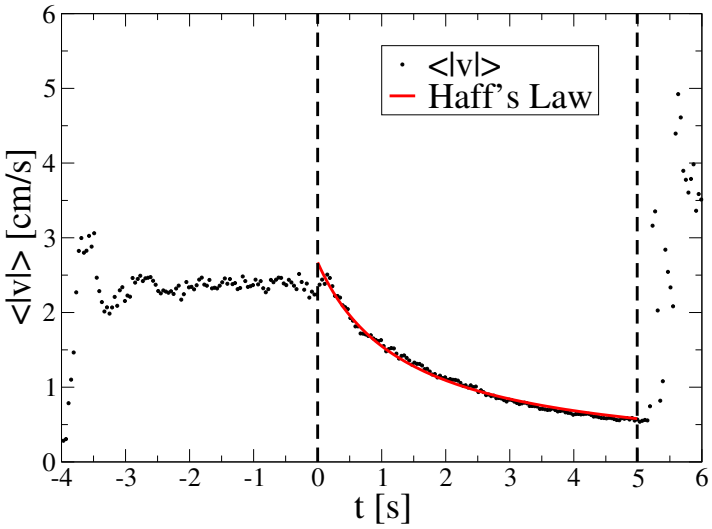

Figure 5.6: Drop tower data for a system of 800 annealed mumetal spheres. The system is excited by sequences of applying a magnetic field for 20ms and waiting for 80ms.

The Haff time τ_H and the initial velocity v_0 are related to the number density n, the particle cross section σ and the coefficient of restitution ϵ of the particles by equation (1.20):

$$\tau_H = \frac{2}{v_0(1-\epsilon^2)n\sigma} \tag{5.2}$$

n and σ can be expressed in terms of the particle radius r and the packing fraction φ as:

$$n = \frac{\varphi}{\frac{4}{3}\pi r^3} \tag{5.3}$$

and

$$\sigma = \pi r^2 \tag{5.4}$$

This allows to write

$$n\sigma = \frac{3\varphi}{4r} \tag{5.5}$$

Therefore, equation (5.2) can be written as:

$$\tau_H = \frac{8r}{3v_0(1-\epsilon^2)\varphi} \tag{5.6}$$

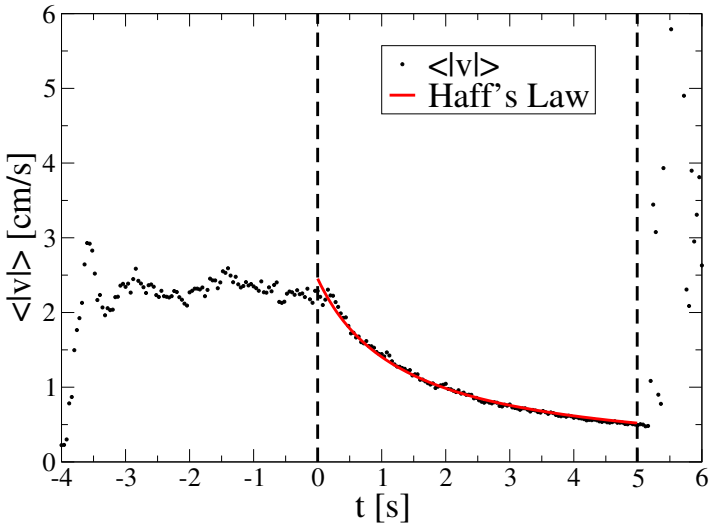

Figure 5.7: Drop tower data for a system of 1000 annealed mumetal spheres. The system is excited by sequences of applying a magnetic field for 20ms and waiting for 80ms.

This can finally be transformed to

$$\frac{1}{\tau_H v_0} = \frac{3(1-\epsilon^2)}{8r}\varphi \tag{5.7}$$

Because the numbers $\epsilon \approx 0.3$ and $r = 0.00045m$ are the same for all drop tower runs, one would expect to find a linear dependence of $\frac{1}{\tau_H v_0}$ on the packing fraction φ with offset 0. In order to check this assumption, the measured data is plotted in figure 5.9.

The plotted data does not show a linear relationship with offset 0. In addition, the values of $\frac{1}{\tau_H v_0}$ seem to depend on the used protocol of magnetic excitation. For instance, while the two measurements for protocol 1 at $\varphi \approx 0.0019$ lead to quite similiar results, the measurement for the same density using protocol 3 deviates by more than 30%. Also, the data point measured using protocol 2 is not consistent with the other data points, because it shows a much smaller value for $\frac{1}{\tau_H v_0}$ than the other data points even though it is measured at a comparably high density.

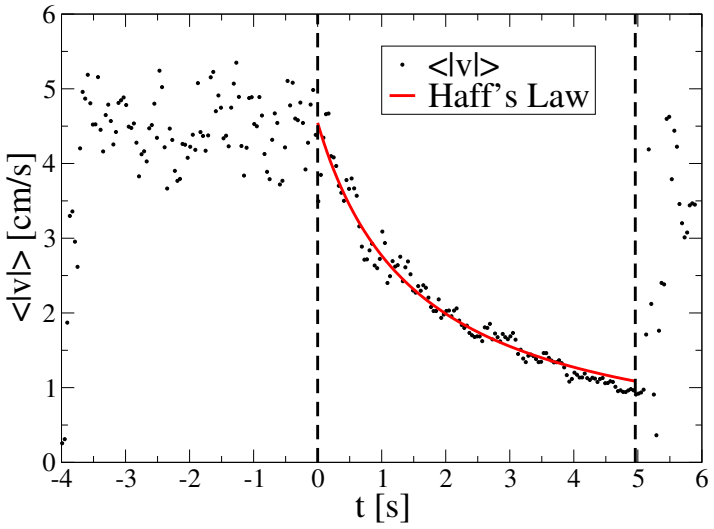

Figure 5.8: Drop tower data for a system of 1219 unannealed mumetal spheres. The system is excited by sequences of applying a magnetic field for 50ms and waiting for 50ms.

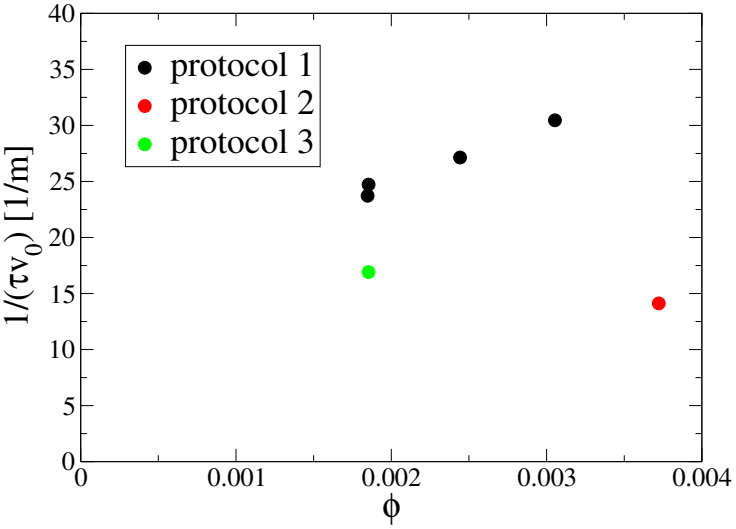

Figure 5.9: $\frac{1}{\tau_H v_0}$ as a function of the packing fraction φ for drop tower results. The different shaking protocols are indicated by different colors.

Therefore, it makes sense to neglect the data points for protocol 2 and 3 for the time being and to focus on the data points for protocol 1 instead. A linear function of the form

$$\frac{1}{\tau_H v_0} = m\varphi + b \tag{5.8}$$

can be fitted to those data points as shown in figure 5.10. This fit yields a slope of $m = 5165.2\frac{1}{m}$ and an offset of $b = 14.634\frac{1}{m}$. This offset might be caused by a finite size effect of the system: While the number of particle-particle collisions approaches 0 for $\varphi \to 0$, the number of particle-wall collisions per particle and travelled length has to stay finite. In addition, this number should be independent of φ for small packing fractions $\varphi \ll 1$. Therefore, the finite size of the system leads to an offset of the number of collisions per particle and travelled length. Because this number has to be proportional to $\frac{1}{\tau_H v_0}$, this consequently leads to an offset in the quantity $\frac{1}{\tau_H v_0}$. Therefore, equation (5.7) can be rewritten as

$$\frac{1}{\tau_H v_0} = \frac{3(1-\epsilon^2)}{8r}\varphi + b \tag{5.9}$$

and the slope m can be expressed in terms of the coefficient of restitution ϵ and the particle radius r:

$$\frac{3(1-\epsilon^2)}{8r} \stackrel{!}{=} m = 5165.2\frac{1}{\mathrm{m}} \tag{5.10}$$

However, inserting $\epsilon \approx 0.3$ and $r = 0.00045$m leads to a slope of $\approx 758\frac{1}{\mathrm{m}}$, which is about an order of magnitude smaller than the slope obtained from the data.

The values for ϵ and r are determined relatively precisely, which means, that they can not possibly cause such a big deviation between the expected and the actual slope. However, the particles are only driven by the magnets in x and y-direction. This means, that even though the distribution of granular particles in the x-y-plane seems rather homogenous for most measurements, it might be quite inhomogenous in the z-direction. For instance, the majority of the particles could stay within a rather thin layer during the whole experiment. Because the camera observing the experiment is pointing in z-direction, it can only record x-y-projections of the system. This means, that possible inhomogeneities in z-direction are hard to detect.

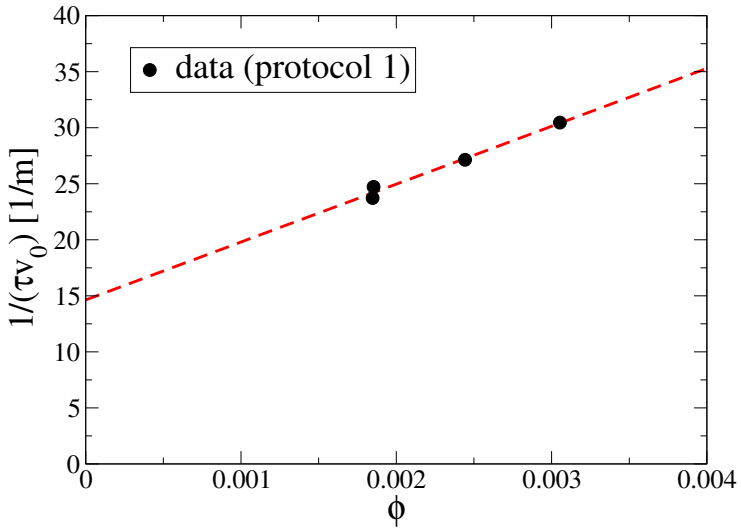

Figure 5.10: $\frac{1}{\tau_H v_0}$ as a function of the packing fraction φ for drop tower results for magnetic shaking by protocol 1. A linear fit is performed and yields a slope of $5165.2\frac{1}{m}$ and an offset of $14.634\frac{1}{m}$.

If, for instance, the vast majority of particles would stay within a subvolume V' of the sample cell volume V during the whole measurement, the effective packing fraction φ' for this subvolume would be given as

$$\varphi' = \frac{V}{V'}\varphi \tag{5.11}$$

With the definition of a factor $\beta := \frac{V'}{V}$, which equals 1 for a homogenous system and becomes smaller than 1 for an inhomgenous system, one can also write:

$$\varphi' = \frac{1}{\beta}\varphi \tag{5.12}$$

Because the dynamics of the system is governed by the effective packing fraction φ', φ' is also the relevant quantity which goes into equation (5.7):

$$\frac{1}{\tau_H v_0} = \frac{3(1-\epsilon^2)}{8r}\varphi' \tag{5.13}$$

However, because only the system-wide packing fraction φ can be determined for the drop tower experiment, it is more convenient to write:

$$\frac{1}{\tau_H v_0} = \frac{3(1-\epsilon^2)}{8r\beta}\varphi \tag{5.14}$$

The slope from this equation can then be compared to the measured slope m:

$$m = \frac{3(1-\epsilon^2)}{8r\beta} \tag{5.15}$$

Because $\epsilon \approx 0.3$ and $r = 0.00045$m are known, the factor β for the measurements performed with magnetic excitation protocol 1 can be determined as:

$$\beta = \frac{3(1-\epsilon^2)}{8rm} = \frac{3(1-\epsilon^2)}{8r * 5165.2\frac{1}{\mathrm{m}}} \approx 0.147 \tag{5.16}$$

This means, that the particles effectively only use about 15% of the maximum sample cell volume. However, the validity of this assumption can not be further investigated with the experimental setup from the drop tower experiment: In order to obtain a 3D-density distribution of the investigated granular gas, e.g. a second camera perpendicular to the current camera would be needed.

5.3.2 Velocity Distributions

For understanding the particle dynamics in cooling granular systems, the evolution of the velocity distribution might be relevant. For instance, it is an interesting question if the velocities follow a Maxwell-Boltzmann distribution or not [29].

If the individual components of velocity vectors

1. follow a Gaussian distribution with mean zero and the same standard deviation for each spatial dimension and

2. there is no correlation between the components v_x, v_y and v_z,

the absolute values of velocity vectors are Maxwell-Boltzmann distributed. For a gas in thermal equilibrium, the particle velocities follow a Maxwell-Boltzmann distribution. However, for a granular gas this is not necessarily

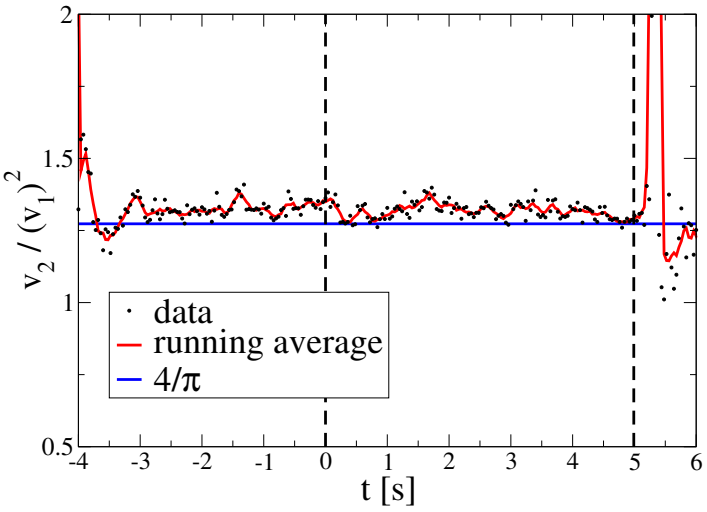

Figure 5.11: Coefficient of momenta $\frac{v_2}{v_1^2}$ for drop tower data for a system of 605 annealed mumetal spheres. The system is excited by sequences of applying a magnetic field for 20ms and waiting for 80ms. The red line represents a running average averaging over 5 data points.

true, because particles undergo dissipative collisions and therefore a granular gas can not be in thermal equilibrium.

In the drop tower experiment, the particle velocities are obtained from a 2D-projection. Therefore, the absolute value v of a 2D velocity vector $\vec{v}$ is given by the x- and y-components v_x and v_y of the velocity by

$$v = \sqrt{v_x^2 + v_y^2} \tag{5.17}$$

The z-component v_z can not be observed and therefore does not contribute to the measured velocity vectors.

Now the properties of a potential 2D-Maxwell Boltzmann distribution have to be derived in order to be compared to the data obtained from the drop tower experiment. First, Gaussian distributions $p(v_{x,y})$ are assumed for the individual components of the velocity vector:

$$p(v_x) = \frac{1}{\sigma\sqrt{2\pi}} \exp(-\frac{1}{2}\frac{v_x^2}{\sigma^2}) \tag{5.18}$$

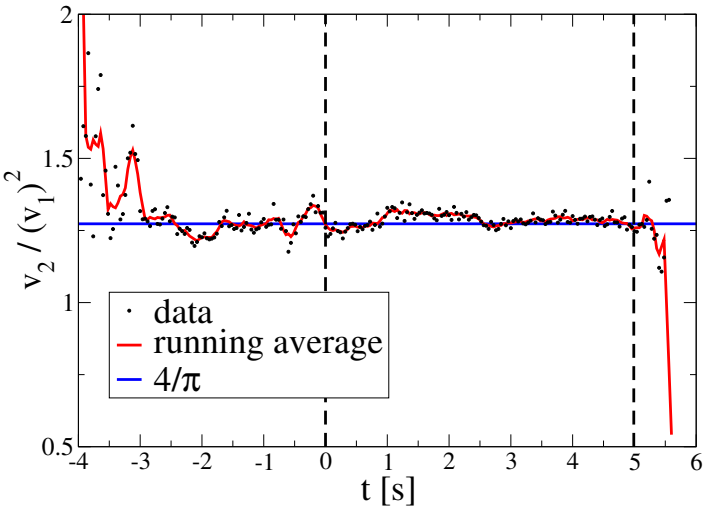

Figure 5.12: Coefficient of momenta $\frac{v_2}{v_1^2}$ for drop tower data for a system of 607 unannealed mumetal spheres. The system is excited by sequences of applying a magnetic field for 50ms and waiting for 150ms. The red line represents a running average averaging over 5 data points.

$$p(v_y) = \frac{1}{\sigma\sqrt{2\pi}}\exp(-\frac{1}{2}\frac{\mathrm{v_y^2}}{\sigma^2}) \tag{5.19}$$

The probability $p(v)$ for the 2D-vector having an absolute value of v can now written in using cylindrical coordinates as follows:

$$p_{MB}(v) = \int_0^{2\pi} d\theta p(v\cos\theta)p(v\sin\theta)v \tag{5.20}$$

Using the definition of $p(v_{x,y})$, this gives:

$$p_{MB}(v) = \int_0^{2\pi} d\theta \frac{1}{2\pi\sigma^2}\exp(-\frac{1}{2}\frac{(\mathrm{v}\cos\theta)^2}{\sigma^2})\exp(-\frac{1}{2}\frac{(\mathrm{v}\sin\theta)^2}{\sigma^2})\mathrm{v} \tag{5.21}$$

With $v^2 = v_x^2 + v_y^2$ and $\cos^2\theta + \sin^2\theta = 1$, one can combine the two exponentials, which leads to:

$$p_{MB}(v) = \frac{1}{2\pi\sigma^2}\int_0^{2\pi} d\theta\exp(-\frac{1}{2}\frac{\mathrm{v}^2}{\sigma^2})\mathrm{v} \tag{5.22}$$

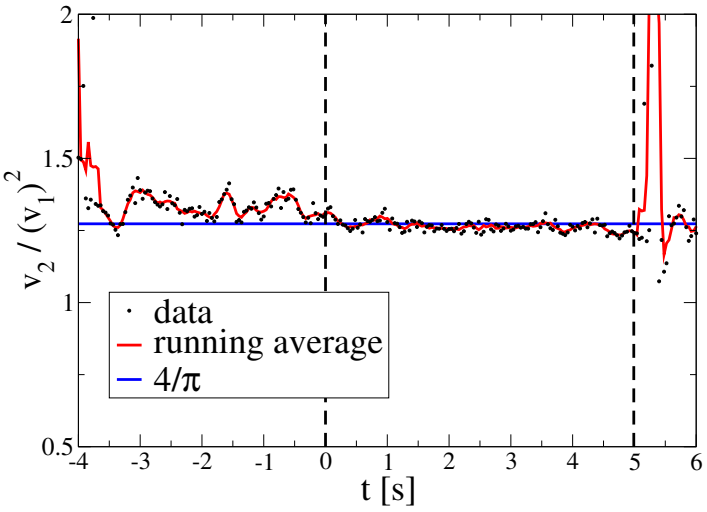

Figure 5.13: Coefficient of momenta $\frac{v_2}{v_1^2}$ for drop tower data for a system of 607 unannealed mumetal spheres. The system is excited by sequences of applying a magnetic field for 20ms and waiting for 80ms. The red line represents a running average averaging over 5 data points.

The above integration yields the 2D-Maxwell Boltzmann distribution as:

$$p_{MB}(v) = \frac{1}{\sigma^2} v \exp(-\frac{1}{2}\frac{v^2}{\sigma^2}) \tag{5.23}$$

Now the first moment of the 2D-Maxwell Boltzmann distribution can be calculated as:

$$v_1 = \int_0^\infty dv \frac{1}{\sigma^2} v^2 \exp(-\frac{1}{2}\frac{v^2}{\sigma^2}) \tag{5.24}$$

Partial integration leads to:

$$v_1 = -[v \exp(-\frac{1}{2}\frac{v^2}{\sigma^2})]_0^\infty + \int_0^\infty dv \exp(-\frac{1}{2}\frac{v^2}{\sigma^2}) \tag{5.25}$$

The first summand is zero and the second summand is proportional to the integral of the normal distribution. Therefore, v_1 can be calculated as:

$$v_1 = \int_0^\infty dv \exp(-\frac{1}{2}\frac{v^2}{\sigma^2}) = \frac{1}{2}\int_{-\infty}^\infty dv \exp(-\frac{1}{2}\frac{v^2}{\sigma^2}) = \frac{\sigma\sqrt{2\pi}}{2} = \sigma\sqrt{\frac{\pi}{2}} \tag{5.26}$$

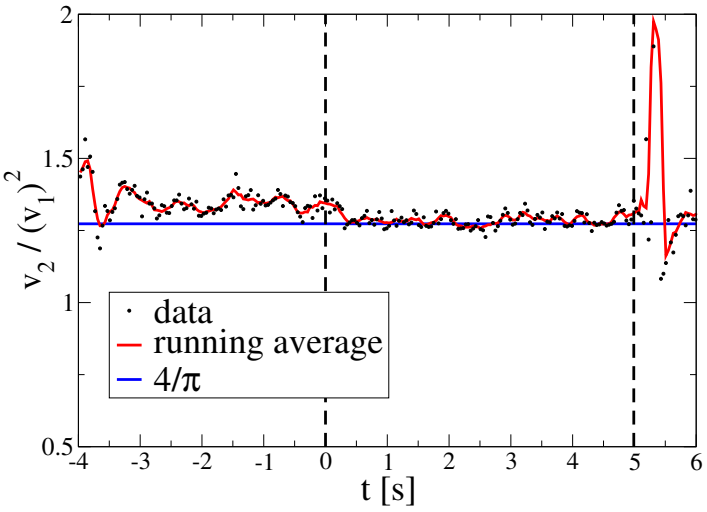

Figure 5.14: Coefficient of momenta $\frac{v_2}{v_1^2}$ for drop tower data for a system of 800 annealed mumetal spheres. The system is excited by sequences of applying a magnetic field for 20ms and waiting for 80ms. The red line represents a running average averaging over 5 data points.

Similiarly, the second moment v_2 can be calculated as

$$v_2 = \int_0^\infty dv \frac{1}{\sigma^2} v^3 \exp(-\frac{1}{2}\frac{v^2}{\sigma^2}) \tag{5.27}$$

Partial integration leads to:

$$v_2 = [-v^2 \exp(-\frac{1}{2}\frac{v^2}{\sigma^2}]_0^\infty + \int_0^\infty dv 2v \exp(-\frac{1}{2}\frac{v^2}{\sigma^2}) \tag{5.28}$$

The first summand equals zero. The second summand can be rewritten with the substitution $u = v^2$ as:

$$v_2 = \int_0^\infty du \exp(-\frac{u}{2\sigma^2}) \tag{5.29}$$

This integral can be solved as:

$$v_2 = [-2\sigma^2 \exp(-\frac{u}{2\sigma^2})]_0^\infty = 2\sigma^2 \tag{5.30}$$

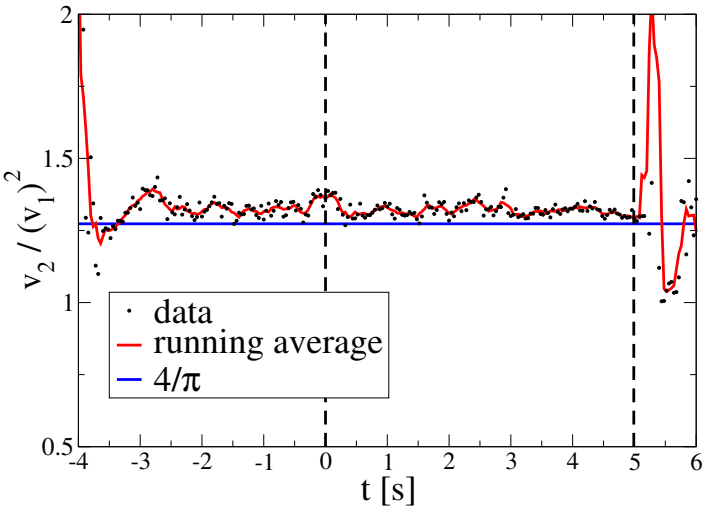

Figure 5.15: Coefficient of momenta $\frac{v_2}{v_1^2}$ for drop tower data for a system of 1000 annealed mumetal spheres. The system is excited by sequences of applying a magnetic field for 20ms and waiting for 80ms. The red line represents a running average averaging over 5 data points.

The moments v_1 and v_2 can be obtained from the measured absolute particle velocities v as

$$v_1 =< v > \tag{5.31}$$

and

$$v_2 =< v^2 > \tag{5.32}$$

The averaging is performed for sets of 20 frames each, which means that all velocities obtained from a set of 20 frames or 40ms contribute to the same data point for v_1 and v_2. Then for every data set the coefficient

$$\frac{v_2}{v_1^2}$$

is calculated and plotted as a function of time (cf. fig. 5.11, 5.12, 5.13, 5.14, 5.15, and 5.16). The measured coefficient can be compared to the according value for a Maxwell-Boltzmann velocity distribution, which is:

$$\frac{v_2}{v_1^2} = \frac{2\sigma^2}{(\sigma\sqrt{\frac{\pi}{2}})^2} = \frac{4}{\pi} \tag{5.33}$$

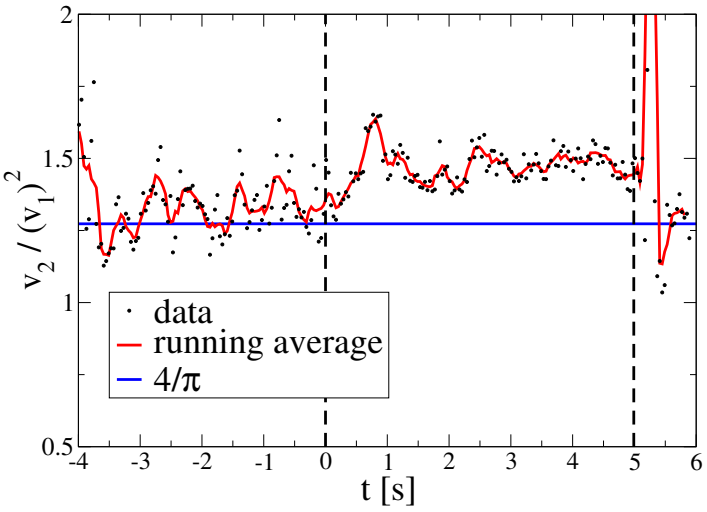

Figure 5.16: Coefficient of momenta $\frac{v_2}{v_1^2}$ for drop tower data for a system of 1219 unannealed mumetal spheres. The system is excited by sequences of applying a magnetic field for 50ms and waiting for 50ms. The red line represents a running average averaging over 5 data points.

The plots show, that the coefficient of momenta $\frac{v_2}{v_1^2}$ is in general consistent to a Maxwell-Boltzmann distribution during cooling for most drop tower measurements.

However, at the beginning and the end of the experiment, strong deviations from the Maxwell-Boltzmann distribution can be seen: The sample cell is catapulted upwards at the beginning of an experiment and hits the bottom of the drop tower again at the end of an experiment. Therefore, the system undergoes strong accelerations at those times and the particle dynamics are always completely governed by those accelerations.

After the catapulting phase, the coefficient $\frac{v_2}{v_1^2}$ approaches the Maxwell-Boltzmann value of $\frac{4}{\pi}$ quickly already during the magnetic excitation phase. However, the measured coefficient $\frac{v_2}{v_1^2}$ fluctuates significantly around $\frac{4}{\pi}$. Also, in some cases (cf. fig. 5.11 and fig. 5.15) it seems to stay slightly above that value. Therefore, a non-Maxwellian distribution can not be outruled completely. In addition, there is also a possibility, that the velocity

distribution is consistent to a Maxwell-Boltzmann distribution in the first two moments, but not in its higher moments. However, for investigating higher moments and for making more significant statements about the behavior of the first two moments, experiments with higher particle numbers (and therefore better statistics) would be useful.

Different from the other drop tower experiments, the run with 1219 unannealed particles shows strong deviations from Maxwell-Boltzmann over the whole measurement time: During the magnetic excitation, the coefficient $\frac{v_2}{v_1^2}$ fluctuates wildly around $\frac{4}{\pi}$. During the cooling period, it converges to a value around $\frac{3}{2}$, which is clearly different from $\frac{4}{\pi}$. When looking at the original videos, it turns out that the magnetic excitation is not able to produce homogenous $x-y-$distributions of particles for higher particle numbers. The magnetic excitation produces homogenous $x-y-$distributions in the experiments with ~ 600 and ~ 800 particles. But for the experiments with 1000 and 1219 particles the distribution becomes increasingly inhomogenous, e.g. the particles tend to cluster. This behavior seems to be caused by the paramagnetic properties of the particles, because it appears already before the granular cooling happens. For the run with 1219 particles, the clustering of the particles seems to be strong enough to change the velocity distribution significantly: While most particles stick together and only move slowly, some particles can move around without participating in clustering and therefore move much faster. This leads to a high-velocity tail of the velocity distribution which is indicated by a $\frac{v_2}{v_1^2} > \frac{4}{\pi}$.

The clustering of particles might also explain the fact, that the data point for 1219 particles ($\varphi \approx 0.0037$) deviates significantly from all other data points in figure 5.9. The quantity $\frac{1}{\tau_H v_0}$, which is proportional to the number of collisions per travelled distance, is influenced strongly by the spatial distribution of particles. However, the temporal evolution of the mean absolute velocity $< v >$ is still consistent with Haff's Law in this measurement (cf. fig. 5.8), even though the velocity distribution is quite different from the other measurements.

5.4 Conclusion

From the analysis of the described drop tower experiment, the following conclusions can be made:

- Haff's Law $< v(t) >= \frac{v_0}{1+\frac{t}{\tau_H}}$ describes the temporal evolution of mean absolute velocities in a cooling granular gas very well.
- The obtained Haff times τ_H differ from the values one would expect for a completely homogenous system with given v_0, n, σ and ϵ. This is most likely due to inhomogenous spatial distributions of particles, which are caused by an effectively 2D-excitation mechanism. The assumption that the deviations from the expected values are caused by the excitation mechanism is supported by the fact, that the results are consistent between different measurements with the same shaking mechanism.
- The influence of system walls can be clearly seen. However, it is also shown by the data, that particle-particle collisions play a significant role in the drop tower experiment.
- For granular gases without strong clustering, the measured velocity distributions are consistent with Maxwell-Boltzmann. However, even for clearly non-Maxwellian velocity distributions, the time evolution of mean absolute velocities still follows $< v(t) >= \frac{v_0}{1+\frac{t}{\tau_H}}$. This means, that the validity of Haff's Law does not depend on a specific velocity distribution.
- The current excitation mechanism is only able to produce non-clustered granular gases at very low densities ($\varphi < 0.3\%$). An optimized driving mechanism, which produces non-clustered granular gases also at higher densities, would not only increase the accessible parameter space, but also allow for higher particle numbers and therefore better statistics. Also, it would make sense to add magnets in the z-direction in order to achieve a homogenous spatial distribution of particles.

Chapter 6

Outlook

In this thesis, granular dynamics have been investigated in a Lorentz model, for a 2D dense granular fluid, and for a 3D granular gas. In all three experiments, results beyond literature could be obtained. However, the analysis of the experimental results also points out possible future improvements.

The dynamics of a single sphere within a Lorentz model has been investigated. The localization transition was observed and exponents of the subdiffusive dynamics were obtained. The results proved to be consistent with simulation results. For following the long-time dynamics of the system, a larger experimental area would be needed. Also, the experimental results show a need for better statistics, which could be achieved by averaging over different sample plates with randomly distributed obstacles. In addition, experiments with more than one sample particle at a time or with self-propelled particles (cf. sect. A.2) are conceivable.

In 2D dense granular fluids, the onset of glassy dynamics has been observed. A plateau over more than four decades in time was found at a density of $\varphi = 0.76$. Exponents of the mean-squared displacements for intermediate and for long times have been obtained for different densities and the scaling properties of the mean-squared displacement have been investigated. For future experiments, a larger system size would be useful in order to diminish the influence of finite size effects and to increase statistics. Also, introducing rough system boundaries could prevent the collective angular motion at higher densities. Another extension would be the behavior of a pulled test particle in a dense granular fluid [11, 12, 13]. In addition, 2D fluids of self-propelled particles [35] could be investigated.

The cooling of 3D granular gases was investigated and Haff's Law was verified. It was shown that the velocity distribution does not change significantly during granular cooling. For future microgravity experiments on granular cooling, it would be interesting to go to higher densities. Also, the magnetic driving of particles could be improved in order to provide more homogenous spatial distributions of particles at the beginning of the cooling process. In addition, measuring with more than one camera would allow to obtain 3D particle positions.

Appendix A

A.1 Haff's Law for a Single Particle in 1D

A simple example of dissipative dynamics is a particle oscillating between two walls in one dimension. At each wall, the particle undergoes an inelastic collision with a coefficient of restitution $\epsilon < 1$ and is reflected back towards the opposite wall. The time-dependence of the particle velocity $v(t)$ can be calculated as follows.

The particle starts at time $t_0 = 0$ at one side of the system with an initial velocity v_0. After travelling by the system size L, which takes a time $t_1 = \frac{L}{v_0}$, it hits the opposite wall and is reflected back. It then has a new velocity $v_1 = v_0\epsilon$. Consequently, the particle veloctiy v_n after n collisions is:

$$v_n = \epsilon^n v_0 \tag{A.1}$$

The time t_n of the n-th collision can then be calculated as:

$$t_n = \sum_{i=0}^{n-1} \frac{L}{v_i} = \sum_{i=0}^{n-1} \frac{L}{v_0\epsilon^i} = \frac{L}{v_0}\frac{1-\epsilon^{-n}}{1-\epsilon^{-1}} = \frac{L}{v_0}\frac{\epsilon^n - 1}{\epsilon^{n-1}(\epsilon - 1)} \tag{A.2}$$

The function

$$v(t) = \frac{v_0}{1 + \frac{t}{\tau_H}} \tag{A.3}$$

with

$$\tau_H = \frac{L}{v_0}\frac{\epsilon}{1-\epsilon} \tag{A.4}$$

yields the correct velocities $v_n(t_n)$ directly after the collisions at the times t_n. This can be proven by inserting equation (A.2) into equation (A.3):

$$v(t_n) = \frac{v_0}{1 + \frac{t_n}{\tau_H}} = \frac{v_0}{1 + \frac{1-\epsilon}{\epsilon}\frac{\epsilon^n - 1}{\epsilon^{n-1}(\epsilon-1)}} = \frac{v_0}{1 - \frac{\epsilon^n - 1}{\epsilon^n}} = v_0\epsilon^n \tag{A.5}$$

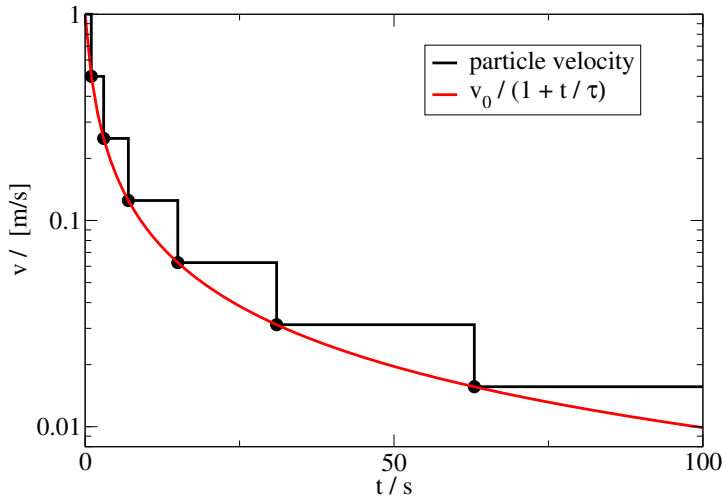

Figure A.1: Actual particle velocity (black) versus a Haff-like approximation $v(t) = \frac{v_0}{1+\frac{t}{\tau}}$ for the cooling behavior of a particle with initial velocity $v_0 = 1\frac{m}{s}$ between walls. Collisions are indicated by black dots.

The function $v(t)$ is very similiar to Haff's Law (1.5). Different from the actual velocity of the particle in the described experiment, $v(t)$ is a continous function. However, it matches the actual particle velocity at the collision times t_n and therefore is a good approximation of the actual particle velocity. Both the actual particle velocity and the Haff-like velocity function v(t) are shown in figure A.1 for an initial velocity $v_0 = 1$ms, a wall distance $L = 1$m and a coefficient of restitution $\epsilon = 0.5$.

A.2 Self-Propelled Particles

Self-propelled particles [34] are particles which are able to perform a directed motion. This can be achieved by driving each particle individually, e.g. by a small motor. A more efficient way is to use an external energy sorce for driving the particles, for instance a vibrating surface [36].

In order to transform vertical vibrations into a directed horizontal movement, particles with an asymetric mass distribution are used. If one side of the particle has a lower mass than the other, the side with the lower mass responds stronger to the vertical vibrations than the heavier side of

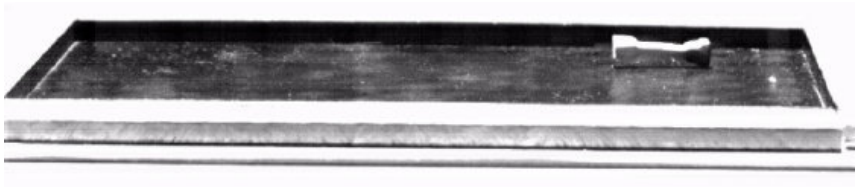

Figure A.2: Self-propelled particle with a length of 40mm on a vertically vibrated surface. The particle moves from right to left.

the particle. This means, the movement of the particle becomes asymetric.

The resulting horizontal motion depends on the shape and material of the particle and on the driving frequency. The dynamic behavior of different particles is tested experimentally and several possible designs of self-propelled particles are found.

An example of a self-propelled particle is shown in figure A.2. The particle consists of a metal screw, which is charged with two nuts on one side and put into a heat shrink tube. The asymetric mass distribution is provided by the screw and the nuts, while the heat shrink tube provides a smooth surface of the particle. The particle length is 40mm.

When driven by a vertical sine vibration with the frequency $f = 70\text{Hz}$ and the peak acceleration $a = 2.5\text{g}$, this particle moves into the direction of its lighter side. This is because the lighter side jumps up and down by a significant distance and, by this, slowly pulls the heavier side of the particle in its direction.

Such particles can be used for future experiments on 2D fluids of self-propelled particles. Similiar, but smaller particles could also be used as test particles for the Lorentz model experiment.

A.3 Bibliography

[1] Jacques Duran, *Sands, Powders and Grains.* Springer-Verlag New York, 1997.

[2] James G. Berryman, *Physical Review A*, 27(2):1053-1061, 1983.

[3] J. D. Bernal, *Nature*, 185:68-70, 1960.

[4] Anuraag R. Kansal, Salvatore Torquato, and Frank H. Stillinger, *Physical Review E*, 66:041109, 2002.

[5] A. Anikeenko and N. Medvedev, *Physical Review Letters*, 98(23):235504, June 2007.

[6] S. Torquato, T. M. Truskett, and P. G. Debenedetti, *Physical Review Letters*, 84(10):2064-2067, March 2000.

[7] H. A. Lorentz, *KNAW Proceedings*, 7:438-453, 1905.

[8] Felix Höfling, Thomas Franosch, and Erwin Frey, *Physical Review Letters*, 96(16):165901, April 2006.

[9] T. Bauer, F. Höfling, T. Munk, E. Frey, and T. Franosch, *Eur. Phys. J. Special Topics*, 189:103-118, 2010.

[10] Luca Cipelletti, S. Manley, R. C. Ball, and D. A. Weitz, *Physical Review Letters*, 84(10):2275, 2000.

[11] I. Gazuz, A. M. Puertas, Th. Voigtmann, and M. Fuchs, *Physical Review Letters*, 102(24):248302, 2009.

[12] Andrea Fiege, Matthias Grob, Annette Zippelius, *Granular Matter*, 14:247-252, 2012.

[13] R. Chandelier, and O. Dauchot, *Pysical Review Letter*, 103(12):128001, 2009.

[14] Rafael C. Gonzales, Richard E. Woods, *Digital Image Processing, Second Edition.* Prentice Hall, New Jersey, 2002.

[15] C. A. Angell, *Science*, 267, 1995.

[16] P. N. Pusey and W. van Megen, *Nature*, 320(27):340-342, 1986.

[17] W. van Megen, P. N. Pusey, *Physical Review A*, 43(10):5429-5441, 1991.

[18] U. Bengtzelius, W. Götze, and A. Sjölander, *J. Phys. C: Solid State Phys.*,17:5915-5934, 1984.

[19] Franceso Sciortino. One liquid, two glasses, *Nature Materials*, 1:145-146, 2002.

[20] Wolfgang Götze, *Complex Dynamics of Glass-Forming Liquids.* Oxford University Press, 2009.

[21] W. Till Kranz, Matthias Sperl, and Annette Zippelius, *Physical Review Letters*, 104(22):225701, June 2010.

[22] Matthias Sperl, W. Till Kranz, and Annette Zippelius, *Europhysics Letters*, 98(2);28001, 2012.

[23] P. M. Reis, R. a. Ingale, and M. D. Shattuck, *Physical Review Letters*, 98(18):188301, May 2007.

[24] A. R. Abate and D. J. Durian, *Physical Review E*, 74(3):031308, 2006.

[25] W. Kob and H. C. Andersen, *Physical Review E*, 51:4626, 1995a.

[26] J. Baschnagel, C. Bennemann, W. Paul, and K. Binder, *J. Phys.: Condens. Matter*, 12:6365-6374, 2000.

[27] M. Bayer, J. M. Brader, F. Ebert, M. Fuchs, E. Lange, G. Maret, R. Schilling, M. Sperl, and J. P. Wittmer, *Physical Review E*, 76:011508, 2007.

[28] P. K. Haff, *J. Fluid Mech.*, 134:401-430, 1983.

[29] Hiizu Nakanishi, *Physical Review E*, 67(1):010301, 2003.

[30] C. C. Maass, N. Isert, G. Maret, and C. M. Aegerter, *Physical Review Letters*, 100(24):248001, June 2008.

[31] Isaac Goldhirsch. *Annual Review of Fluid Mechanics*, 35(1):267-293, January 2003.

[32] F. Lechenault and Karen E. Daniels, *Soft Matter*, 6(13):3074, 2010.

[33] Éric Falcon, Régis Wunenburger, Pierre Évesque, Stéphan Fauve, Carole Chabot, Yves Garrabos, and Daniel Bysens, *Physical Review Letters*, 83(2):440-443, 1999.

[34] S. Dorbolo, D. Volfson, L. Tsimring, and A. Kudrolli, *Physical Review Letters*, 95:044101, 2005.

[35] Arshad Kudrolli, Geoffroy Lumay, Dmitri Volfson, and Lev S. Tsimring, *Physical Review Letters*, 100(5):058001, 2008.

[36] Julien Deseigne, Sébastien Léonard, Olivier Dauchot, and Hugues Chaté, *Soft Matter*, 8(20), 5629-5639, 2012.

Acknowledgement

I thank Professor Jürgen Horbach and Professor Stefan Egelhaaf for supervising my thesis.

I want to thank Doctor Matthias Sperl for guiding me through my thesis and for many interesting scientific discussions. He also supported me with very helpfull ideas to improve my experiments.

Steffen Reinhold helped me greatly with assembling the dense granular fluids experiment. Anoosheh Yazdi answered some of my mode-coupling questions and helped me a lot by proofreading my thesis.

I also thank my colleagues Doktor Peidong Yu, Doktor Philip Born, Ting Wang and Jörg Bartnick for providing a nice work environment and joining me for coffee breaks.

Stefan Frank-Richter helped me with mechanical problems. Darren Flynn assisted me performing the Lorentz model experiment. Matthias Wiech supported me by testing self-propelled particles and Liam Redmond fixed a technical problem with my experimental equipment.

Finally I want to thank my friends, my girlfriend and my family for their moral support.

Erklärung

Hiermit erkläre ich, dass ich die vorliegende Dissertation selbstständig verfasst habe. Dabei habe ich keine anderen als die angegebenen Quellen und Hilfsmittel benutzt, Zitate wurden kenntlich gemacht.

Köln, den 30. Oktober 2012